POLITECNICO DI TORINO

Master's Degree in Biomedical Engineering

Master's Degree Thesis

Compact, low cost Particle Image Velocimetry system for the in vitro analysis of cardiovascular flows

Supervisors

Prof. UMBERTO MORBIDUCCI

Prof. DIEGO GALLO

Prof. CLAUDIO CHIASTRA

Ing. ELENA TORTA

Candidate

RICCARDO MUCCI

RAFFAELE FELICE

March 2021

Abstract

In the presented thesis, an experimental setup was designed and implemented for the in vitro study of haemodynamics in a model of a healthy coronary artery and of a stenotic coronary artery. The setup was fine-tuned with the aim of obtaining a compact and low cost test-bench that could be employed in various applications in the biomedical field. In particular, it can be used in the Artery in microgravity project in order to investigate the effect of microgravity on the fluid dynamic structures that are generated within the coronary models. The experimental equipment was chosen in such a way as to replace some characteristic elements of the setups for the traditional PIV (e.g. high frame rate cameras or pulsed light lasers) with low-cost ones. Specifically, the acquisitions were made using a mobile phone, while for the lighting, it was decided to use a continuous white LED light. The hydraulic circuit was suitably characterized in such a way as to reproduce a physiological flow-rate range (20-80 ml/min) relating to the coronary arteries. Subsequently, an in-depth study was carried out on flow visualization techniques and two different optical techniques were chosen. Both techniques made it possible to obtain the velocity fields, within the two models, of a blood-mimicking fluid inseminated with polyamide particles. The first optical technique chosen is Particle Image Velocimetry (PIV), which was implemented using the PIVlab algorithm in Matlab. The second technique taken into consideration is Optical Flow (OF), implemented in Matlab as well. The validation of the velocity fields obtained through the implementation of both approaches was carried out through a comparison with the results of the third PIV challenge, compared with the characteristic velocity values obtained from the imposed flow-rates and through comparisons with numerical simulations. The main sources of uncertainty of the method were also discussed and analyzed, in particular those that led to an underestimation of the fluid velocity values in areas where high displacements are reached, such as in the narrowing caused by the presence of stenosis. From the velocity fields obtained from the two algorithms, it was possible to visualize fluid

dynamic patterns of interest in the field of cardiovascular biomechanics. In fact, low speed recirculation areas downstream of the stenosis were detected, which are among the main causes involved in the genesis and development of cardiovascular diseases such as atherosclerosis. In order to investigate and deepen the analysis in the post-stenotic region, which is the region of interest, starting from the motion fields, further quantities and fluid dynamics parameters were also calculated and discussed. In conclusion, it can be stated that the proposed approach represents an easy to implement and low cost methodology that allows to obtain robust qualitative data to be able to investigate fluid dynamics in coronary arteries in vitro. The differences between the performances of both algorithms are highlighted in higher computational costs for the OF, while PIV has a lower maximum spatial resolution. A series of improvements have also been proposed which, if implemented in future applications of the presented method, would allow to reduce the sources of uncertainty, in order to further improve the quality of the results.

Table of Contents

List of Tables

List of Figures

Acronyms

AIM

Artery in microgravity

CCD

Charge coupled devices

CFD

Computational fluid dynamic

CFR

Coronary flow reserve

CMOS

Complementary metal oxide semiconductor

DA

Anterior descending artery

GUI

Graphical user interface

HDL

High density lipoproteins

ICE

International commercial experiment

ICF

Ice cubes facility

ISS

International space station

LCX

Left circumflex artery

LDL

Low density lipoproteins

LMCA

Left main coronary artery

MRI

Magnetic resonance imaging

OF

Optical flow

PC-MRI

Phase Contrast-Magnetic resonance imaging

PIV

Particle image velocimetry

PTV

Particle tracking velocimetry

PP

Polypropylene

RCA

Right coronary artery

SNR

Signal noise ratio

WSS

Wall Shear Stress

Chapter 1

Introduction

1.1 Preamble

This thesis work was developed by the collaboration of two students of the Politecnico di Torino, under the supervision of the research group of Computational Biofluidodynamics of the $Polito^{BIO}MedLab$. The initial aim of the work was to implement a method to visualize and study the motion of a blood mimicking fluid within phantoms of coronary arteries. This methodology would have served to extract information of fluid dynamics and biomedical interest from space experiments. With the development of the work, new objectives and goals have been set in order to improve the quality of the results.

1.1.1 Artery in Microgravity (AIM)

The setup developed in this work is an evolution of the one previously developed within the Artery in Microgravity (AIM) project. The project was born in conjunction with man's growing interest in space exploration, which therefore requires an accurate knowledge of health risks. Precisely with the aim of investigating the effects on the human body of the long exposure to the conditions of microgravity to which astronauts are subjected during long space missions. In fact, inside the experiment there are numerous sensors to detect the variation of some quantities. In particular, there are pressure sensors, to measure the pressure difference between

the two phantoms, a pH sensor useful for detecting dissolved ions in the working fluid following exposure to space radiation and, at the end, temperature sensors to control the operating temperatures [1].
The AIM experiment consists of a cube designed for ICE (International Commercial Experiment) Cubes Facility aboard the International Space Station (ISS). The ICE Cubes Services provide quick and easy access to the ISS in order to allow experiments to be carried out within it. The ICE Cubes Services makes use of the ICE Cubes Facility (ICF), a sliding platform permanently installed on-board the ISS that accommodates Experiment Cubes and that hosts the functional interfaces to the ISS infrastructure [1]. The dimensions of the cube inside which the experiment is contained are 10x10x20 *cm*. For the reasons just mentioned, one of the main objectives during the development of the setup was to reduce the space used to a minimum. Therefore each component has been carefully chosen to obtain the right compromise between reliability, efficiency and occupied space.

1.2 Aims of the thesis

Starting from the idea of characterizing the AIM setup, the aims of the thesis evolved into the development of a new approach to Particle Image velocimetry (PIV). In particular, the work was carried out to implement a compact and low cost setup that would allow the application of this technique in the cardiovascular field. Even if this technique is widely used in the fluid dynamics field, in this case it has been thought to mitigate the negative aspects, concerning the cost and the size. The next aim was to characterize the new setup and validate the results through the use of numerical simulations.
In addition to allowing an analysis of cardiovascular flows in space experiments, the aim of the presented methodology is to conduct in vitro experiments on patient-specific models. In fact, starting from medical images acquired through diagnostic tests (i.e. angiography, MRI, CT) it is possible to reconstruct the geometry of the blood vessels of a specific patient. Once the CAD model has been obtained, it is possible to create a realistic phantom with the aim of reproducing the patient's hemodynamics and studying it with in vitro experiments.

Chapter 2

Coronary arteries

This Chapter describes the cardiovascular system with particular attention to coronary arteries and their pathologies. In the first part of the Chapter there is a brief general introduction on the cardiovascular system in general, its constituent elements and its main functions within the human body. In the second part of the Chapter a brief discussion on the motion of fluids inside cylindrical pipe, as in the case of blood, with an analysis and description of the types of motion present within the cardiovascular system is presented. These first two parts serve as a framework for the later parts of the Chapter. In particular, the third part illustrates the coronary arteries with the description of their location within the cardiovascular system. In the following, some characteristics of the flow and motion of blood inside the coronary arteries are described, with particular reference to the velocities and flow-rates inside them. Then a description of the pathologies affecting the coronary arteries with the causes and the damage that can arise from them, followed by the effects of coronary pathologies on the motion conditions and flow parameters are described. In the last part of the chapter a brief presentation of the most used techniques for cardiac flow visualization is reported.

2.1 General introduction

The cardiovascular system is composed of three main elements: blood, blood vessels and the heart. It is a closed system of vessels in which blood circulates under the pressure exerted by the heart. The most important functions of the cardiovascular system are [2]:

- Supply of oxygen and nutrients to the body.
- Thermal regulation (heat transfer in blood).
- Transport of immune cells and antibodies with defensive function.
- Hormonal control.
- Haemostasis (transport of blood platelets and coagulation factors).

It is composed of two main components: systemic circulation and pulmonary circulation. The blood in the systemic circulation, that came from the lungs, is full of oxygen and nutrients and is pumped from the left ventricle into the aorta, in order to be distributed throughout the body. When it reaches the tissues, the blood releases oxygen and nutrients, and contemporary it collects carbon dioxide and waste product, produced during cellular metabolism. At the end of the cycle it goes to the right atrium through the vena cava [2].
Systemic circulation is schematically represented at the bottom of Figure 2.1, it is possible to see the aortic arch from which the blood is distributed along the other districts and the vena cava that canalize the blood flow into the right atrium. The pulmonary circulation is a closed circuit between the heart and lugs. It starts from the right ventricle, where the blood rich in carbon dioxide and waste products is pumped in the pulmonary artery. The latter divides in two branches each one goes to a lung. At this point the branches end forming capillaries that collect oxygen at the level of the alveoli. The oxygenated blood flows into increasingly larger vessels, until to the pulmonary veins. Then it pours into the left atrium of the heart from which it will pass into the left ventricle through the mitral valve. In Figure 2.1 the pulmonary circulation and the path through the lungs are schematically

represented.

The 84% of the blood circulates through the systemic circulation, while the remaining 16% through the pulmonary circulation, and it is interesting to note how the whole volume of blood that circulates in one minute in the systemic circulation is equal to that which circulates, in the same time interval, in the pulmonary circulation. This is precisely to highlight the high metabolic need of the heart compared to the other compartments of the body.

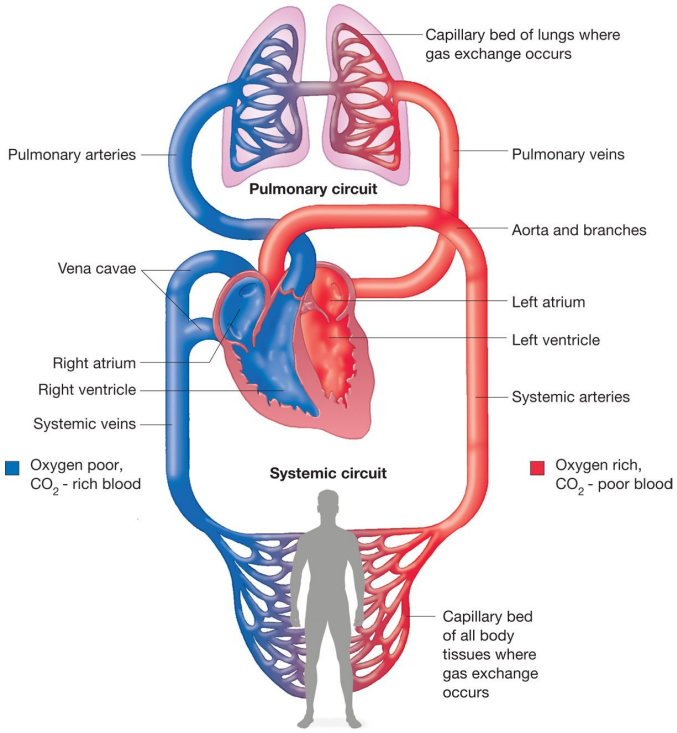

Figure 2.1: Schematic representation of Cardiovascular system that is composed by the systemic circulation (at the bottom of the figure) and pulmonary circulation (at the top of the figure) [3].

As explained in detail in [4], the complex circulatory mechanism has three basic principles that highlight the functioning of the system:

1. The blood flow rate for each tissue in the body is controlled according to the metabolic needs of the tissue.

2. The cardiac output is more controlled by the sum of all the local tissue flows.

3. In general the arterial pressure is controlled independently of either local blood flow control or cardiac output control.

Considering the third point, for example, if the pressure drops drastically, nerve barriers are activated causing a series of reactions to restore the pressure to normal value. These mechanisms can, for example, increase the heart's pulsatile force, can cause the large veins to constrict to supply more blood to the heart, or could cause arterioles to constrict so blood accumulates in larger arteries. All these mechanisms are intended to restore pressure [2].
As shown in Figure 2.2 the blood flow in a vessel is regulated by the difference in pressure between two ends of the vessel itself, that is the pressure gradient, and by the vascular resistance. Vascular resistance is caused by the friction between the endothelium of the vessel walls and the flowing blood. The relation between resistance and pressure is:

$$F = \frac{\Delta P}{R} \tag{2.1}$$

where F is the flow, ΔP is the pressure gradient and R is the vascular resistance [4].

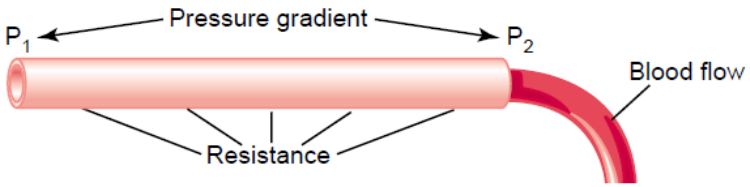

Figure 2.2: Relationship between flow, vessel resistance and pressure gradient [4].

2.2 Laminar and turbulent flow in cardiovascular system

The description of the motion of the fluids, and therefore also of the blood inside the vessels, depends on some descriptive parameters of the motion. These allow to predict the possible development of some fluid dynamic structures.

One of this that allow the description of turbulence is the *Reynolds Number*, given by the formula :

$$R_e = \frac{\rho v d}{\mu} \tag{2.2}$$

Observing Equation 2.2, it is possible to assess that Reynolds number is directly proportional to the diameter of the pipe d, to the velocity of the fluid v and to the density of the fluid ρ. While it is inversely proportional to the viscosity of the fluid μ. This fraction represents the ratio of inertial forces to viscous forces [5]. As depicted in Figure 2.3, three main ranges of Reynolds number values have been identified and they represent different flow patterns.

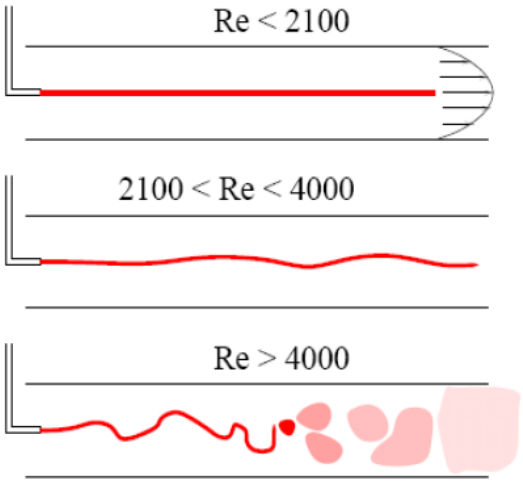

Figure 2.3: Reynolds number values and associated motion types inside a cylindrical pipe [5]. The top figure represents the laminar motion, the middle one represents the transitional regime and the bottom one the turbulent motion.

The first case represents the *laminar flow*, which can be observed for Reynolds Number values lower than 2100. In this condition the flow velocity in the center of the pipe is greaterthan than the one in the areas located near the walls. This creates a parabolic velocity profile within the pipes under steady flow conditions [5]. The parabolic velocity profile is created because the motion of the fluid molecules touching the wall is greatly reduced due to the friction and adhesion between the fluid and the pipe walls. The velocity increases going from the walls towards the

center of the pipe because each layer of fluid moves with a slightly greater speed than the previous one [6].
In the central image of the Figure 2.3 the *transitional regime* is presented. This flow pattern arises for values of the Reynolds number between 2100 and 4000 and the value of the Reynolds number at which the transition from the laminar regime to the transition regime takes place is called *critical Reynolds*. In this case, the fluid trace maintains its spatial coherence by remaining confined within a thin lamina [5].
The last image in Figure 2.3 represents the *turbulent motion*, that is established inside the pipe for Reynolds values higher than 4000. In this case, after an initial stretch with increasingly large oscillations, the diffusion of the fluid becomes increasingly important along the entire cross section of the pipe. In this case the motion has three-dimensional and non-stationary characteristics, with non-deterministic speed fluctuations [5].

2.2.1 Type of flow in arteries

When blood flows steadily through long, smooth-walled blood vessels, its flow is in a laminar regime. The flow can become turbulent when it passes through an obstruction, when it passes through areas with sharp curvatures or with rough surfaces. The motion inside the vessel in turbulent conditions has a disordered pattern that causes the formation of vortices within the bloodstream, the blood, in turbulent conditions, flows with a much greater resistance due to the friction between the vortices and the vessel walls [2]. The formation of turbulent motions is directly proportional to the velocity of the blood, to the diameter of the vessel and to the density of the blood, while it is inversely proportional to the viscosity of the blood, as expressed by 2.2. Normally, within the circulatory system, the Reynolds number is between 200 and 400. The arise of turbulent motions occurs in the bifurcations of the vessels or in the great arteries [2]. This type of motion in biological systems for humans and animals of similar size is substantially limited to some portions of the aorta, particularly during the diastolic phase of the cardiac cycle [5].

Some conditions can favor the onset of turbulence inside the vessels:

1. High blood flow rates compared to normal conditions.

2. Pulsating nature of blood flow.

3. Sudden changes in the diameter of the vessel.

4. Vessels of larger diameter (i.e. aorta or aneurysm).

2.3 Anatomy of Coronary artery

The coronary arteries provide an adequate amount of blood to guarantee the correct supply of oxygen and nutrients to the cardiac muscle for its metabolic demands. Looking at Figure 2.4, it is possible to see that the coronary arteries originate from the initial portion of the ascending aorta and divide into the right coronary artery (RCA) and left main coronary artery (LMCA). The two main coronaries lie on the outer surface of the heart and divide into smaller arteries that penetrate the heart muscle. The RCA descends vertically between the right atrium and the right ventricle through the coronary sulcus. It supplies the right atrium, the right ventricle, the electrical conduction system of the heart and a portion of the left ventricle [7]. The LMCA, larger than the previous one, passes through the pulmonary artery before entering the coronary sulcus. The LMCA, after 2-4 cm, divides into two branches, one is the anterior descending artery (LDA) that flows on the anterior wall of the heart. The other one is the circumflex artery (LCX) which runs along the lateral wall of the left ventricle. LMCA supplies blood to most of the left atrium, left ventricle, and intraventricular septum[7].

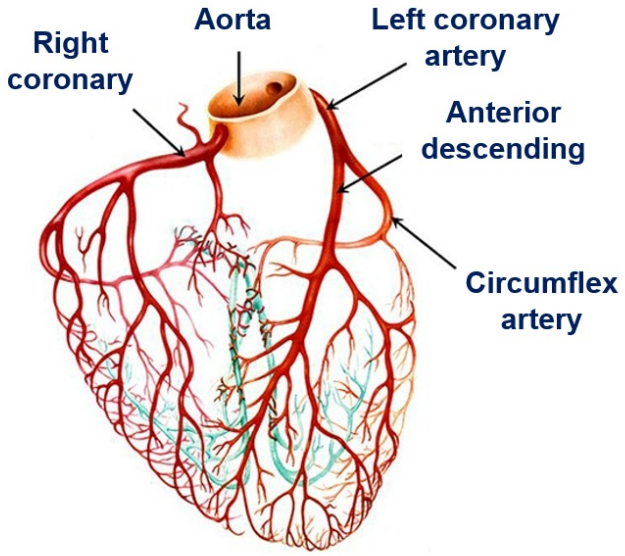

Figure 2.4: Arterial network of the heart. The main coronary arteries are highlighted, and it is possible to observe the two main coronaries originating from the aorta [8].

2.3.1 Coronary flow

The blood circulation in the heart is very important, in fact, the heart has the highest oxygen consumption per tissue mass of all human organs. The coronary blood flow ranges around 250 ml/min at rest and this value represent the 5% of the cardiac output[9]. It is almost entirely through these arteries that the heart receives its nutritive blood supply and only a small percentage of nutritive blood came directly from the heart chamber. During an intense exercise the coronary blood flow increases threefold to fourfold to supply the extra nutrients needed by the heart [9].

Figure 2.5 shows the variation in blood flow through the nutrient capillaries of the left ventricular coronary system in the human heart during systole and diastole. As described in the [4] blood flow in the left ventricle muscle decrease during systole. This is due to the strong compression exerted by the cardiac muscle during its contraction on the intramuscular vessels during systolic contraction. During

diastole, the cardiac muscle relaxes and no longer obstructs blood flow through the capillaries. Some measurements, as reported in [10], obtained through the use of doppler catheters, have allowed to obtain average velocities inside the coronary arteries equal to 30 cm/s. The velocity values are different during the cardiac cycle, in fact, during the diastolic peak velocities are between 40 cm/s and 80 cm/s while during the systolic peak the values are between 10 cm/s and 20 cm/s. Since there are three main coronary arteries, as briefly described in 2.3, it is possible to hypothesize an average value of flow, in each coronary artery, equal to 60 ml/min [11]. Assuming an average diameter equal to 3 mm, an average velocity is obtained, during the cardiac cycle for each coronary artery, equal to 35 cm/s, which is about the value above mentioned. Moreover, the total flow divided by the three main coronaries, a small part of the flow distributed along the smallest arterioles must be considered.

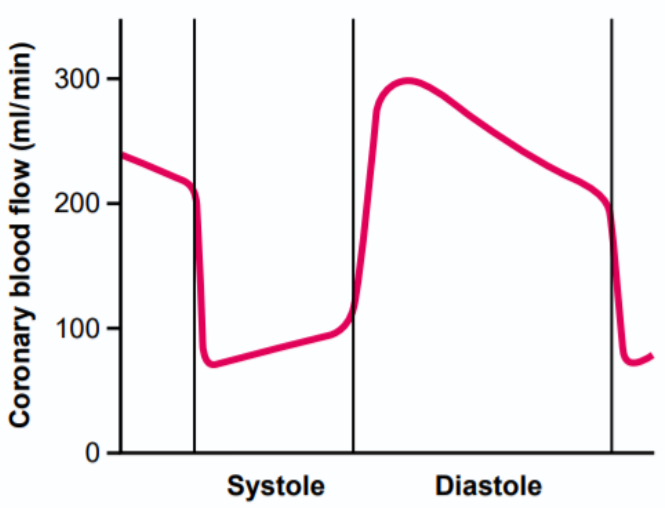

Figure 2.5: Blood flow rate during cardiac systole and diastole through the coronary capillaries of the human left ventricle [4].

Blood flow in the coronaries is regulated proportionally to the need of the cardiac musculature for oxygen. The supply of oxygen and nutrients is provided by a highly sophisticated dynamical system that has a wide range of regulatory mechanisms and a large network of conducting vessels. Because of their function, the development

of coronary artery diseases decrease the myocardial flow perfusion and can cause severe damages to the myocardium, such as myocardial ischemia and infarction [4]. As can be seen from Figure 2.6, coronary arteries have high curvatures, this can cause disturbed flow patterns, resulting in stenosis and atherosclerosis as better described in the next section.

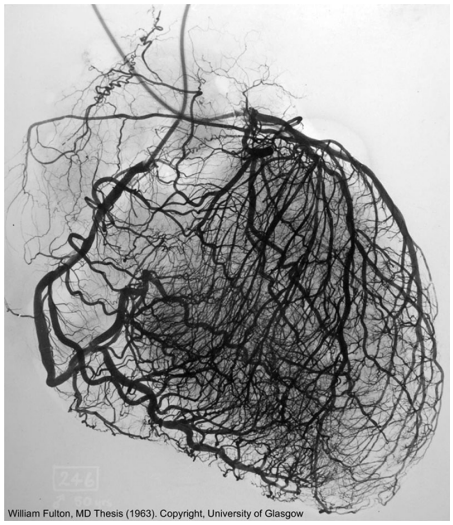

Figure 2.6: Extensive network of conducting vessels and the highly sophisticated dynamical system that provide the blood supply to heart tissue [12].

2.4 Atherosclerosis

As depicted in section 2.3.1, the blood flow could be extremely disturbed and it can cause a damage to the vascular endothelium, that bring to atherosclerotic lesions, plaque formation and stenosis.

Atherosclerosis can affect all large and medium-sized arteries and it is the leading cause of mortality in the United States and in most developed countries. Lots of studies have shown that early vascular disease develops in regions of arterial branching and curvature where blood flow patterns are multi-directional and highly disturbed [13]. Atherosclerosis consists of the formation of a lesion made up of fatty material called atheromatic plaque and develops within the surface of the arterial walls. Plaque development begins with a dysfunction of the endothelium,

which causes the expression of adhesion molecules such as VCAM-1 (Vascular Cell Adesion Molecule) and ICAM-1 (Intracellular Adesion Molecule). In this way the ability to release substances that prevent the adhesion of macromolecules, platelets and monocytes decreases [14]. After the lesion has formed, lipids, cholesterol in the low-density lipoprotein forms, and monocytes accumulate in the lesion area. Monocytes migrate into the intimate tunica of the vessel and differentiate into macrophages. As a result of these processes, a migration of smooth muscle cells from the tunica media of the vessel occurs, thus leading to the formation of the atheromatic plaque. The latter consists of a core and a fibrotic outer part. As the plaque increases in size, it can grow within the lumen of the vessel reducing blood flow, as shown in Figure 2.7. Furthermore, the formation of plaques causes a stiffening of the vessel, due to the deposit of connective tissue and calcium salts that precipitate together with the lipid plaque. One of the most dangerous effects of plaque formation is its rupture and this can lead to thrombus formation with myocardial ischemia and tissue necrosis [14].
Atherosclerosis can also cause a lots of less serious pathologies including gangrene in the lower limbs, ischemic encephalopathy, aneurysms and stenosis of the aorta and renal arteries [14][4].

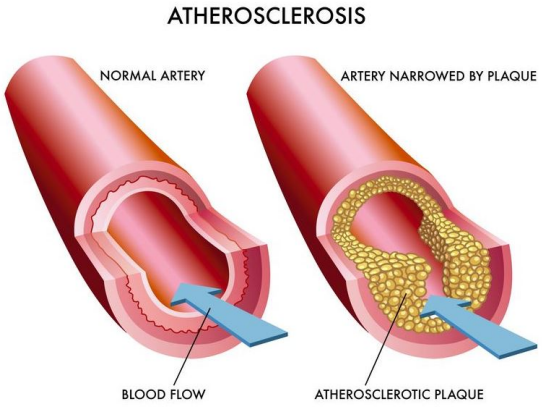

Figure 2.7: Comparison between a healthy vessel and a vessel in which the atheromatic plaque has formed. In the second case, following the formation of the plaque there is a modification of the hemodynamics [15].

2.4.1 Causes of atherosclerosis

One of the main causes that contributes to the formation of atherosclerotic plaque inside the arteries is a high concentration of cholesterol (LDL). In particular, the concentration of cholesterol (LDL) increases as a result of an improper diet rich in fat, obesity and physical inactivity. The high percentage of cholesterol in the blood, also called hypercholesterolemia, can also be due to genetic reasons. This causes a higher concentration of cholesterol in the blood starting from birth [4]. Instead, a high concentration of high density lipoprotein (HDL) has been shown to have a protective behavior against the absorption of lipids by the vessel walls. These molecules can absorb the cholesterol which is deposited on the vessel walls. Other risk factors are age, the presence of diseases such as diabetes, hypertension, hyperlipidemia and cigarette smoking. Table 2.1 highlights the main causes of risk that lead to the formation of atherosclerotic plaque, including those mentioned above.

Irreversible factors	**Reversible factors**
Age	Stress
Gender	Cigarette smoke
Previous pathologies	Use of oral contraceptives
Genetic hypercholesterolemia	Unbalanced diet
Genetic hypertension	Sedentary lifestyle
Genetic obesity	Obesity due to diet

Table 2.1: Summary of risk factors that contribute to the development of atherosclerosis [13].

2.5 Stenotic coronary hemodynamics

As mentioned in Section 2.4 coronary artery diseases begin with the deposit of lipidic materials in the vessel causing it to thicken.

During the initial stages of the disease there are no major changes in local hemodynamics: in fact, the flow continues to be laminar as in healthy coronaries. As the disease progresses, the plaque grows inside the lumen of the vessel, and this causes an alteration in the hemodynamics inside of it. Following plaque growth, the flow will no longer be fully laminar as in the case of healthy coronaries and this causes a significant change in the flow characteristics [13].
Stenosis is usually classified according to the percentage of restriction that causes inside the vessel. In particular, mild is defined as a stenosis from 20% to 49% of restriction, moderate from 50% to 69% and severe between 70% and 99% up to the complete occlusion of the artery [16].
Some studies, like [17], have shown how the geometry with which the plaque develops influences the velocity fields inside the vessel. As plaque develops, some conditions that alter the flow are created and contribute to plaque growth.
As will be shown in Section 5.1.5, the restriction causes a pressure difference between the pre-stenosis zone and the post-stenosis zone. In fact the pressure drop downstream of the stenosis occurs in accordance with Bernulli's law, following the reduction of the area of the vessel section. In the ideal case, a complete recovery of pressure downstream of the restriction is obtained [6].
In the real case turbulence, and associated energy losses along with the narrowed radius are two of the primary causes that produce an incomplete recovery pressure distal to a severe stenosis. In atherosclerotic arteries and/or at branch points, the critical Reynold's number is much lower and there can be turbulence even at normal physiologic flow velocities [18]. In severe stenoses, turbulence can be initiated at Reynold's numbers an order of magnitude less than in the theoretical [18]. Furthermore, due to the restriction, referring to the equation 2.1 the resistance or impedance of the vessel to the passage of blood flow increases. A change in the distribution of pressures and shear stress is observed through the restriction and separated region of flow are formed. As has been noted in [10], the velocity in the distal zone of the stenotic coronaries is considerably decreased. In addition, the ratio of proximal to distal velocity increases significantly, and this highlights how, in pathological vessels, the obstructions inside the lumen are the cause of the alterations in the velocity patterns.

With the development of an atherosclerotic plaque and therefore of a stenosis, variations in some flow parameters are observed.
As described in [19] coronary flow in resting conditions does not vary until there are occlusions of the vessel equal to 85% of the diameter. The coronary flow reserve (CFR), which is the maximum flow normalized with respect to the flow under rest conditions begin to decrease with stenosis of $30\% - 45\%$ in diameter [20]. Moreover, with high restrictions of $88\% - 93\%$, the ability to increase the flow beyond the basal level following a vasodilatory stimulus disappears.
The greatest differences in blood flow velocities are found between the diastolic peak velocity, which is lower in stenotic arteries. The greatest speed differences are observed in the distal area of the stenosis. Figure 2.8 shows two graphs that describe the variation in pressure and flow following the stenosis. Figure 2.8 (a) shows how the CFR along a stenotic vessel undergo a greater decrease as the degree of stenosis increases.

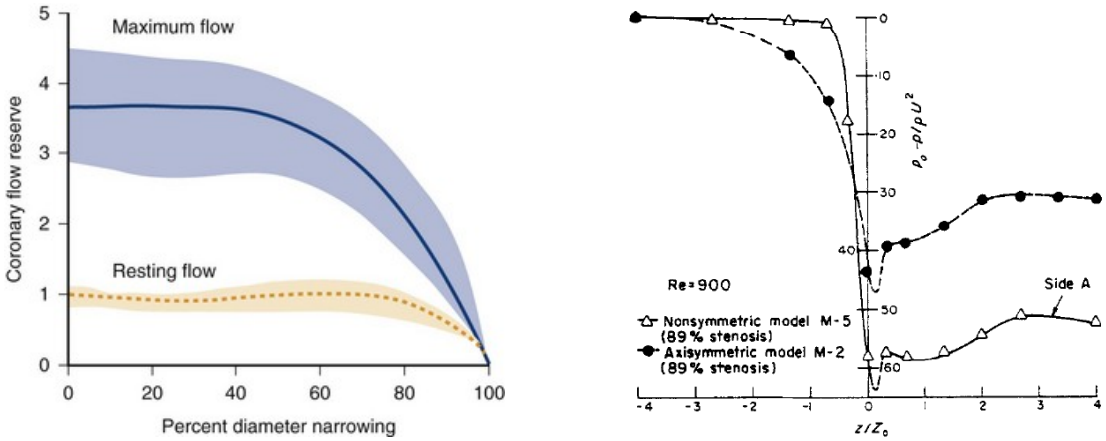

a b

Figure 2.8: (a) Variation of the flow as a function of the degree of stenosis (b) Representation of the variation in pressure from the pre-stenotic to the post-stenotic zone [21].

In particular, there are greater variations following the stenosis in the conditions of maximum flow, represented by the blue curve. In resting conditions, significant changes in the CFR are evident only with high degrees of stenosis. In Figure 2.8 (b)

the horizontal coordinate z, represented on the abscissa axis, is normalized to Z_0, where Z_0 represents the stenosis coordinate. It is possible to observe how, passing from the pre-stenotic area to the post-stenotic one, there is a sudden variation of the pressure conditions. In particular, the downstream area of the stenosis has a lower pressure than the upstream area. Furthermore, the two curves that are represented in the graph are related to an axisymmetric stenosis and an asymmetric stenosis. In the case of axisymmetric stenosis (represented by colored circles) the pressure gradient is smaller.

2.5.1 Fluid dynamics in pathological conditions

The development of atherosclerosis in human arteries is a complicated mechanism and is linked to the interactions of several factors, namely systemic, biological and haemodynamic factors [13]. In this paragraph it will be mentioned some of the factors related to haemodynamics that can lead to the development of atherosclerotic pathology. In particular, it has been demonstrated that there are fluid dynamics structures identified as indicators of "disturbed flow", which contribute to the development of the pathology. Among these fluid dynamic structures it is possible to mention: areas of separation or re-attachment of the flow, low and oscillating wall shear stresses (WSS) and stagnation points of the flow.
As demonstrated by the experiments conducted by [22, Javadzadegan et al., 2013], downstream of the coronary stenosis, regions with fluid decelerations and recirculating areas are generated in which the inversion of motion is present. In particular, the low-speed recirculating zones are associated with atherogenetic areas and can induce endothelial dysfunction and remodeling of the vessel in the coronary arteries. In Figure 2.9 the experimental and numerical results conducted on a stenotic coronary artery model are shown [23]. Observing the velocity field it is possible to notice the separation of the main jet, with the formation of a recirculation zone at low speed in the lower region of the vessel, downstream of the restriction.

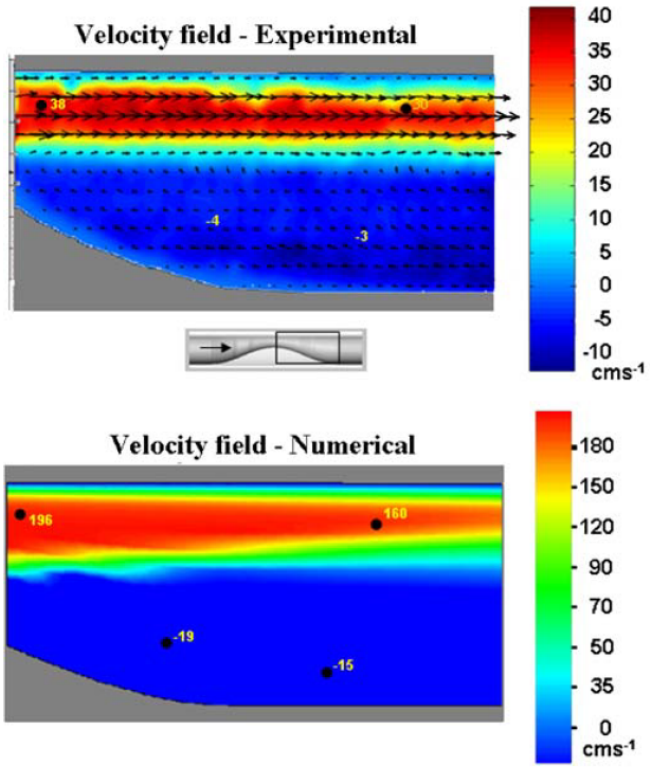

Figure 2.9: Experimental and Numerical Velocity Field from a coronary artery model with an eccentric, axisymetric stenosis. Formation of a recirculating zone with low velocities downstream of the restriction [23].

The disturbed flow events have a direct interaction with anomalous biological phenomena such as dysfunction of the vascular endothelial cells, damage to the endothelium, increased permeability of the wall, aggregation and deposition of platelets and fibrin. Furthermore, the formation of atherosclerotic plaques was also observed in regions where the above mentioned fluid dynamic structures were not present, but a velocity distribution far from the physiological one was present [24]. The most relevant factors that contribute to the gradual thickening of the vessel walls are low blood velocity in the pathological area of the vessel and the consequent presence of low WSS on the wall. Therefore low velocity and high velocity of flow play a pathogenic and preventive role respectively. In fact, as reported in the study [24], there is less development of pathologies in the distal area of the coronary vessels since, following the curvatures, the speed is 1.5 times greater than that in

the proximal area.
In low-flow regions, the radial component of velocity in the fluid layers adjacent to the endothelium may have the same order of magnitude, or greater, than the longitudinal component, and this can cause the adhesion of particles to the endothelium. Low speed and low WSS can promote prolonged interaction and adhesion, thus the accumulation of macromolecules in the intimal layer of the vessel continues over time. The particles accumulate in the region with the lowest pressure, which causes thickening of the endothelium in these regions, forming further zones of recirculation and flow separation [24].
As observable in Figure 2.10 if the cells of the endothelium are exposed to a laminar flow with high WSS values they tend to orient themselves in the main direction of motion and stretch. In areas where there is disturbed flow, the cells are subject to low and oscillating WSS and this causes their disorganization which leads them to assume irregular shapes [25]. The change in the morphology of endothelial cells can cause an increase in permeability to water, solutes and macromolecules and therefore influence the formation and development of atherosclerotic pathology [13] [24].

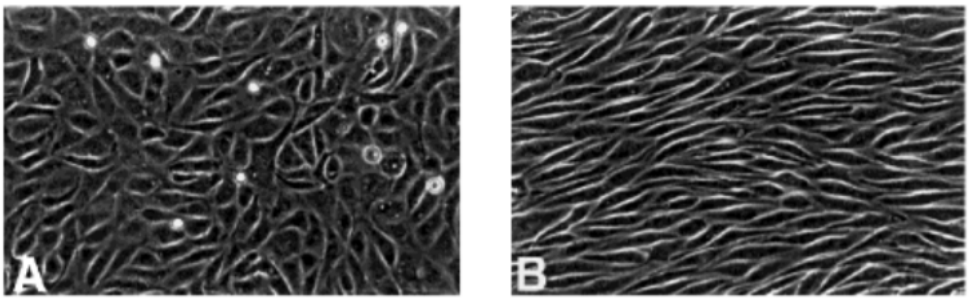

Figure 2.10: Phase contrast micrograph images of bovine aorta endothelial cells. Image A: endothelial cells are disorganized in the presence of low WSS. Image B: endothelial cells in the presence of physiological WSS tend to organize themselves in the main direction of motion [25].

Moreover another parameter of rheological interest, as described in [26], is the shear rate of blood flow, since this parameter affects the apparent viscosity of the blood and therefore its behavior. In particular, the shear rate affects the adhesion

between red blood cells which in turn influence and determine the viscosity of the blood. From the studies conducted in [22] and [23] it has been shown that low shear rate values associated with the formation of atherogenetic areas are present in the recirculating zones. While in the flow separation zone high shear rates are obtained which can lead to the activation of platelets and leukocytes causing inflammatory and thrombotic states. Figure 2.11 shows the shear rate map for the coronary artery model studied in [23]. From the figure it is possible to observe maximum values of shear rate in the upper region of the vessel near the wall and in the separation region, between the jet and the low speed recirculation zone.

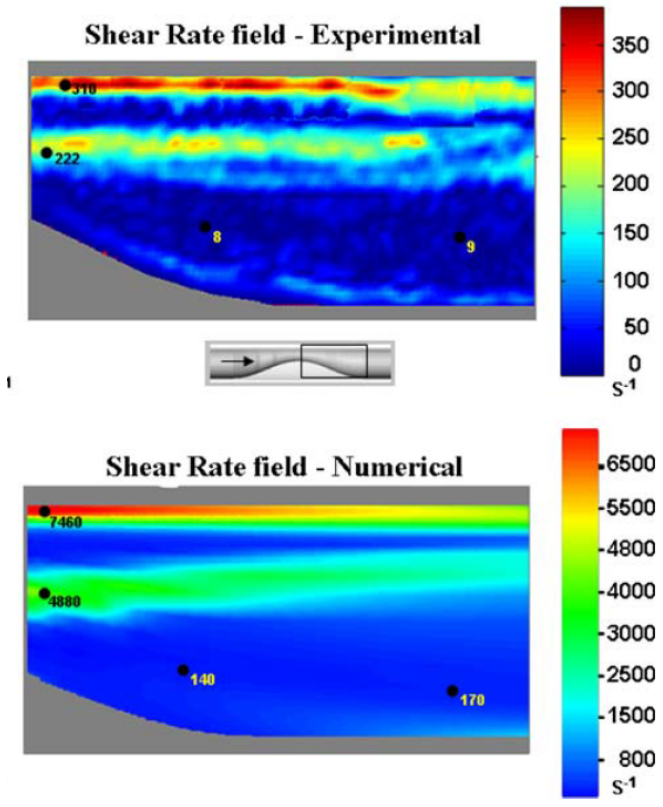

Figure 2.11: Shear rate maps of post-stenotic region. Top image: Experimental results. Bottom image: Numerical simulations. [23]

2.6 Cardiac Flow Visualization Techniques

Cardiovascular flow visualization techniques can be divided into three main categories [27]:

- In vivo techniques: these are techniques that involve direct interaction with the patient and for this reason they are the ones that give the optimal representation of reality.
- In vitro techniques: they are carried out outside the human body, and for this reason they are not always usable.
- In silico techniques: refer to computational studies using Computational fluid dynamic simulations (CFD).

2.6.1 In vivo techniques

The in vivo techniques that allow to observe the functioning of the heart are numerous. They are distinguished according to the type of physical approach on which they are based [27].

Echocardiography

Among the most used techniques in the cardiovascular field are those that exploit ultrasound as in the case of techniques based on echocardiography. On the basis of the methodology with which the technique is used, distinctions can be made. For example, transthoracic echocardiography is configured as a non-invasive technique which, through the use of a transducer, which is placed on the patient's chest, allows the images to be reconstructed. Transesophageal echocardiography, on the other hand, allows the reconstruction of cardiological images by inserting a probe inside the patient's esophagus. In this way it is able to return more defined images to the detriment of the patient's comfort. Finally, another technique that involves the use of ultrasound is intracardiac echocardiography. This allows to obtain very defined images through the insertion of a venous catheter [27].

Doppler echocardiography

Doppler echocardiography is one of the most used techniques. It is based on the Doppler effect and allows to measure the speed along the direction of the sensor. The velocity can be determined by the following formula:

$$v = \frac{(f_e - f_r)c}{2f_e cos(\theta)} \tag{2.3}$$

where v is the velocity to be estimated, f_e the emission frequency, f_r the reception frequency, θ the angle between the ultrasound beam and the object under study and c is the velocity of sound transmission in the tissues.
There are three types of Doppler electrocardiography, for example Pulsed Doppler, which emits an ultrasound pulse in a pulsed way that is received by the sensor after a time interval depending on the depth of the tissue. Unlike this technique, the continuous doppler emits and receives simultaneously and this allows to measure higher speeds than in the previous case. A variation of the pulsed doppler is the color doppler which allows to obtain two-dimensional colorimetric maps. Its operation is similar to that of the pulsed doppler [27].

Echo-PIV

The Echocardiographic Particle Image Velocimetry is based on particle image field acquired by ultrasound. For this technique, hydrophilic gaseous particles are used as the contrast medium. To avoid emboli these particles must be the same size as the red blood cells. Some problems with this technique may be due precisely to the use of particles as a tracer. Moreover this technique allows to measure speeds up to 0.42 m/s because it does not have sufficient accuracy for higher speeds. For further information on this technique, the reader is referred to [28].

MRI (Magnetic Resonance Imaging)

This technique allows for three-dimensional reconstructions with the use of magnetic fields. Magnetic fields force the hydrogen atoms inside the body to align with the magnetic field itself. The formation of the image is based on the application of

a radiofrequency which causes a bending of the protons out of equilibrium. The reestablishment of equilibrium causes the release of energy which is used for imaging. Often these techniques are accompanied by the use of contrast agents to improve their effectiveness. A specific type of MRI is PC-MRI (Phase contrast-Magnetic Resonance Imaging) which allows to measure the speed of the blood in certain directions of the gradient of the magnetic field. For a complete discussion see [29], [27].

2.7 In vitro and in silico techniques

In vitro visualization techniques have always been a support to in vivo ones and have gradually developed over the years. The heart of the in vitro techniques consists of the visualization techniques that will be described in detail in Chapter 3. They are configured as optical techniques since they require visual access to the region under investigation.
In silico techniques are those that involve the use of CFD simulations. They are widely used in research in the study of cardiovascular flows and will be explored in Chapter 8.

Chapter 3

Visualization techniques

Principles and main features of the flow visualization techniques used in this thesis are presented in this Chapter. The first part of the Chapter is devoted to the description of the tracers, from the historical background to their characterization. The tracers used in this project are of two types: continuous (e.g. ink) and discrete (particles). The difference between the latter are here described in terms of dynamic and optical property. In the second part, the imaging of the particles tracers through a camera is described. The final part of the chapter introduce the working principles of the two techniques used in the data acquisition: Particle Image Velocimetry (PIV) and Optical Flow (OF).

3.1 Historical Background

In the course of history, the first attempts to visualize the fluid dynamic structures that form inside a moving fluid date back to Leonardo da Vinci's detailed drawings concerning the formation of vortices in a water flow. Later, in 1883, Osborne Reynolds conducted experiments to show the transition between laminar and turbulent flow in a pipe (Figure 3.1) [30]. Thanks to the invention and improvement of photographic recording techniques it was possible to capture images of the flows and make the results of the flow visualizations more accessible by the scientific community. It is possible to recall Ahlborn's experiments that used aluminum or

lycopidium particles in a water tunnel, illuminating through a narrow slit window [31]. Prandtl used as a starting point the techniques of Ahlborn to study separate unstable flows behind wings and other objects, in the Figure 3.2 it is possible to observe his water channel in which the visualizations are made with a box camera above the channel and the fluid it is inseminated with micaceous iron particles.

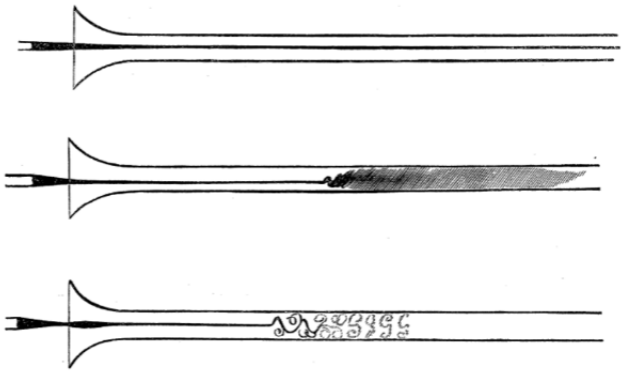

Figure 3.1: Experiments by means of colour bands in glass tube: schematic drawings of different flow structures of water flow in a pipe obtained by Reynolds [30].

These first experiments carried out on the visualization of flows laid the foundations for the experimental techniques currently used.
The history of flow visualization began with qualitative approaches and it is thanks to technological progress, such as digitalization of cameras and development of computers, that a quantitative approach has also been obtained. In fact, today it is possible to extract both qualitative and quantitative information from the motion of a fluid.
As shown in Figure 3.3 a it was possible to replicate the Prandtl experiment using aluminum particles for the insemination of the water flow and lighting the particles twice from a flash lamp placed above the water tunnel and capturing the particle position with a camera in two instants of time. Simplifying the concept, it is possible to state that the local flow velocity can be determined by knowing the local displacement of the tracer particles and the time interval between the two illuminations (see figure 3.3 b). This illustrates the basic principles underlying the

quantitative visualization technique Particle Image Velocimetry (PIV) discussed in the section 3.5 [32].

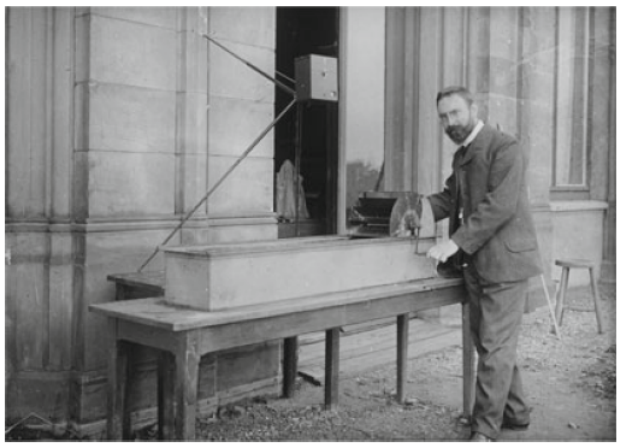

Figure 3.2: Ludwig Prandtl in front of his water channel for flow visualization in 1904 [32].

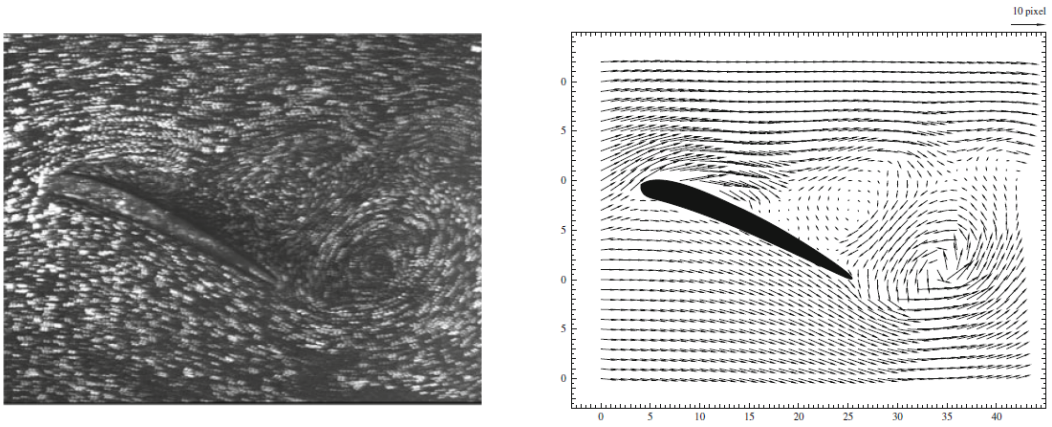

a b

Figure 3.3: Image a: Separated flow behind wing profile, visualized with modern equipment in a replica of Ludwig Prandtl's water channel. The image shows the superposition of two sequentially acquired images in order to resemble a photographic recording of 1904. Image b: Vector map of instantaneous velocity field corresponding to Image a. [32]

For a complete chronology of the history of visualization techniques, the reader is referred to [33] [34] [35].
After this brief historical analysis on visualization techniques it can be stated that the main element for observing and studying the motion of a fluid is the tracer, such as particles. Furthermore, the imaging system is of great importance, which allows the signal deriving from the particles to be transformed into data that can be stored and processed. These two main aspects of visualization techniques will be described in the following sections.

3.2 General principles

Since most liquid or gaseous fluids are transparent media, capturing their motion is difficult for the human eye. As reported on [33] "Flow visualization is a tool in experimental fluid mechanics that renders certain properties of a flow field directly accessible to visual perception". To make the flow visible it is necessary to illuminate the field of motion. What is perceived by the human eye is the result of the interaction between light and fluid. [33]
It is possible to exploit the interaction between light and the flow of a fluid mainly in two ways: by recording the light transmitted through the fluid and comparing it with the incident one or recording the light scattered by the fluid flow. In the first case it is possible to cite techniques based on the variations of light due to changes in the refractive index of the fluid (optical interferometry, schlieren and shadography) [33]. In the latter case the light gives information on the state of the flow from the position in which it is scattered, therefore these techniques give local information on the flow. It is necessary to remember that due to absorption phenomena the scattered light is much lower than that incident. In Figure 3.4 it is shown a typical interaction between light and fluid domain.
In order to expand the light intensity scattered by the fluid, so that it can be recorded, it is necessary to seed the fluid with tracer particles much larger than the fluid molecules. Since what is recorded is the movement of the particles it is necessary to ensure that their motion approximates in the best way that of the fluid [33]. In the following section there will be a brief discussion on seeding techniques

and properties of continuous and discrete tracers used in techniques based on the recording of light scattered by the fluid.

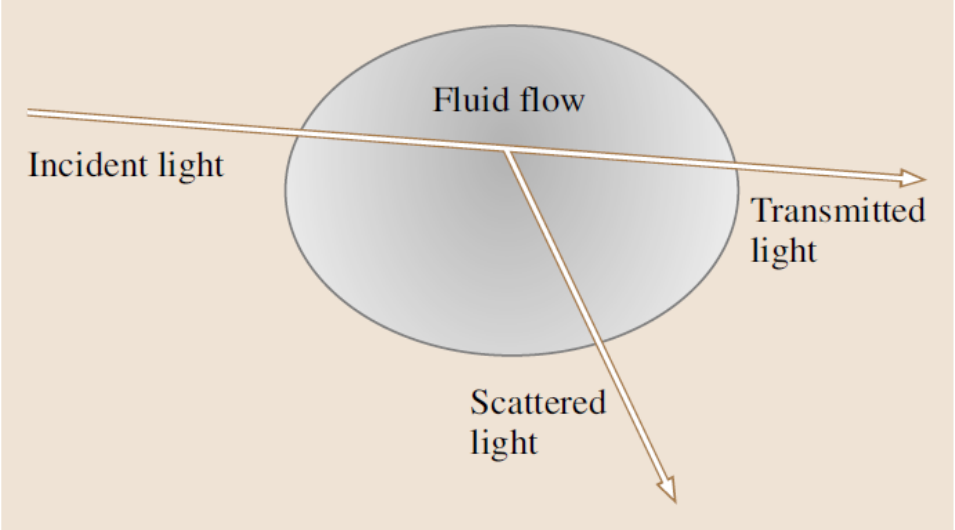

Figure 3.4: Representation of interaction between a wave light and a fluid flow [33].

3.3 Tracers

As previously described to ensure that the observer receives enough light scattered by the flow it is necessary to add tracers to the fluid. In order to minimize the properties difference between the tracers and the working fluid as much as possible neutrally buoyant tracer materials are used. The condition of neutrally buoyancy occurs when the average density of an object is equal to the density of the fluid in which the object is immersed. In this way the object does not go deep into the fluid because the force of gravity is balanced by the buoyancy force [36]. The most used tracers for liquids are dyes, while smoke is used for gases.

3.3.1 Continuous tracers

Among the various visualization techniques, those that use continuous tracers are the easiest to implement, especially for the easy availability and the low cost of the

materials used.

- *Food dye*: Generally, ink and food dye are the tracers most used. Often food colors have a specific gravity grater than one and this high concentration will not allow them to accurately follow the flow field. For this reason in order to make the dye neutrally buoyant, a small amount of alcohol (methanol or ethanol) is added before diluting the tracer with the working fluid. It is also of fundamental importance to regulate the concentration of the dye because it will tend to diffuse into the fluid. If the diffusion of the dye in the fluid is too high this will lead to obtaining images with poor contrast between the two phases and consequently a poor visualization of the fluid motion [37].

- *Laundry brightener*: This readily avaliable product has been widely used in various studies on flow visualization (see Lim & Nickels, 1992; Kelso et al., 1996; Lim, 1997; Adhikari and Lim, 2009) [37]. The advantage of this material is that it diffuses in water more slowly than food dye, allowing to improve the visualization and to extend the times of experiments.

- *Milk*: It has excellent reflective properties that help to improve contrast in images and its high fat content allows it to delay diffusion in the fluid [37].

- *Fluorescent dyes*: They are the tracers that allow to guarantee a high optical contrast, however, it is necessary to illuminate them with appropriate wavelengths in order to activate the fluorescence phenomenon [37].

In Figure 3.5 it is shown an example of a continuos tracers application. The biggest limitation of continuous tracers is that with the increase of the Reynolds number the motion of the tracer deviates more and more from that of the fluid. These methods are therefore limited to laminar flows at low-Reynolds-numbers [33] [37]. Furthermore, the continuous tracer does not allow information to be obtained in the entire field of motion, but only along the flow line in which it is located until it then disappears due to diffusion in the fluid. In the Table 3.1 are summarized the most important characteristics of continuos tracers.

In the following Figure 3.6 are shown same optical and physical properties of most used continuous tracers and their comparison with water properties.

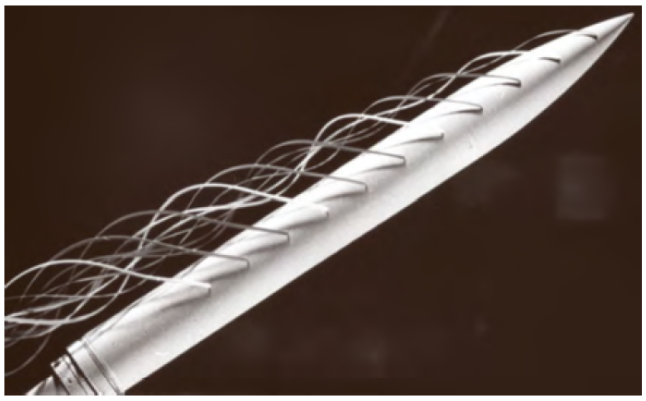

Figure 3.5: Dye lines in the vortex flow behind a yawed cylindrical model. The fluid is water, the dye is a mixture of ink, milk, and alcohol (courtesy of Deutsch-Französisches Forschungsinstitut, ISL, St.Louis, France) [33].

Aqueous solutions of	n	ρ/ρ_0	μ/μ_0
Glycerin	1.33–1.47	1.0–1.26	1.0–1490
Zinc iodide	1.33–1.62		
Sodium iodide (60%)	1.5		
Sodium thiocyanate	1.33–1.48	1.0–1.34	1.0–7.5
Potassium thiocyanate	1.33–1.49	1.0–1.39	1.0–2.4
Ammonium thiocyanate	1.33–1.50	1.0–1.15	1.0–2.1
Organic liquids			
Kerosene	1.45	0.82	
Silicone oil mixture	1.47	1.03	190
Paraffin oil	1.48	0.85	
Turpentine	1.47	0.87	1.49
Soybean oil	1.47	0.93	69
Olive oil	1.47	0.92	84
Castor oil	1.48	0.96	986

Figure 3.6: Table of properties of most common used tracers; n=refractive index; ρ=density; μ=viscosity; ρ_0 (1000 kg/m^3) and μ_0 (1 cP) are the reference values of water at 20°C [33].

Pros	**Cons**
Ready availability	Fast diffusion in the working fluid
Low cost	Difficulty in following the fluid motion accurately
Usable without expensive accessory instrumentation (i.e. laser)	Limitations to low-Reynolds-numbers applications

Table 3.1: Summary of advantages and disadvantages of continuous tracers.

3.3.2 Particle tracers

Techniques based on the use of particle tracers (i.e. PIV, see section 3.5) are indirect as those that use continuous tracers, since the velocity of the particles is determined instead of that of the fluid. In the following sections principal dynamic and optical properties of particles will be discussed.
It is important to remember that by adjusting particles characteristics, improvements in the results of flow visualization techniques can be achieved. Furthermore, since this type of tracers is discrete, it allows to obtain a distribution with uniform concentration throughout the fluid, in this way a more uniform signal will be obtained in the visualization, compared to the use of a continuous tracer. For a complete discussion the reader is referred to [32].

Dynamic properties

When particles are dispersed in a fluid flow the most important force that influence the motion of the particles is the gravitational force. Approximating the motion of spherical particles in a viscous fluid at very low Reynolds number it is possible to obtain [32]:

$$\boldsymbol{U_g} = d_p^2 \frac{(\rho_p - \rho)}{18\mu} \boldsymbol{g} \tag{3.1}$$

where U_g is the gravitationally induced velocity, $\boldsymbol{g}$ is the acceleration of gravity, μ is the dynamic viscosity of the fluid and d_p the diameter of particles. It is evident that in order to avoid the sedimentation of particles and inertial effects it is necessary the condition $\rho \simeq \rho_p$. This condition is easier to obtain in liquids than in gases where the density of particles is much greater than that of the fluid. For this reason, in gases it is necessary to choose a sufficiently small diameter to reduce the settling velocity of the particles.
The delay between the velocity of the particles and that of the fluid is called slip

velocity U_s and it is given by:

$$\boldsymbol{U_s} = \boldsymbol{U_p} - \boldsymbol{U} = d_p^2 \frac{(\rho_p - \rho)}{18\mu} \boldsymbol{a} \tag{3.2}$$

where $\boldsymbol{U_p}$ and $\boldsymbol{U}$ are the particle and fluid velocities, while $\boldsymbol{a}$ is the fluid acceleration. The solution of these equation reported on [32] is given by an exponential function from which it is possible to obtain the response time of the particle immersed in the fluid τ_p:

$$\tau_p = d_p^2 \frac{(\rho_p - \rho)}{18\mu} \tag{3.3}$$

It is important to remember that in case of large particles or high flow velocities the solution is not an exponential, but have a non-linear solution. τ_p is related to the exponential decay of the particle velocity due to drag motion and it is used to calculate the number of Stokes:

$$Stk = \frac{\tau_p}{\tau_f} \tag{3.4}$$

where τ_f is the characteristic time scale in the flow. It is reported by literature that values of Stokes number below 10^{-1} make the motion of the particles approximate that of the fluid with good accuracy [38]. In order to have a sufficiently low number of Stokes it is necessary that the density of the tracer is similar to that of the fluid (neutrally buoyancy condition). In fluids such as water this is easily achieved with polyamide particles or hollow glass spheres. In gases the condition is not verified and consequently it is necessary to reduce the diameter of the particles, worsening the scattering properties (see section 3.3.2). Considering the high viscosity of the water and the relatively low velocities in the experiments with liquids it is possible to use particles in the range between ($10\mu m$ and $100\mu m$) [32]. In Figure 3.7 some of the most commonly used particles in liquid applications are shown.

Type	Material	Mean diameter in µm
Solid	Polystyrene	10–100
	Aluminum flakes	2–7
	Hollow glass spheres	10–100
	Granules for synthetic coatings	10–500
Liquid	Different oils	50–500
Gaseous	Oxygen bubbles	50–1000

Figure 3.7: List of most used materials for seeding liquids [32].

Optical properties

In images obtained from visualization techniques such as PIV, the contrast between fluid and particles is directly proportional to the power of the scattered light [32]. To increase the intensity of the scattered light it is necessary to increase the power of the illumination source (i.e. laser), or it is possible to carefully choose the particles based on their optical properties. Clearly the second solution makes it possible to significantly reduce costs. The main parameters that influence the intensity of the scattered light are: size, shape, orientation of the particles and also the ratio between the refractive index of the particles and the fluid.
In order to describe the scattering properties of particles, some aspects of Mie's scattering theory will be described. The theory is valid if the particles are approximated to spheres and the diameter d_p is greater than the wave length of incident light λ. According to Melling [39], a convenient measure of the (spatially integrated) light scattering capability is the scattering cross section C_s, defined as the ratio of the total scattered power P_s to the laser intensity I_0 incident on the particle:

$$C_s = \frac{P_s}{I_0} \tag{3.5}$$

In particular C_s is linked to the ratio $\frac{d_p}{\lambda}$ with a relationship of direct proportionality (as it is shown in Figure 3.8).

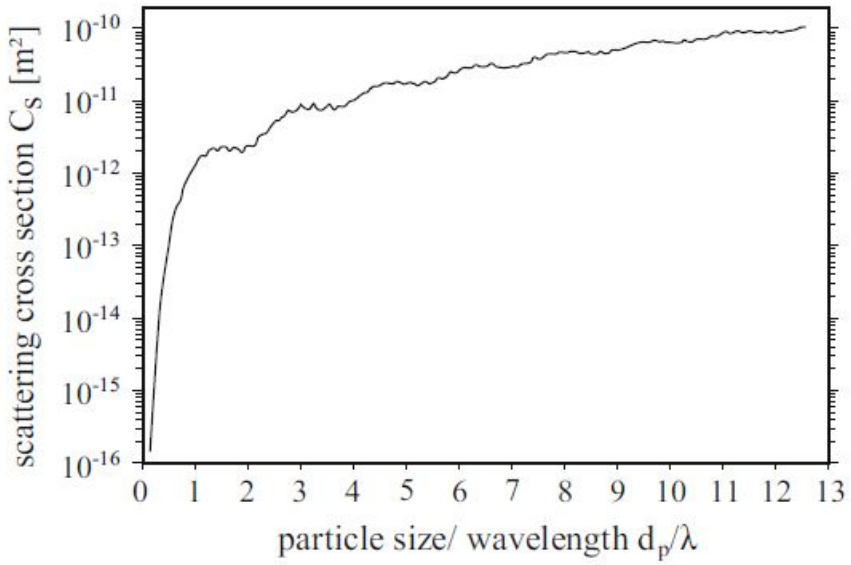

Figure 3.8: Variation of C_s with respect to d_p [32].

Another term that characterizes Mie's theory is the normalized diameter X_m:

$$X_m = \frac{\pi dp}{\lambda} \tag{3.6}$$

This parameter give informations on the ratio between forward and backward scattering, so in order to have an high efficiency in forward scattering it is necessary to increase X_m [32]. In Figure 3.9 the scattering intervals: Rayleigh (X_m<1), Geometrical Optics (X_m>90) and the intermediate interval (Mie region) are represented. The non-monotone trend of the scattered intensity as d_p varies can be seen as the superimposition of various scattering orders (i.e. reflection, first order refraction). For insights on the topic see [40].

The scattering efficiency is also given by the ratio between the refractive index of the particles and that of the fluid. Since the refractive index of water is much greater than that of air, the intensity of scattering in air is one order of magnitude greater. For these reasons, when conducting experiments with particles seeded in water, it is necessary to choose sufficiently large diameters d_p. Since the relation $\rho \simeq \rho_p$ is valid in liquids for the reasons described above, it is allowed to choose a

larger d_p, generally up to 100 μm, as the one used in the experiments described in Chapter 5.

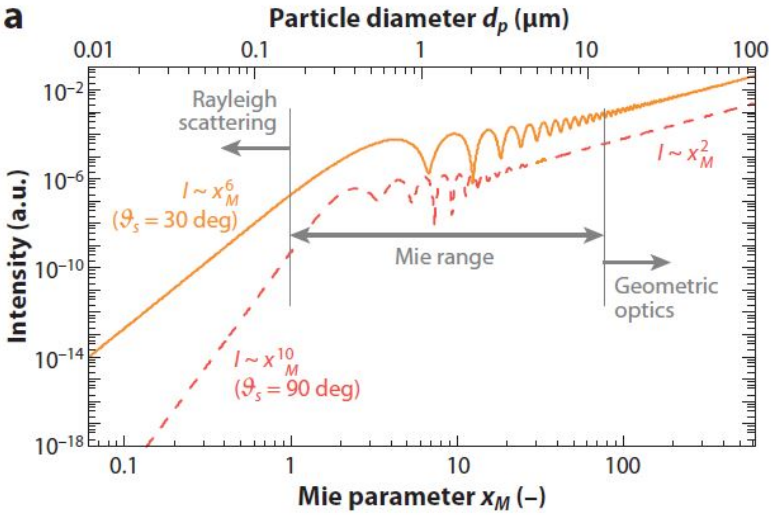

Figure 3.9: Variation of scattering intensity as function of X_m for two scattering angles [40].

Figure 3.10 show the representation of the normalized scattering intensity in Mie region (λ=532 nm) for different glass particle sizes in water. As can be noted the maximum values of light intensity scattering are obtained for observation angles of 180 degrees. However, a sufficient amount of scattered light intensity is achieved even at viewing angles of 90 degrees. In 2D PIV techniques it is important that the camera is aligned orthogonally to the illumination plane of the motion field in order to avoid measurement uncertainties caused by blurred particle images due to the limited depth of focus of the imaging system, for more information on the topic the reader is referred to [32].

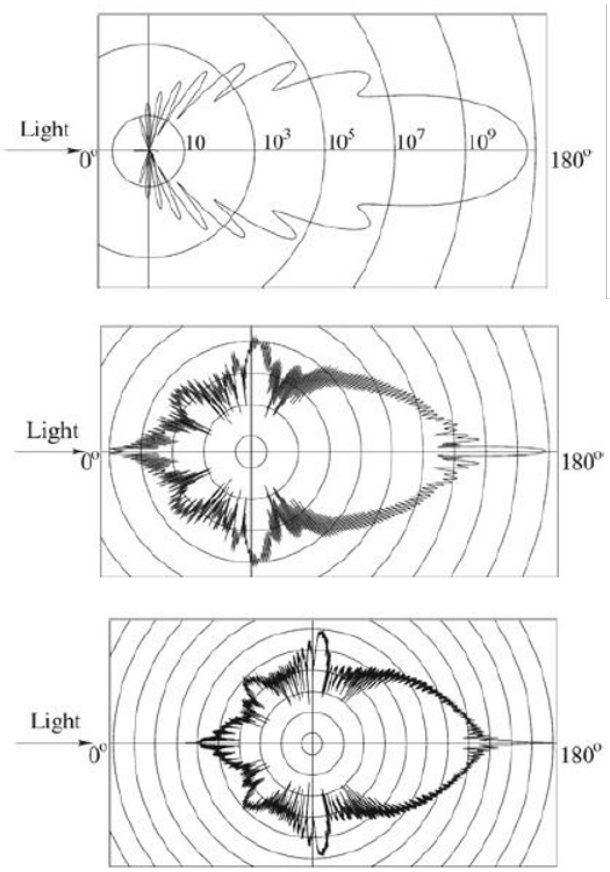

Figure 3.10: First image: light scattering by 1 μm glass particle in water. Second image: light scattering by 10 μm glass particle in water. Third image: light scattering by 30 μm glass particle in water[32].

To summarize in a few words the concepts underlying the choice of the type of particles to inseminate fluids in visualization techniques, it is possible to state:

- Need for sufficiently small particles in order to correctly follow the fluid motion.
- Need for particles large enough to scatter enough light.

It is clear that these two statement are in contrast each other, so it is necessary to choose an appropriate trade off between the two, according to the specific case of study.
In Table 3.2 are summarized the most important characteristics of discrete tracers.

Pros	Cons
Better accuracy in following the fluid motion	High cost
Controllability of experiments (adjusting dynamic and optical properties)	Often required expensive accessory instrumentation (i.e. laser)
Diffusion in the fluid slower with respect to continuous tracers	Difficulty of use (choice of suitable dynamic and optical parameters)

Table 3.2: Summary of advantages and disadvantages of particle tracers.

3.4 Particle Imaging

In this section it is described the main equations underlying Particle Imaging, that is, the visualization of particles through a camera. The Figure 3.11 shows a typical arrangement for acquiring images of tracers moving in a fluid flow and this configuration is implementable for various flow visualization techniques such as PIV (see section 3.5) and Optical Flow (see section 3.6).

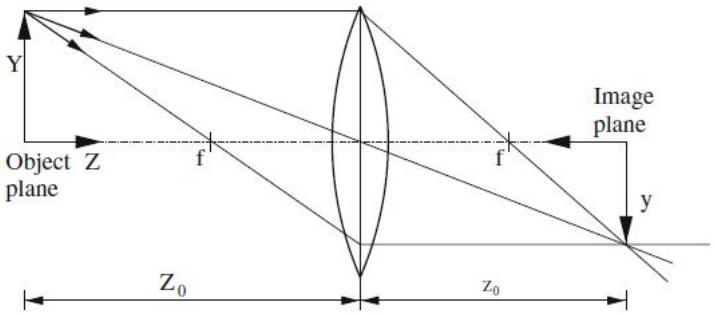

Figure 3.11: Representation of the relation between Object plane and Image plane which is the basis of optical techniques [32].

An important parameter to define is the magnification factor M:

$$M = \frac{z_0}{Z_0}; \tag{3.7}$$

It is given by the ratio of the distance between the image plane and the camera lens z_0 and the distance between the camera lens and the object plane Z_0. M can be defined as the factor that links the object with his projection on the image plane [32]. For a thin lens immersed in air, focal length f (represented in Figure 3.11) is the distance from the center of the lens to its focal points. The relation between f, z_0 and Z_0 is given by the thin lens equation:

$$\frac{1}{f} = \frac{1}{z_0} + \frac{1}{Z_0}; \tag{3.8}$$

Once the particles in the motion field have been captured by the camera, it is important to evaluate the actual size of the particles in the image plane. The image of a finite-diameter particle is given by the convolution of the point spread function with the geometric image of the particle [32]. Neglecting the aberrations of the lens and approximating the diffusion function of the point to the Airy function it is obtained:

$$d_\tau = \sqrt{M^2 d_p^2 + d_{diff}^2}; \tag{3.9}$$

The equation is dominated by two terms: the first represents the size of the geometric image of the particle, while the second is given by the diffraction limited minimum image diameter:

$$d_{diff} = 2{,}44 f_n (1 + M)\lambda \tag{3.10}$$

where f_n is the f-number of the lens, defined as the ratio between the focal length f and the aperture diameter D_a. For particles larger than a few microns and with high magnification values in the equation (3.9) the first term dominates [32]. According to [32, Raffel et al.] there are two main reasons why it is necessary to optimize image particle diameter:

- If d_τ is reduced, the error in velocity estimation in PIV techniques is reduced.
- I_{max}, or the light energy per sensor area at constant light energy scattered by tracer particles is proportional to $1/d_\tau^2$.

The last important parameter to be consider in particle imaging techniques is the depth of field δZ which is the distance between the nearest and the farthest objects that are in acceptably sharp focus in an image and it is linked to the parameters described above by:

$$\delta Z = \frac{2 f_n d_{diff}(M+1)}{M^2} \tag{3.11}$$

In accordance with the above equations and as shown in Figure 3.12 it is possible to note that to reduce d_τ it is necessary to have D_a large and therefore f_n small, but this involves a reduction of δZ [32].

$f_n = f/D_a$	d_τ [µm]	δ_Z [mm]
2.8	4.7	0.5
4.0	6.6	1.1
5.6	9.1	2.0
8.0	13.0	4.2
11	17.8	7.8
16	26.0	16.6
22	35.7	31.4

Figure 3.12: Values of d_τ, f_n and δZ for imaging of small particles ($\lambda = 532$ nm, $M = 1/4$, $d_p = 1\mu m$)[32].

3.5 Particle Image Velocimetry

Particle image velocimetry (PIV) is a non-invasive imaging technique that allows to derive the motion field of a fluid seeded with tracer particles. The fluid velocity is determined indirectly by measuring the displacement (Δx) of tracer particles between two successive time instants t_1 and t_2. The velocity of the particles between two successive instants is simply given by the relation:

$$V = \frac{\Delta x}{\Delta t}, \tag{3.12}$$

where Δt is the time distance between t_1 and t_2. The determination of the Δx is carried out through cross-correlation techniques and will be presented in the next

section [41], [42].

The PIV technique allows to obtain the average displacement of the particles inside an interrogation window (I_w) according to an Eulerian-type approach, instead there are techniques to detect the displacement of single particles, such as PTV (Particle tracking velocimetry) using a Lagrangian-type approach [42] [32] [41]. In Figure 3.13 it is shown a typical PIV imaging system (2C-2D PIV) for determining the two components of the velocity field on the imaging plane, there are also techniques for determining the three component of the velocity field in 3D space but they will not be covered in this Chapter. The experimental set up for a PIV application can

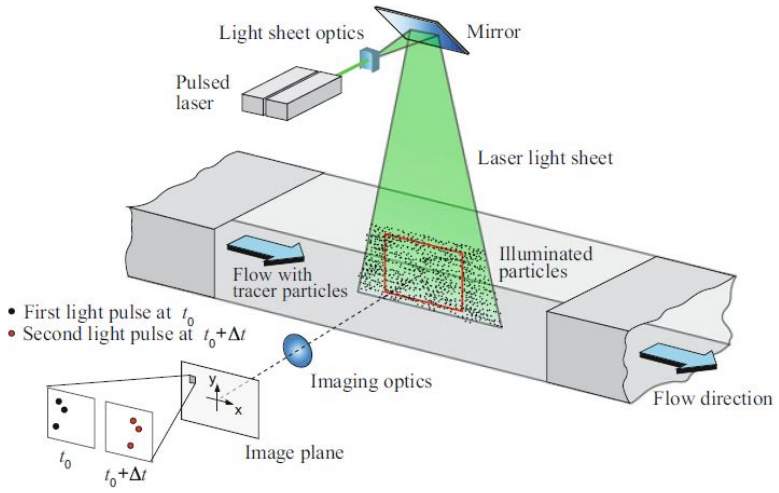

Figure 3.13: Experimental system for 2C-2D PIV in a wind tunnel [32].

be divided into various subsystems:

- Tracer particles;
- Illumination system;
- Recording system;
- Calibration;
- Evaluation of particles displacement;
- Post-Processing.

3.5.1 Seeding

The tracer particles must be chosen in such a way as to be able to approximate in the best possible way the motion of the fluid, as described in section 3.3.2. For seeding liquids it is sufficient to mix an appropriate concentration of particles with the working fluid. It is necessary to reach a determined tracer concentration in order to have a sufficient number of particles in the PIV images to have loss of information on the displacement of the tracer and consequently on the movement of the fluid. However, if too high tracer concentrations are reached, spekle phenomena may occur, which cause errors in the estimation of displacements due to interference between the various scattering contributions of the particles [42].

3.5.2 Sources of illumination

The plane of interest within the fluid flow is illuminated in the two time instants t_1 and t_2 by means of a sheet of laser light. The time delay between pulses Δt must be chosen with respect to the flow velocity and the magnification at imaging [32]. In general Δt must to be choose in order to obtain maximum particle displacements of about 10 pixels, higher displacements can lead to errors in the estimation of the velocity field, furthermore this condition is also valid for the Optical flow techniques discussed in Chapter 4.
The laser is collimated through a lens system and must illuminate the motion field so as not to excessively lose the movement of the particles out of the plane. Another parameter of the lighting source that must be set is the pulse width δt, which is the duration of the pulse. This parameter affects the visibility of the tracer and generally if it is small it allows to freeze the movement of particles and represent them as sharp dots in the images, otherwise streaks will be obtained in the PIV images [38]. As explained in the section 3.3.2 in applications with liquids, larger particles can be used, which scatter more light than particles with a diameter of 1 μm, which are usually used in air streams. These conditions are equally valid for the case study presented in this work in which a solution of water and glycerol at 33% v/v was used as the working fluid. In these cases it is possible to use light sources with significantly lower peak power, such as continuous shutter (CW) lasers,

high-power LEDs and flash lamps. This means that the experimental requirements and costs are more relaxed for PIV applications in water than in air [32].

3.5.3 Recording system

Before recording the motion field it is necessary to perform a calibration of the system to determine the relationship that links the movement of the particles in the object plane to the movement of them in the image plane. The light scattered by the moving particles is captured by a camera in the two instants of time t_1 and t_2, the frames corresponding to the two instants of time are subsequently processed to obtain the displacement of the particles.
The most used cameras are CCDs (charge couped devices), or the most recent CMOS (Complementary Metal Oxide Semiconductor) which have an increase in SNR (signal-noise ratio) and higher temporal resolution. The sensors of the camera are formed by a grid of pixels, which allow to convert the photons constituting the light scattered by the particles into electrons which will then form the digital signal. CCD cameras present pixels dimensions of about 5x5 μm^2 and acquisition rates up to 50 Hz, instead CMOS have pixels dimensions of 20x20 μm^2 and acquisition rates until 10 kHz [38].

3.5.4 Evaluation of particle displacement

In this phase, the digital images obtained in the various instants of time are divided into interrogation windows I_w and their size will determine the spatial resolution of the motion field. The displacement vector of particles in each I_w is determined by using statistical methods such as cross-correlation. As reported in [43], each I_w in the two images corresponds to an intensity function in 2D, $I_{t1}(X)$ and$I_{t2}(X)$ where $X = (x, y)$. The particle displacement Δx is calculated by cross-correlation between I_{t1} and I_{t2}:

$$R(\Delta x) = \int I_{t1}(X) I_{t2}(X + \Delta x) dX, \tag{3.13}$$

The function R is essentially a measure of the degree of correspondence between the two intensity functions for a given spatial displacement. The highest peak in the

correlation map represents the most likely displacement within each interrogation window [32] [41] [44]. In other words the Δx value that maximizes R is equivalent to the average displacement of the particles inside the I_w. In Figure 3.14 are summarized all the steps for determining the particle displacement.

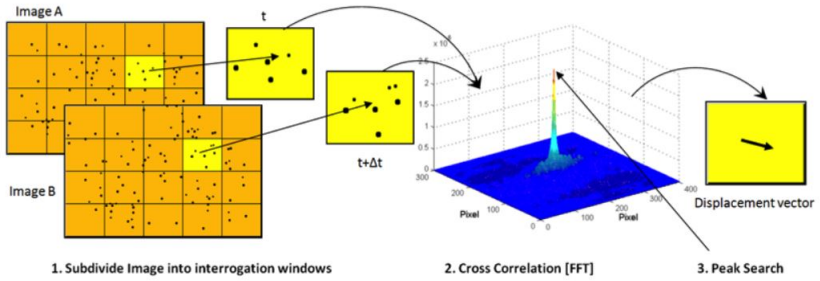

Figure 3.14: Schematic representation of division in I_w, computation of cross correlation function and peak search [45].

3.5.5 Temporal and Spatial resolution

The temporal resolution of a PIV system is mainly dependent to the maximum acquisition frequency of cameras and repetition rates of lasers. The recent development of dedicated high-speed lasers and high-speed cameras allows time resolved measurements of most liquid and low-speed aerodynamic flows [32]. The distance between adjacent independent vectors defines the spatial resolution of the PIV measurement. The spatial resolution of the motion fields is mainly linked to the size of the sensor, i.e. the number of pixels that compose it.
Another parameter to consider is the size of the interrogation windows, which determine the number of independent velocity vectors in the motion field and therefore the maximum spatial resolution obtainable at a given spatial resolution of the sensor.
Furthermore, PIV systems are divided into two main types, namely "Low speed" systems and "High speed" systems. High speed systems have the advantage of being able to perform time-resolved measurements, in such a way as to follow the movement of particles instant by instant. The setup presented in this thesis, through the

use of a mobile phone as a camera (see Chapter 5), allows to realize time-resolved acquisitions. The advantage of this type of acquisition is the possibility of carrying out various types of post processing of the results, such as the calculation of the acceleration of the particles, starting from their velocity.

3.6 Optical Flow

A different technique that will be discussed and implemented in this thesis work concerns the Optical flow (OF). As mentioned in [46] "The optical flow is defined as the velocity field in the image plane that transforms one image into the next one in a time sequence."
The presented technique can be used to calculate the velocity field of a fluid seeded with a tracer, which moves inside a pipe. In literature there are not yet many applications of this method to fluid motion, because it is usually used to detect and track moving solid objects. Similarly to the PIV technique, to apply this method it is first necessary to record the motion of the tracer that moves inside the fluid and subsequently the velocity field will be calculated starting from the series of subsequent frames. In fact the OF tries to reconstruct the motion of an object starting from a pixel grid, that is its representation through the image acquired with the camera.
Figure 3.15 shows an example of the application of OF to two different pairs of frames.

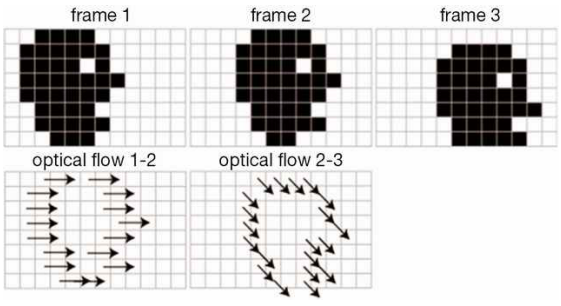

Figure 3.15: Example of an application of OF to two pairs of different frames [47].

For the first pair of images it is noted how the represented figure has moved from left to right and this is represented in the first result of the OF. In the second case, in addition to a translation from left to right, the figure also moves from top to bottom and this can be seen in the result of the OF. Knowing the motion of each pixel and the time interval between the two analyzed frames, it is possible to derive the speed with which the pixel has moved from one frame to the next.

3.6.1 Theory of OF

The fundamental assumption of this algorithm is based on the constancy of brightness between two frames in a sequence. The intensity of the image is a two-dimensional function of the space (x, y) and of the time (t), as a consequence the variation of the intensity between two consecutive images can be expressed by the general equation of OF as follows [48]:

$$I(x, y, t) = I(x + \delta x, y + \delta y, t + \delta t) \tag{3.14}$$

$I(x, y, t)$ is the intensity of the image, that is the two-dimensional distribution of the light intensity between two frames in a sequence, δt is the time separation between the two frames and δx, δy represent the horizontal and vertical displacement. Figure 3.16 represents what is described in the equation 3.14, namely the constancy of the light intensity of the particle as it changes position in the two-dimensional space of the image.

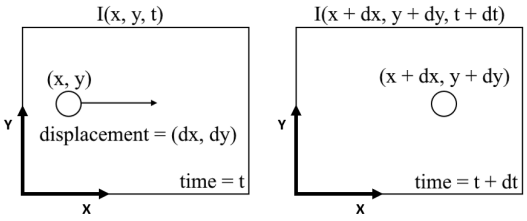

Figure 3.16: Graphic representation of the general equation of the OF.

The velocity vectors along the principal axes are obtained from the Taylor series approximation of equation 3.14 [48]:

$$I(x + \delta x, y + \delta y, t + \delta t) = I(x, y, t) + \frac{\partial I}{\partial x}\partial x + \frac{\partial I}{\partial y}\partial y + \frac{\partial I}{\partial t}\partial t + \Theta(I) \tag{3.15}$$

Assuming that the terms of higher degree are negligible, the derivative of I with respect to time can be calculated as follows [49]:

$$\frac{\partial I}{\partial t} = \frac{I(x+\delta x, y+\delta y, t+\delta t) - I(x,y,t)}{\partial t} = \frac{\partial I}{\partial x}\frac{\partial x}{\partial t} + \frac{\partial I}{\partial y}\frac{\partial y}{\partial t} + \frac{\partial I}{\partial t} \tag{3.16}$$

finally from 3.16 it is possible to obtain the general equation of OF:

$$\frac{\partial I}{\partial x}u + \frac{\partial I}{\partial y}v + \frac{\partial I}{\partial t} = 0 \tag{3.17}$$

where u and v represent the horizontal and vertical component of the velocity field of the OF. In the equation 3.17 the image intensity gradient are known variables and are given by the image sequence (frames). By observing the equation (3.17), it is evident that there are two unknowns (u, v) for one constraint, so it is impossible to determine the components of the velocity. For this reason, as it is shown by [46, Horn and Schunck, 1981], it is necessary to add another constraint. Depending on the method that is used to introduce a further equation, the OF is divided into Sparse Optical Flow and Dense Optical Flow. The solution methods most used to add a constraint to the equation (3.17) are:

- Lukas Kanade [50, Lukas and Kanade, 1981].
- Horn and Schunk [46, Horn and Schunck 1981].
- Block Matching [51, Zhang and Guojun, 2000].
- Farneback [52, Farneback, 2003].

For a more detailed discussion of the following methods, please refer to the articles mentioned above.
In the next Sections the method chosen, in this thesis work, will be described to solve the equations of the OF by adding a further constraint.

3.6.2 Introduction to the OF method

The first studies that attempted to find a solution to the open problem of optical flow were Horn-Schunck [46]. Their assumption is based on considerations on the

motion of an object. In particular, the two scientists observed that nearby points in an object move at approximately the same speed. In particular, their assumptions are based on the variation of the light intensity which varies gradually for nearby points of an object and not with abrupt variations.
One way of expressing the additional equation is to minimize the square of the intensity of the speed gradients of the OF and calculate the error defined as:

$$E = \left(\frac{\partial u}{\partial x}\right)^2 + \left(\frac{\partial u}{\partial y}\right)^2 + \left(\frac{\partial v}{\partial x}\right)^2 + \left(\frac{\partial v}{\partial x}\right)^2 \tag{3.18}$$

For a more detailed description of the method proposed by Horn-Shunck for the solution of the OF equation, the reader is recommended to refer to [46]. The method that has been implemented is based on a different approach to the solution of the open problem of the OF. In particular, the Horn-Schunck constraint is used as a basis for developing the solution of the method described in the following Sections.

3.6.3 Phisical meaning

The key to attribute a physical meaning to the OF equation (3.17) is the consideration that the intensity of the image is proportional to the radiation projected into the camera which is positioned at a precise point in space. In this way it is possible to state that the relative radiation can be replaced with the relative intensity of the image. Different types of projected-motion equations for different flow visualization are well described in [53]. For example, laser-sheet induced fluorescence, transmittance through transported passive scalar, schlieren, shadowgraph and trasmittance imaging in density varying flows, transmittance, scattering of particulate flows and laser-sheet visualization of particle in flows. Reformulating the equation (3.17) it is possible to obtain a general equation that describes the phenomena listed above:

$$\frac{\partial g}{\partial t} + \boldsymbol{\nabla} \cdot (g\boldsymbol{u}) = f\left(X_1, X_2, g\right), \tag{3.19}$$

where $\boldsymbol{u} = (u, v)$ is the velocity in the image plane referred to as the OF, $g = g(I)$ is a function of the intensity which, as mentioned before, it is proportional to the radiation received by the camera. For a more in-depth discussion on the physical

meaning of $g(I)$ it is recommend reading the Appendix A of [53]. The term ∇ is the spatial gradient and $f(X_1, X_2, g)$ is dependent on the specific flow visualization technique as described earlier.
In the special case where $g\nabla\cdot\boldsymbol{u} = 0$ and $f = 0$, (3.19) is reduced to the Horn-Schunck brightness constraint equation that is [54]:

$$\frac{\partial g}{\partial t} + \boldsymbol{u} \cdot \nabla g = 0 \tag{3.20}$$

3.6.4 A Variational Formulation

To obtain an equation with physical meaning, it is possible to hypothesize to project the Navier-Stokes equations in the image plane to obtain a constraint that allows to solve the OF. However, this would entail considerable analytical complications. Hence, the Horn-Schunck constraint is used for its simplicity.
Taking into account these considerations and combining the two constraint equations (3.18) and (3.19) previously obtained it is possible to define a functional:

$$\boldsymbol{J}(\boldsymbol{u}) = \int_\Gamma \left[\frac{\partial g}{\partial t} + \boldsymbol{\nabla}\cdot(g\boldsymbol{u}) - f\right]^2 dx\,dy \; + \lambda \int_\Gamma \left(|\boldsymbol{\nabla} u|^2 + |\boldsymbol{\nabla} v|^2\right) dx\,dy \;, \tag{3.21}$$

where λ is the Lagrange multiplier and Γ is an image domain.
By minimizing 3.21 it is possible to obtain the Euler-Lagrange equation:

$$g\nabla\left[\frac{\partial g}{\partial t} + \nabla\cdot(g\boldsymbol{u}) - f\right] + \lambda\nabla^2\boldsymbol{u} = 0 \tag{3.22}$$

For solving the equation above is necessary to use the standard finite difference method with the Neumann condition $\frac{\partial u}{\partial n} = 0$ on the image domain boundary for the optical flow [54, 53].

3.6.5 Error Analysis

Error estimated for PIV images

A formulation of the error, in the case of using particle images typically used in the field of PIV analysis, is described in [55].

As described previously in this Chapter 3 in typical planar PIV measurements, a thin laser sheet is used to illuminate particles seeded into the flow, and the light scattered by these particles is perpendicularly recorded by a camera.
As reported in [54], the use of images with particles not distributed uniformly can create a challenge for the results obtainable with the OF especially in the case of large displacements. In general, the particle displacement should be small in optical flow computation using particle images, particularly in regions of large velocity gradients. The total error relate to the use of OF with the particles, is mainly influenced by some parameters. In fact, it is directly proportional to the particles displacement and particle velocity gradient, while it is inversely proportional to the particle image density [54]. An in-depth discussion on the topic described briefly and on the relationship between particle velocity and OF is provided in [55], [54].

General error in the OF

As reported in the [55], it is possible to make a general estimate of the error committed by the algorithm under investigation that is expressed by the following equation:

$$\epsilon = \|\Delta x\| \sqrt{\frac{C_1}{\|\nabla g\|^2 \|\boldsymbol{u}\|^2} + C_2 \|\nabla \boldsymbol{u}\|^2}, \tag{3.23}$$

In the equation C_1 and C_2 are two coefficients that must be determined during the iterations to estimate the error, $\|\Delta x\|$ is the observed displacement, and as can be seen from the equation small displacement are required to have good performances because the error is directly proportional to the displacement itself. $\|\Delta g\|$ is the image intensity gradient while $\|\Delta \boldsymbol{u}\|$ is the velocity gradient. Since these two terms are present in the equation, the error turns out to be a function locally dependent on these quantities. The error increases in areas where there are large changes in the velocity gradient or small changes in the intensity gradient. The magnitude of the speed also contributes to the determination of the error, which must be small to contain the error [55].

Taking into consideration the theoretical discussion presented in this Chapter, is it possible to adapt these techniques in order to implementing a methodology that allows to visualize and study the velocity field of a fluid within coronary artery phantoms?

Chapter 4

Analysis methods

In this Chapter there is a description of the OF and PIV algorithms used to analyze the data acquired from the imaging system of the setup which will be described in the next Chapter. The Chapter is divided into two main parts, each dedicated to the description of one of the methods. The first part presents a description of a method of closing the open equation of OF that has been implemented for application in Matlab by [54, Liu et al., 2017]. In turn, this part of the Chapter is divided into the main parts that describe the steps present within the algorithm and that allow to obtain the solution of the OF equation showing same examples demonstrating the effectiveness of OF in flow diagnostics. The second part of the Chapter presents the description of the PIVlab open source software with settings chosen for the specific case treated in this project. During the description of the various settings selected in this section there is a brief description of their function within the algorithm. Finally, there is a comparison between the two algorithms.

4.1 OF Algorithm

In this section it is proposed the description of the algorithm used for this work that is based on the solving of the OF equation and in particular it is focused on the resolution of equations (3.19) and (3.22). All the code implemented in Matlab is open source and it can be found in the work presented by [54]. Every section of

the algorithm has been analysed and modified to fit it for calculating of velocity field from video frames of a blood mimicking fluid trough a coronary artery model as it will be described in Chapter 5.

4.1.1 General description

The program is composed of one principal code "Flow_Diagnostic_Run.m" and some functions that are called in the main script.
The heart of the code consists of a large iterative cycle that allows to acquire, two at time, a predetermined number of consecutive frames. The input images can be in different types of formats like *".tif", ".jpeg", ".jpg", ".bmp"* etc..
The most important steps of the code are summerized below:

1. Loading of the frame n and n+1 that are called Im1 and Im2;
2. Converting the image to grayscale;
3. Selection of idex region:
   - If is set to 0 the program will analyze all the image;
   - If is set to 1 the user can choose a window of analysis selecting the region of interest from the original image.
4. Correction of the global and local intensity change in images;
5. Pre-processing for reducing random noise and downsampling images if displacements is too large;
6. Solving of the Horn and Schunck OF equation using a specified routine;
7. Solving of Euler-Lagrange equation (3.22) using a specified routine;
8. Coarse-to-fine iteration:
   - Generation of the shifted version of the Im1 image from based on the initial coarse-grained velocity field "$(ux0, uy0)$";

- Calculation of velocity difference for iterative correction in order to obtain a refined velocity field.

9. Plot of the images, velocity vector, and streamlines in the initial and refined estimations;

10. Plot of the velocity magnitude fields;

11. The cycle restarts from the next iteration analyzing the image n and n+1.

In this way, a time-resolved solution of the velocity field is obtained. The most important section of the code starts with the resolution of Horn-Schunck OF equation (3.19) that is used as initial approximate solution in the solving of the Euler-Lagrange equation (3.22) for a faster convergence. Values of ux0 and uy0 (showed in the tables below) are the coarse-grained velocity components obtained from the downsampled images in the coarse-to-fine process which returns as output the refined velocity components "ux_corr" and "uy_corr".
All the results plotted by the algorithm are showed in $pixels/\Delta t$, where Δt is the time-interval between the next two frames (Im1 and Im2), for these reasons to give a unit of measurement with a physical meaning (i.e. m/s) a system calibration is required. To carry out the calibration, the model represented in the images was measured through the use of a caliper. Then the number of pixels corresponding to that determined measurement in Matlab was manually checked. In this way, by carrying out the relationship between the two quantities, the scaling factor was obtained which allowed to pass from pixels to mm. Tables 4.1 and 4.2 respectively describe the data to be supplied as input and the respective output data obtained by applying the described routine.

Input files and parameters	**Notation**	**Unit**	**Note**
image pair	Im1, Im2	–	tif, bmp, jpeg etc.
Lagrange multipliers	lambda_1, lambda_2	–	regularization parameter
Gaussian filter size	size_filter	pixel	removing noise
Gaussian filter size	size_average	pixel	correction for illumination
Scale factor for down sampling of original images	scale_im	–	reduction of initial image size in coarse-to-fine
Number of iterations	no_iteration	–	iteration in coarse-to-fine scheme
Indicator for regional diagnostics	index_region	–	"0" for whole image "1" for selected region

Table 4.1: Table of input and parameters [54].

Output files	**Notation**	**Unit**	**Note**
coarse-grained velocity	ux0, uy0	pixels/unit-time	based on downsampled images
refined velocity	ux_corr, uy_corr	pixels/unit-time	refined result with full spatial resolution in coarse-to-fine process

Table 4.2: Table of output parameters [54].

4.2 Pre-processing of the images

The Figure 4.1 shows a frame before having been subjected to the pre-processing phase, which allows to optimize the characteristics of the images before being used as input in the OF and PIVlab algorithms.
Following the acquisition phase, all the frames were extracted from the videos, for a total of 140 frames for each recording. Since with the camera acquisition mode (described in the Chapter 5) there is an initial and final part of the video in which the frame rate is lower than 960 Hz, the frames have been extracted only in the central part of each video.

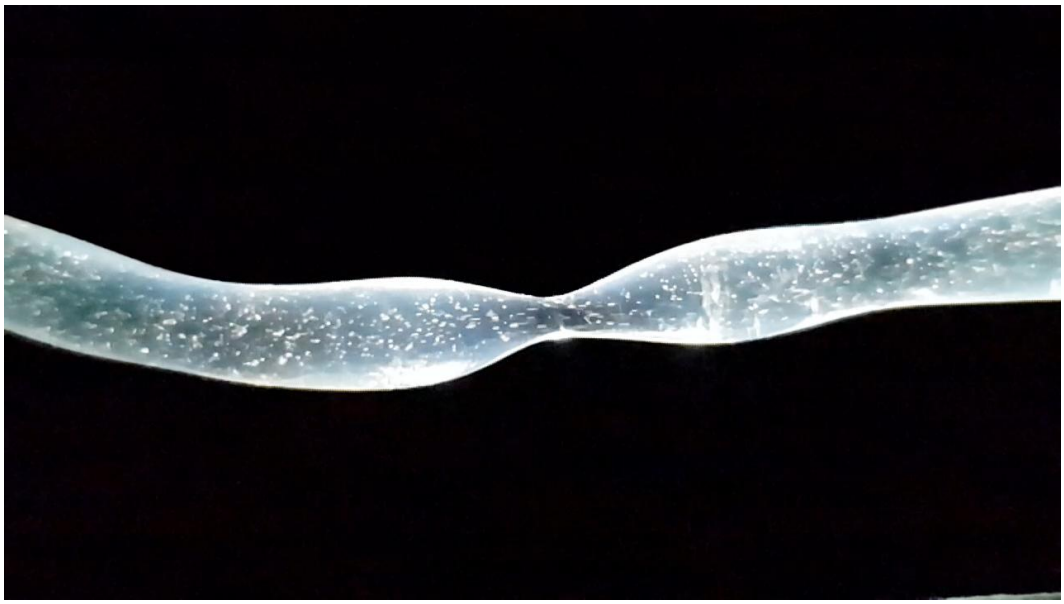

Figure 4.1: Example a frame extracted from the recordered videos.

The operations carried out on each frame, in the pre-processing phase, were the subtraction of the average of the images, calculated on 4000 frames (corresponding to the 30 videos acquired for each flow-rate value), and the multiplication by the standard deviation, always calculated on 4000 frames. This procedure made it possible to attenuate the noisy components inside the frames, such as light reflections at the edges and in the center of the vessels. This because there are peaks of light intensity that remain approximately constant between each frame in

all the sequence. The processing phase allowed to obtain a better visualization of the particles in the vessel and a greater contrast with the background, attenuating all the noisy components, as it has shown in Figure 4.2. However, due to the irregular geometry of the models and the refractive index of the material making up the vessels, some light reflections at the edges remained in the frames even after processing.

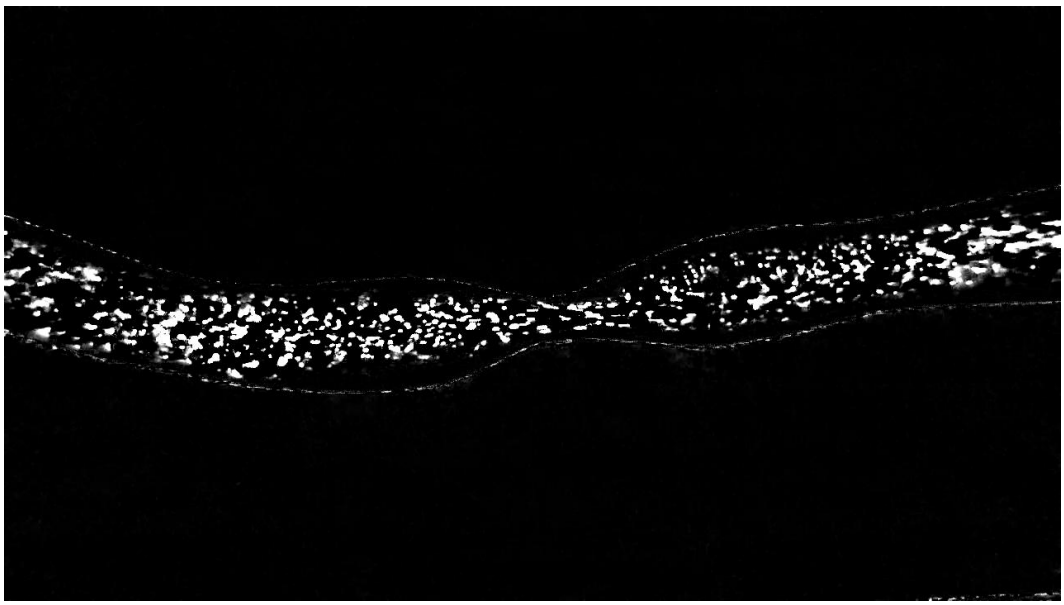

Figure 4.2: Example of the same frame of figure 4.1 after pre-processing procedure.

4.2.1 OF pre-processing

In order to remove random noise in images has been used a Gaussian filter and in the main program it is possible to choose the standard deviation of the filter in *pixels* units setting the parameter "size_filter" and the std of the Gaussian filter is 0.6* "size_filter". For our case of study this parameter has been set at 4 pixels.
All the theory under this method is based on the assumption that the illumination light intensity must not change between the two frames (3.17). In order to reduce light intensity variations a "Correction_illumination" routine is provided.
In the subroutine that allows to correct errors due to lighting defects, these corrections are first made by normalizing the entire image. The lighting corrections

are then corrected by applying a Gaussian filter. When the size of a filter is too large, the local variation associated with the illumination intensity change in images cannot be corrected. On the other hand, when the filter size is too small, the apparent motion of patterns/features in the two images would be artificially reduced after the procedure is applied. The selection of the filter size is a trial-and-error process depending on the pattern of illumination change in a specific measurement and simulations on a synthetic velocity field are used to determine the suitable size [54].

4.2.2 Coarse-to-fine routine

As it is discussed by [54] and in the Error Analysis described in 3.6.5 this program work well when the displacement between frames are small. In fact when displacement are over 10 pixels the performance of the algorithm is reduced. For these reasons in the main program is implemented a coarse-to-fine iterative scheme in order to reduce error given by large displacements. The principal steps of the method are explained below:

1. Downsampling of images to have sufficiently small displacements;
2. Extraction of coarse-grained velocity field by applying the OF algorithm to downsampled images;
3. Generation of a synthetic shift image $Im1_{shift}$ using the coarse-grained velocity obtained;
4. Computation of the difference in velocity field between $Im1_{shift}$ and $Im2_{original}$;
5. Addiction of the difference between the velocities to the initial velocity field ;
6. Obtaining a refined velocity field by iterations.

To regulate the downsampled images is necessary to choose an appropriate value of "scale_im", for example in the described case "scale_im"=0.5 means that the original images are reduced to 50% of the original size.
The algorithm used for the generation of shifted images is an image-warping in

which a translation transformation is used for large displacements and the OF equation is used for sub-pixel correction [54].

4.2.3 Some examples

In order to show the quality of the results obtained with the method described in this section, some examples have been reported in [54] that allow to evaluate the potential of this method.

Oseen vortex pair in uniform flow

In these example are examinated two particle images of an Oseen vortex pair in a uniform flow. The particle images have size of 500 x 500 pixels and there are 1000 particles with a Gaussian intensity distribution with standard deviation $\sigma = 2$ $pixels$ and the mean characteristic diameter of particles is $d_p = 4$ $pixels$ and the particle image density is 0.04 $particles/pixel^2$ [54]. All the results of velocity fields

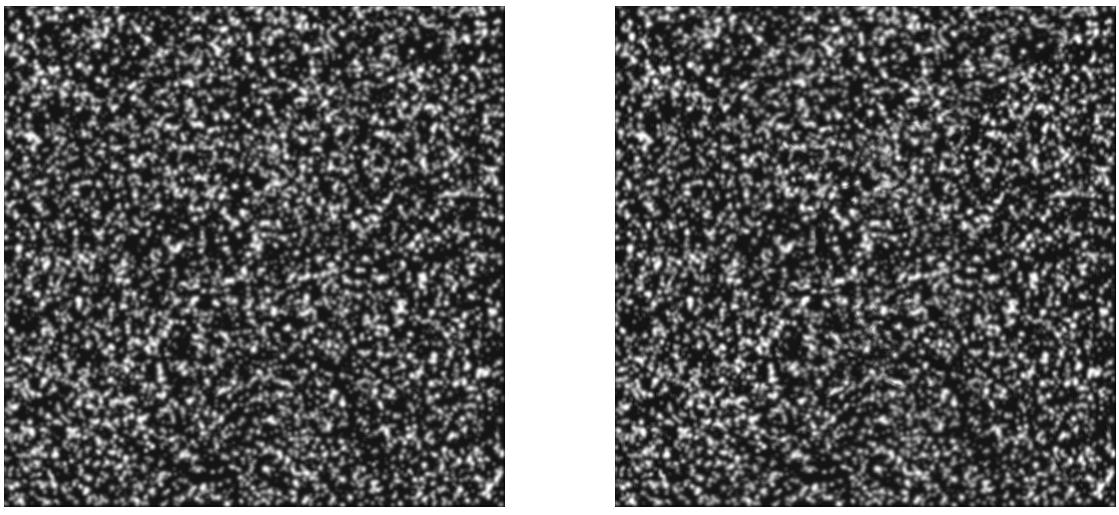

a b

Figure 4.3: A pair of particle images of an Oseen vortex pair in a uniform flow, (a) Image 1, and (b) Image 2 [54].

presented in this chapter are in $pixel/\Delta t$ as mentioned before and the velocity vectors are normalized for the maximum value.

Figure 4.4 (a) and 4.4 (b) show the refined velocity field and streamlines extracted from the two frames of Figure 4.3. The OF returns 500x500 vectors with a maximum displacement of 2.6 *pixels*. This example has been used as a typical case to quantitatively evaluate the optical flow errors in the parametric space through simulations. According to the dependence of the error from the particle displacement and particle velocity gradient, as described in 3.6.5, it was found that the error is larger near the vortex cores where velocity is maximum and its gradient is very large [54].

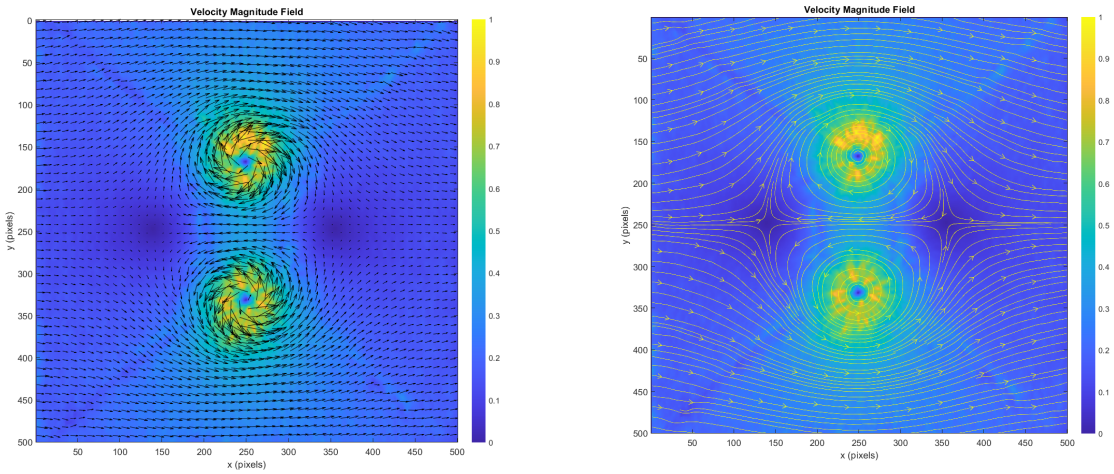

a b

Figure 4.4: Results of Velocity field (a) and Streamlines (b) of Oseen vortex pair in a uniform flow [54].

White Ovals on Jupiter

The White Ovals are distinct storms in the Jupiter's atmosphere. Figure 4.5 shows two successive images of the White Ovals. Three sets of images were taken on 02/19/1997 at a range of 1.1 million kilometers by the Solid State Imaging system aboard NASA's Galileo spacecraft. Each was taken one hour apart [54].
In these images of continuous pattern there is the presence of a considerably changing in the illumination and for this reason they are used to evaluate the effect of the subroutine "correction_illumination.m" [54].

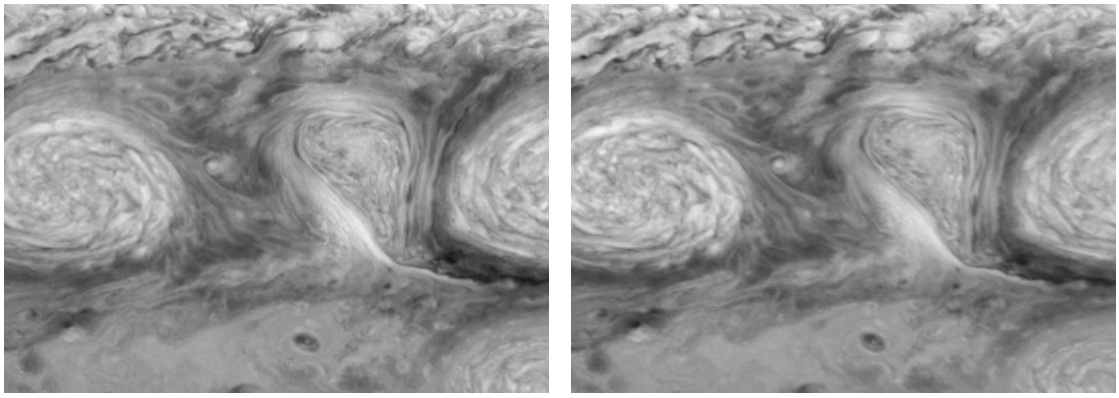

a b

Figure 4.5: A pair of images of the White Ovals on Jupiter, (a) Image 1, and (b) Image 2 [54].

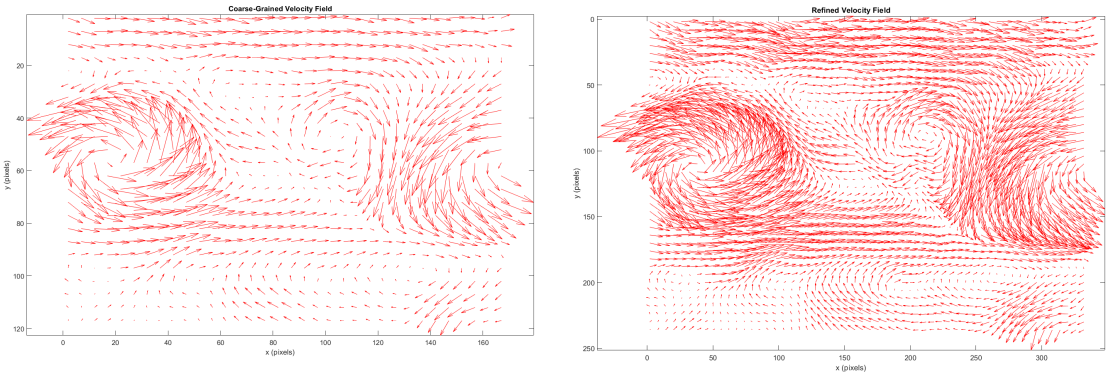

a b

Figure 4.6: Results of Coarse-grained velocity field (a) and Refined velocity field (b) of White Ovals on Jupiter [54].

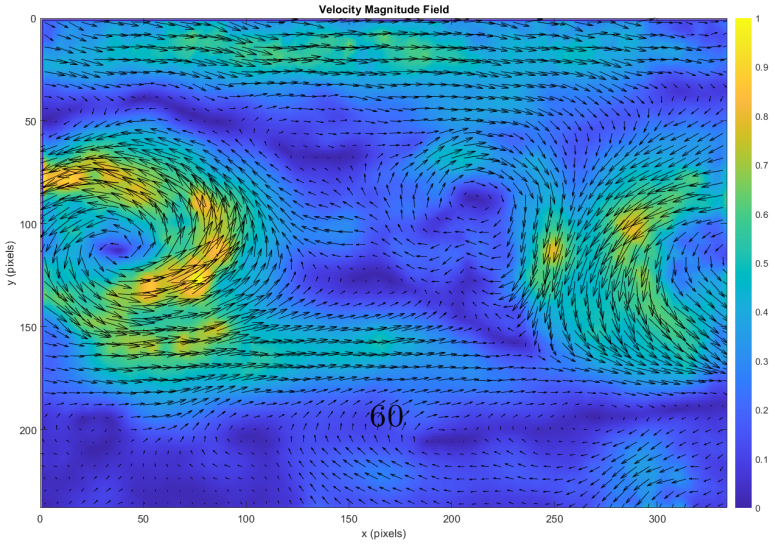

Figure 4.7: Velocity field extracted from the images related to White Ovals on Jupiter [54].

In Figure 4.6 it is shown the difference between the coarse-grained velocity field and the refined velocity field of White Ovals on Jupiter. Observing the results it is possible to notice a better representation of the motion field.
In the following Figure 4.7 are presented velocity field obtained applying the algorithm to the images of Figure 4.5.

Wall-jet region of an impinging jet

The Figure 4.8 shows a jet of air, which hits a wall thus creating a swirling region downstream of the impact zone. Focusing on the wall-jet region there are strong interactions between vortices and boundary layer.
The images shown are PIV image samples with a high particle density. Remembering what mentioned in Section 3.6.5 it is observable how a good density of the image particles can help to keep the error low.
Observing the Figure 4.9 it is possible to seen how the OF method is able to provide the velocity field near the wall with a resolution of one vector per pixel. The OF is able to reveals large vortices generated in the shear layer of the free jet and wall jet due to the instability, and induced secondary vortices (secondary separations) in boundary layer near the wall. Compared to cross-correlation method that is used in PIV, as mentioned in [54], the optical flow allow to obtain the velocity fields with much higher spatial resolution which is one vector per pixel, this show more details of the near-wall flow structures in the thin wall jet.

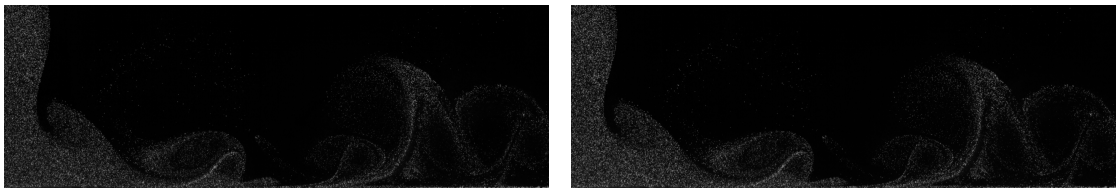

a b

Figure 4.8: Wall-jet region of an impinging jet, (a) Image 1 and (b) Image 2 [54].

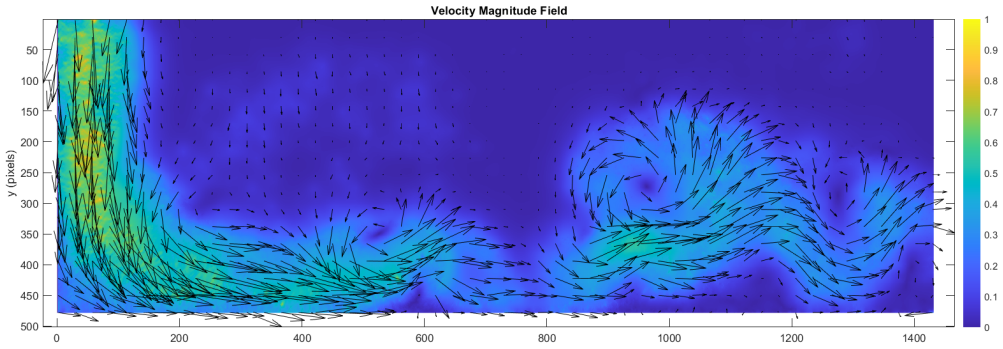

Figure 4.9: Results of Velocity field of Wall-jet region of an impinging jet [54].

4.3 Comparisons between OF and PIV Challenge results

To validate the use of OF in fluid dynamics with the use of particles, a first comparison was made with the fields of motion shown in the third PIV Challenge [56]. In particular, this event took place in 2005 with the aim of describing and comparing the results obtained by the various participants in the competition. Furthermore this event allows to show the various PTV, PIV algorithms in order to discuss and compare their accuracy and robustness.
During the challenge the proposed results are evaluated by a scientific commission, as reported in [56]. In this edition of the PIV Challenge, 5 test-cases were proposed and provided to the participants. Subsequently, the various groups were invited to discuss and present their results in order to highlight in detail the differences and innovations regarding algorithms and methodologies regarding PIV.
The frames provided are time resolved and represent a sequence of synthetic images acquired with a constant frame rate. A laminar separation region is shown in the Figure 4.10. Furthermore, in the image data-set there is a gradual variation of the illumination, in such a way as to simulate different sensitivities of the camera sensor and different particle sizes (3.3.2). For more information on the PIV Challenge reading [57], [58] is recommended.

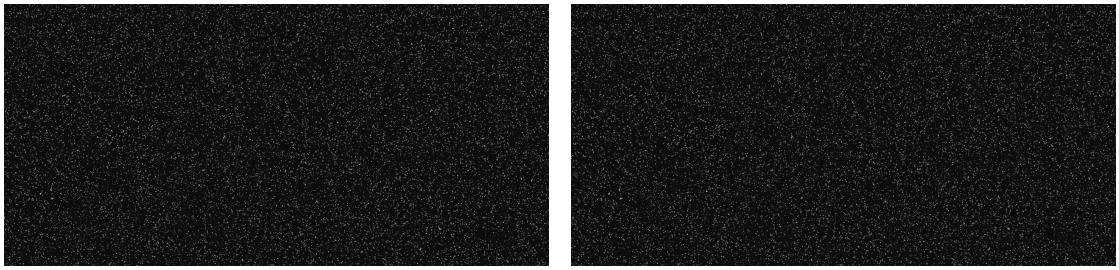

a b

Figure 4.10: Two subsequent frames of case B of Thrid PIV Challenge. Size: 1440x1688 on 8 bits [56].

4.3.1 Comparison of 2-D motion field

In Figure 4.11 it is possible to observe the direct comparison between the results shown in the PIV Challenge and the motion field obtained by analyzing the same frames with the OF algorithm.

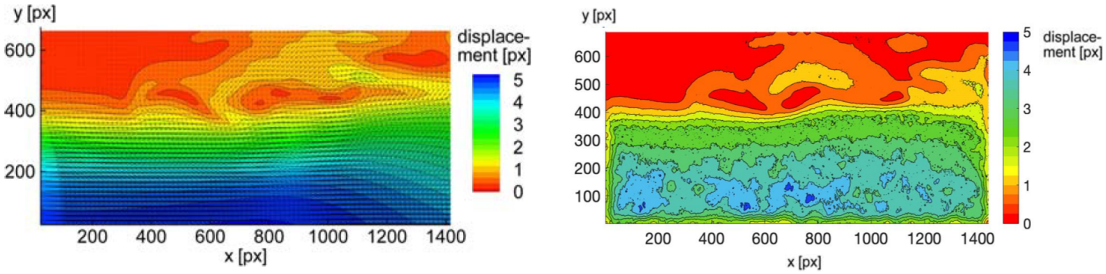

a b

Figure 4.11: Image a: Instantaneous velocity vector field of case B from [56]. Image b: Instantaneous velocity vector field of case B obtained with OF algorithm.

Following the analysis by OF, in order to be able to compare the results in the best possible way, the contour function was applied to create the level curves. In Figure 4.11 b the laminar separation zone is clearly highlighted (about 400 pixels displacement along the y axis). Furthermore, it can be observed that the distribution of velocities in the motion field and the relative intensity is congruent with the motion field represented by Figure 4.11 a.

In the lower region of the image where the velocities reaches the maximum values there are some differences. In areas where low speed gradients are present the differences are minimal showing good performance of the OF. Since the results discussed above show remarkable similarities with those reported by the PIV Challenge, it was decided to carry out other experiments with the use of particles as a tracer.

4.3.2 Final remarks

Observing the results related to the method used to close the general equation of the OF described in [54], it seem to give satisfactory results both with the use of particle images and with continuous images like in Figure 4.5. This last characteristic determined, in part, the choice to investigate this method to observe the results it could give when it is used to observe the motion of a continuous tracer. In the following chapters this method will be validated with respect to its use in the fluid dynamic field with the aim of verifying its usability and its performance.

4.4 PIVlab

The second algorithm used to derive the velocity fields from the frames acquired through the setup described in Chapter 5 is the open source software PIVlab, implemented in Matlab. For further information on all the functions of the algorithm, the reader is referred to [59]. In the following section the main aspects and the main steps performed for the case study addressed in this thesis will be described.
In order to solve the equation 3.12 described in section 3.5 and therefore to be able to calculate the displacement of the particles between consecutive frames, the three main steps present within the PIVlab software have been implemented: Image Pre-processing, Image Analysis, Post -processing.

4.4.1 Image Pre-processing

In order to attenuate the noisy components inside the frames, improve the exposure conditions and the contrast between the background and the particles and attenuate the reflections on the walls it has been chosen to process the images (see section 4.2) before loading them into PIVlab. Subsequently, the various frames to be analyzed were imported into the software and the time resolved analysis was chosen in order to obtain the motion fields between successive frames acquired in a given time interval.

With this algorithm it was possible to load an high number of frames and analyze them simultaneously, this has allowed a significant reduction in computational costs. The Figure 4.12 shows the graphical user interface (GUI) of PIVlab during the loading of the frames in the time-resolved mode.

Figure 4.12: Example of loading frames in PIVlab in the Pre-processing phase.

The first step after loading the data was to apply a mask to all the images in order to isolate the coronary phantom and define a region of interest (ROI) from the analysis, as it is shown in Figure 4.13. Among the different filters present in the algorithm it was chosen to apply the Clahe (Contrast-limited adaptive hinstogram equalization) which allows to locally increase the contrast of the images. In particular, the different frames are divided into small regions, within which the

most frequent intensity values are detected and are redistributed across the entire intensity range of the image (for example from 0 to 255 for 8-bit images). For further information on the Clahe filter, see [60].

Figure 4.13: Example of applying the mask and Clahe filter to frames.

4.4.2 Image Evaluation

In this phase the various parameters for the PIV analysis were set, in particular the type of cross correlation and the size of the interrogation windows (I_w) were chosen. The correlation between the interrogation areas was performed in the frequency domain using the Fast Fourier Transform (FFT) with multiple pass and deforming windows [59].

The use of several interrogation windows with decreasing size allows to obtain a high spatial resolution, without losing the movement of the particles inside the interrogation areas. The larger window allow to more reliably calculate the displacement of the particles, in fact the displacement computed in the first pass is used to offset the I_w in the following passes, i.e., to translate I_w using the displacement vector defined in the previous step. As a result, it is possible to set the size of I_w even if it is smaller than the local mean displacement of the particles [59]. Since this technique returns a single displacement vector for each interrogation

window given by the average of the displacement of the particles inside it, using a very large I_w would lead to obtaining a low spatial resolution.

Figure 4.14: Setting of parameters in the Image Evaluation phase.

To summarize the use of a large I_w allows to increase the signal to noise ratio (SNR) reducing the probability of having wrong correlations, however it also reduces the spatial resolution. For this reason it is necessary to find the right compromise between SNR and spatial resolution. In the case in question, query windows descending 64x64, 32x32, 20x20 pixels with 50% overlap were chosen. The size of the first I_w was chosen about four times the average displacement of the particles [61]. The smaller window size determines the spatial resolution obtained in the analyzes, consequently given that an overlap of 50% has been set, the results obtained will have a resolution of 1 vector for each 10x10 pixels window. In Figure 4.14 it is shown the Image Evaluation phase in which the cross correlation method and the I_w size are chosen.

4.4.3 Post-processing

The velocities calculated by the software immediately after the Image evaluation phase are expressed in $pixels/s$, for this reason, in order to transform the values into cm/s, a calibration procedure was carried out with the software. PIVlab allow

to convert the measurements expressed in *pixels* to *mm* by selecting a reference distance and the time interval between two successive frames. For this reason, the external diameter of the vessels was measured with a caliper and this distance was used for calibration.
The time interval between the frames was calculated starting from the camera acquisition frame rate, as reported in Chapter 5. Following the calibration process, the algorithm allows to calculate and plot numerous parameters, such as velocity, vorticity, streamlines, speed profiles etc. An example of a velocity field plotted with the PIVlab GUI is shown in Figure 4.15. However, to have greater control over the data, it was decided to export the velocity fields directly to Matlab and then proceed with the graphical representation and calculation of other fluid dynamic quantities of interest.

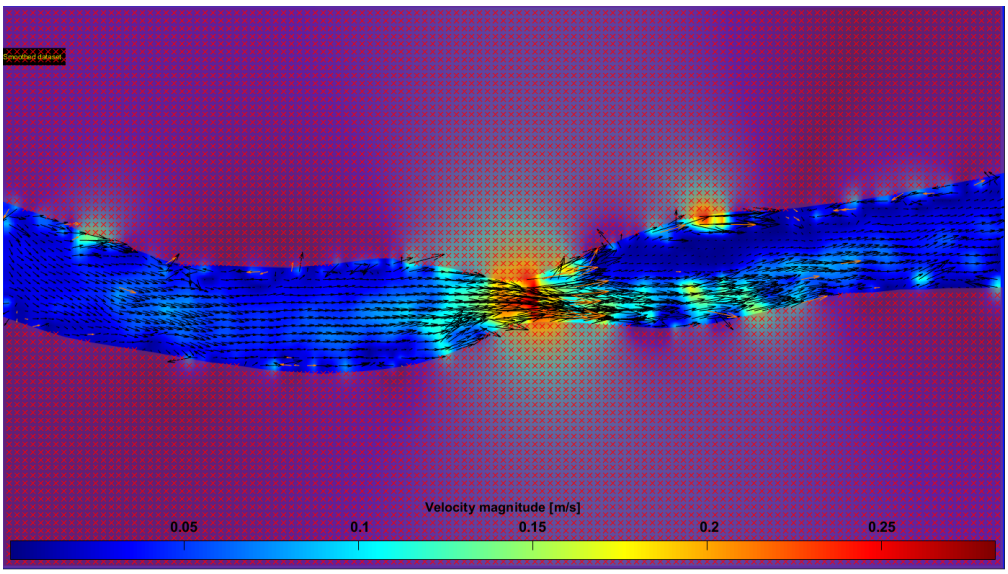

Figure 4.15: Plot of velocity field between two frames with PIVlab GUI.

4.5 Considerations on the two methods and related algorithms

Table 4.3 shows the main characteristics of the two methods in such a way as to show an initial comparison both in terms of the theory underlying the two

approaches (shown in Chapter 3) and in terms of the performance of the algorithms starting from their characteristics described earlier in this Chapter.
From the analytical point of view it is evident that the OF method is made up of equations much more complex than the PIV and moreover it is an open mathematical formulation, which requires the addition of an equation to obtain a solution. The main disadvantage of the PIV technique compared to OF is that it cannot be used with continuous tracers, which are less expensive and easier to find than particles, as fully described in Chapter 3. The PIVlab software also allows to easily adjust its parameters, such as the size of the I_w to adapt it to particular cases, while given the mathematical complexity of the OF it is difficult to modify its parameters to make it compatible with specific applications.
Finally, it can be stated that OF, based on the application of the characteristic equations to the individual pixels of the images, allows to obtain a higher spatial resolution than that obtainable with PIVlab. In fact, in PIVlab the spatial resolution is directly dependent on the size of the I_w chosen, as described above. Following these initial considerations, both algorithms will be applied to the images acquired with the setup described in Chapter 5. The topic of comparison will then be resumed in the Chapter 7 and the main differences found in the results produced by both algorithms will be analyzed.

General aspects	
OF and Open Optical Flow	**PIV and PIVlab**
Used with continuous tracers and particles	Used with particles tracers
Complex equations	Simple equations
Difficult to adapt the parameters	Easy parameter setting
Higher spatial resolution	Resolution linked to I_w size
Few applications in literature	Widely used in literature

Table 4.3: Comparison between the techniques and the resulting algorithms.

Chapter 5

Experimental setup

The following Chapter is divided into two main parts: the first will describe the setup used in the AIM (Artery in Microgravity) project, while the second will present an optimized version of the previous setup, used to acquire the data that have been analyzed in this thesis. Inside the two parts there is a description of the main components of both experimental setups, with the relative hydraulic characteristic curve. In the event that the same component is present in both systems, the description will be given only once. The main difference between the two setups is that the first has been implemented in order to be used with a continuous tracer, while the second has been modified to be adapted for use with a particle tracer.

5.1 AIM setup

The setup shown in the Figure 5.1 was created with the primary objective of reducing the space used, in anticipation of its insertion inside the cube and launch into space (see Section 1.1.1). Each component present in the setup has been chosen in such a way as to obtain the best compromise between component performance and space occupied by it. The core of the experiment consists in the hydraulic loop (Figure 5.1). The loop contains mainly two pumps (one for main circuit and one for dye injection), two reservoirs (one for blood-mimicking fluid and one for dye), and two coronary models. One pump pushes the fluid into the main circuit, which

is composed by two coronary phantoms positioned in series, connection tubes and stopcocks. The blood mimicking fluid firstly passes through the stented phantom and secondly through the stenosed one [1]. Figure 5.1 shows the composition of the setup during the acquisitions carried out on the Earth, with the aim of verifying the functioning and the recording conditions.

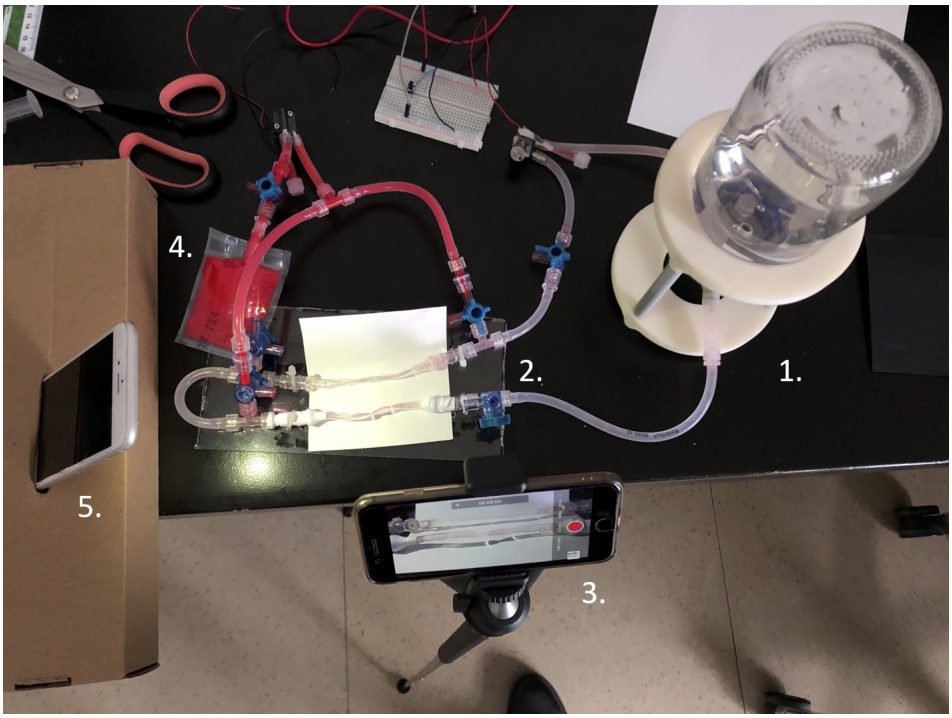

Figure 5.1: Setup used to record videos with the circuit designated for the AIM project. 1 Reservoir with working fluid, 2 3D printed models, 3 Camera (smartphone), 4 Dye reservoir, 5 LED light.

5.1.1 Working fluid

A 33% v/v solution of distilled water and glycerol was used to obtain the ideal fluid to accurately reproduce the rheological behavior of the blood. The choice of this solution as a working fluid is based on a fair compromise between cost, availability of components and similarity of mechanical properties with blood. The viscosity of blood is approximately 4 cP while that of the distilled water and glycerol solution is approximately 2.5 cP at a temperature of 20 degrees. Obviously

this value is inversely proportional to the temperature [62]. The density calculated analytically is equal to 1083 kg/m^3 while that of the blood varies from about 1040 to 1060 kg/m^3 and depends on the hematocrit, which in turn depends on some characteristics of the subject under examination such as age, sex, diet, etc [63].

5.1.2 Dye Reservoir

The dye reservoir was made from a polypropylene (PP) bag in order to obtain a volume of about 50 ml of dye. Inside it was inserted the tracer, consisting of a mixture of distilled water and glycerol at 50% v/v in which about 2.5 ml of red dye was inserted. The choice to use a reservoir of this kind is based on the fact that in this way it does not take up too much space, since it is not completely rigid. In anticipation of the future space launch, the liquid in the reservoir was subjected to vacuum. Figure 5.2 shows the reservoir that was used for the tests carried out and that will be mounted on the cube in view of the space launch.

Figure 5.2: Bag made of PP with the liquid used as a dye inside [1].

5.1.3 Pump

The circuit has two pumps, one that allows the circulation of the fluid mimicking the blood and the other allows the injection of a solution consisting of the same fluid with the addition of the dye. The second pump does not run continuously, as the first does, but it is activated at time intervals. Otherwise, if the second pump were also activated continuously, the dye would be rapidly dispersed within the circuit making it impossible to visualize the motion. Figure 5.3 shows the micro pump RS Pro Centrifugal Pump 480-150 (RS Component, Corby, United Kingdom) which was chosen for the first circuit. For the second circuit, the one concerning the dye injection, the M200-P4 Pump was chosen [1]. For technical information regarding the pumps, the reader is referred to the following reference [64].

Figure 5.3: RS Pro Centrifugal Pump 480-150.

5.1.4 3D Printed Coronary Models

The models representing the vessels were obtained from angiographic images provided by the Politecnico di Torino. One of the phantoms concern a stenotic coronary artery with a degree of stenosis of approximately 69%, while the second vessel represents the geometry of the same vessel after the stent application. For simplicity, from now the stented vessel will be called healthy since it has been used to compare the stenotic case to a geometry that reproduces the case of the same artery in a non-pathological condition.

Before carrying out the molding procedure of the models, the geometry of the same was modified by stretching them at the ends. In this way, the final geometry

of both models is about 8 *cm* long with an internal diameter of about 3 *mm* in the non-stenotic area. The models were produced by Elastrat Sarl (Avenue de Châtelaine, Genève [65]), who reconstructs silicone models starting from their ".stl" format. Elastrat Sarl is a worldwide leader in the development, realization and distribution of human anatomical vascular phantoms. The procedure used for the construction of the models, which is based on a method developed in the early 90s, allows to obtain a faithful reproduction of the internal geometry of the vessels in such a way as to create a realistic environment for simulations. Figure 5.4 shows an image of the final models that were used within the circuit to carry out the experimental tests.
For further information on the model production methodology, which goes beyond the following discussion, the reader is referred to [66]. Table 5.1 summarizes the mechanical characteristics of the material used for the construction of the phantoms.

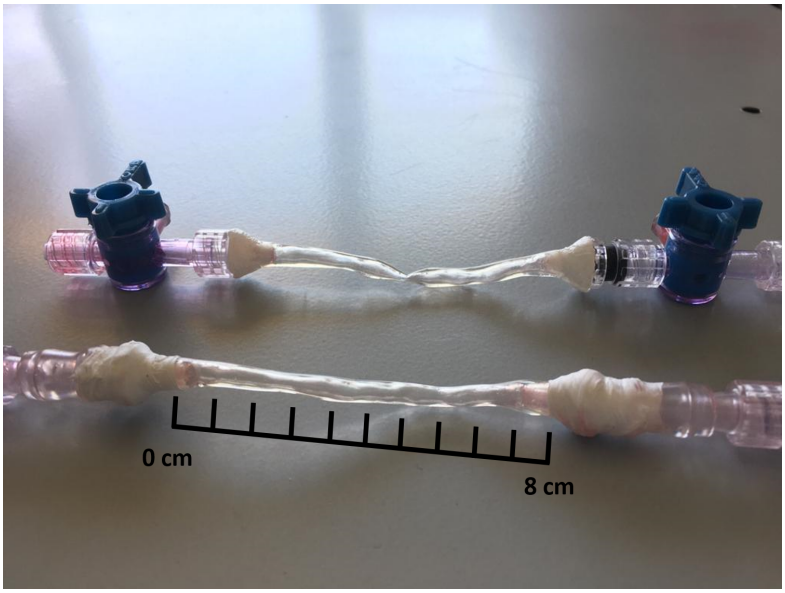

Figure 5.4: Printed phantoms, attached to connectors that allow to plug them into the main circuit.

Silicone physical property	
Hardness	40
Tensile strength	971 psi
Tensile strength	6.7 MPa
Elongation at break	400%
Tear strenght	150 ppi
Tear strenght	27 N/mm
Specific gravity	1.09

Table 5.1: Main mechanical characteristics of the silicone used by Elastrat Sarl for the production of the models [65].

5.1.5 Characteristic pressures of the circuit

The graphs shown in Figure 5.5 represent pressure measurements that have been carried out in order to investigate the range of pressures obtained when the main pump voltage varies. In particular, the pressure values measured in the initial and final zone of the two vessels were acquired through up and down cycles. The graph plotted the differences in pressure measured between the pre-stenotic zone and the post-stenotic zone. The voltage ranges investigated start from 4 V up to 6 Vin steps of 0.5 V. The red curve relates to the stenotic vessel in which the occlusion is present while the blue curve relates to the vessel in the condition following the application of the stent and therefore with the re-established lumen diameter. As expected, the pressure gradient calculated in the stenotic vessel turns out to be greater from the measurements (slope of the curve is greater). As described in Chapter 2, the presence of the restriction causes an increase in speed and a consequent decrease in pressure.
Such a result has been hypothesized considering Bernoulli's law:

$$p_a - p_b + \frac{1}{2}\rho(v_a^2 - v_b^2) + \rho g(h_a - h_b) = 0 \tag{5.1}$$

where p represents the static pressure, ρ the density of the fluid, v the velocity, h and g the height with respect to the reference system and acceleration of gravity

respectively. The differences in these quantities are evaluated between two point of the pipe (a and b). This formula represents the macroscopic energy balance inside a pipe in the absence of dissipative phenomena. The second term represents the energy difference, also referred to as the *kinetic term*, while the third term is due to the difference in altitude and is called the *geodetic term* [67].
Observing the two curves it is possible to note that for ΔP evaluated for higher voltage values there is a greater deviation from the mean. This is due to the fact that the pump, when subjected to its maximum operating conditions (declared by the manufacturer as 6V), is unable to operate continuously but assumes pulsatile operation. This effect is present in both models, although in a minor way for the pressures measured in the healthy one. Obviously, for the healthy coronary the ΔP turns out to be negligible, but there is still an increasing trend as the pump voltage increases. This is due to the internal geometry of the model which, being particularly realistic, has variations in its diameter.

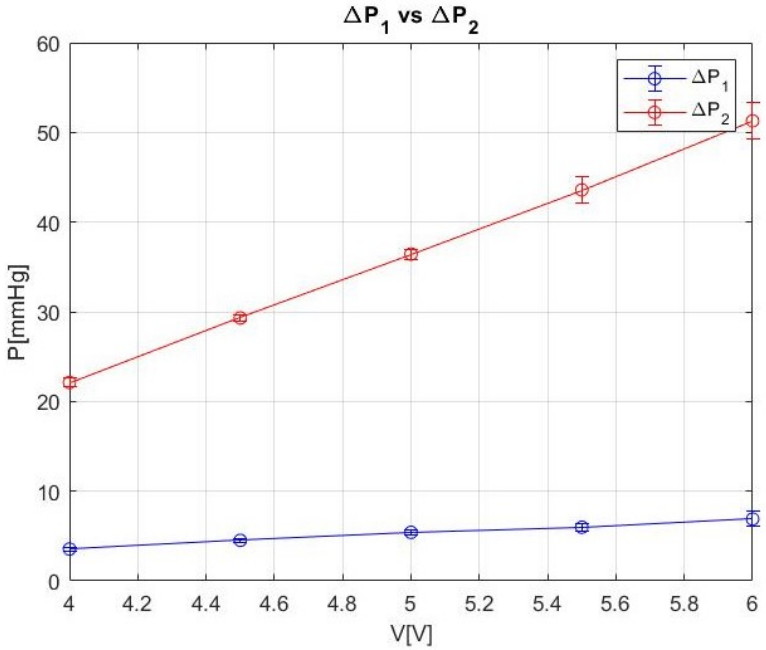

Figure 5.5: Variation of pressure difference upstream and downstream of the pipes as pump voltages varies. Pressure difference for healthy vessel ΔP_1 and for stenotic vessel ΔP_2 .

5.1.6 Pressure Sensors

The pressure measurements, reported in the previous paragraph and described in the following sections, were carried out using the BDC Laboratories pressure sensors (Figure 5.6). The sensors are part of the Data Acquisition System which is one of the parts of the HDT-500 system. With the help of Statys software, it was possible to view the pressure trend during the tests and save them at the end of the tests. For more information and product data sheets, please refer to the following [68].
The sensors that will be used and mounted inside the cube to monitor the pressure trend during the stay of the experiment in space are different. For this purpose, piezoresistive silicon sensors have been chosen. For a more detailed description of the setup and its components inside the cube, which is beyond this work, see [1].

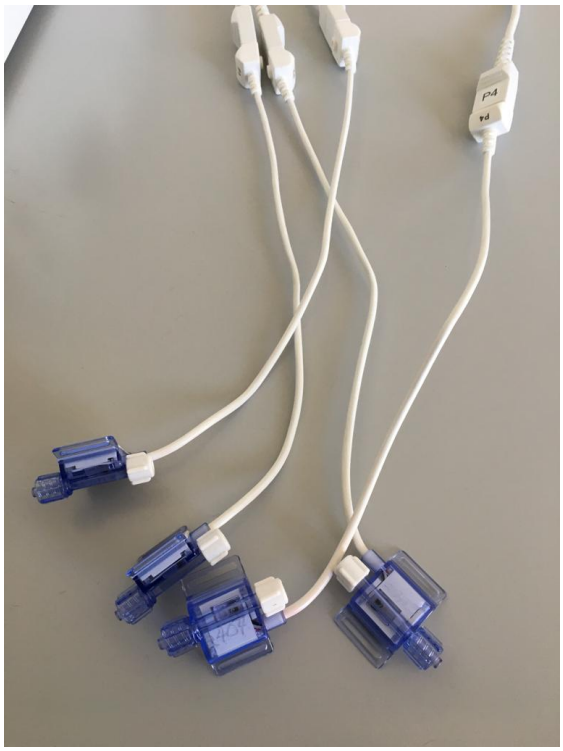

Figure 5.6: Pressure sensors used to calculate the pressure values in the initial and final part of the vessel models.

5.1.7 Characteristic curves of the circuit

Figure 5.7 shows the characteristic curves of the circuit described above. In particular, the obtained curves relate the flow-rate inside the circuit with the pressures measured at the extremity of the vessels. To obtain these curves, pump voltage values were selected in such a way as to obtain flow-rates similar to those present in the coronary arteries. Up and down cycles were repeated. Six pressure values and six flow-rate values were recorded for each selected voltage value in order to obtain more data to interpolate the curves. The *graduated cylinder - chronometer method* was used to measure the flow-rates. Also in this case it is noted that the pressure gradient relative to the stenotic vessel model is considerably greater than in the case of the healthy artery.

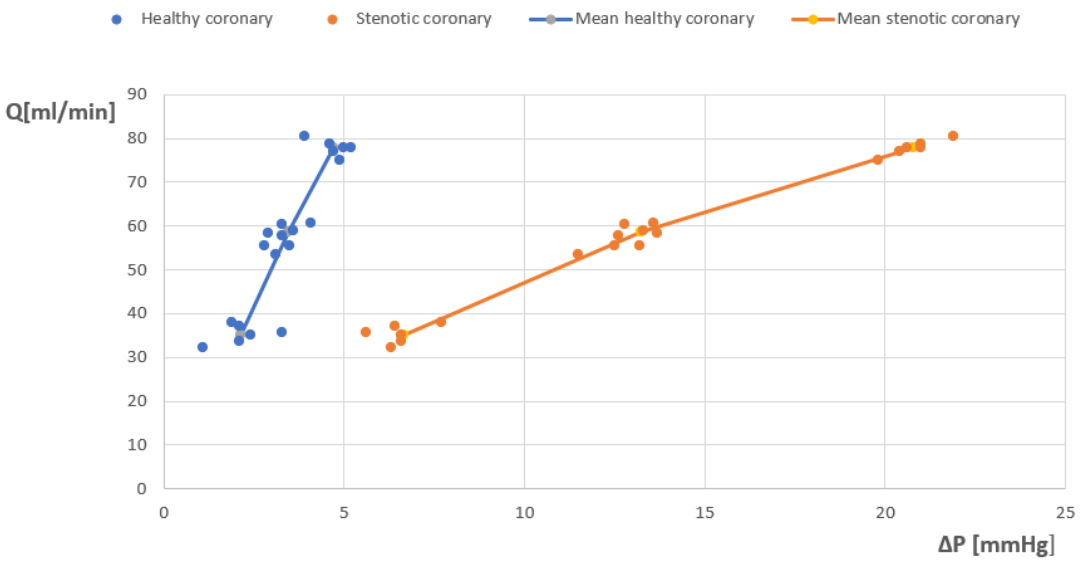

Figure 5.7: Variation of the circuit flow-rate Q as the ΔP varies for the Healthy artery model and for the Stenotic artery model in the AIM setup.

Obviously, comparing these curves with those described in Figure 5.11, different trends are observed. This is due to the different characteristics of the circuit and supports the fact that the curves are specific to the circuit from which they were derived.

5.2 Optimized set-up

In order to try to improve the results, keeping as main objective that of using as little space as possible, it was decided to use particles as a tracer, thus passing from a continuous tracer to a particle one. In Figure 5.8 it is possible to observe the schematic representation of the optimized setup which involves the use of a reservoir with free surface in contact with the air from which the particles have been introduced into the circuit. Another modification that has been made with respect to the condition described above in section 5.1 is the position of the vessel. In fact, in this case, the vessels were analyzed one at a time and were arranged in such a way as to be suspended through the use of two supports, as can be seen in Figure 5.10. The Table 5.2 summarizes the main distance of interest that characterize the geometry of the setup used.

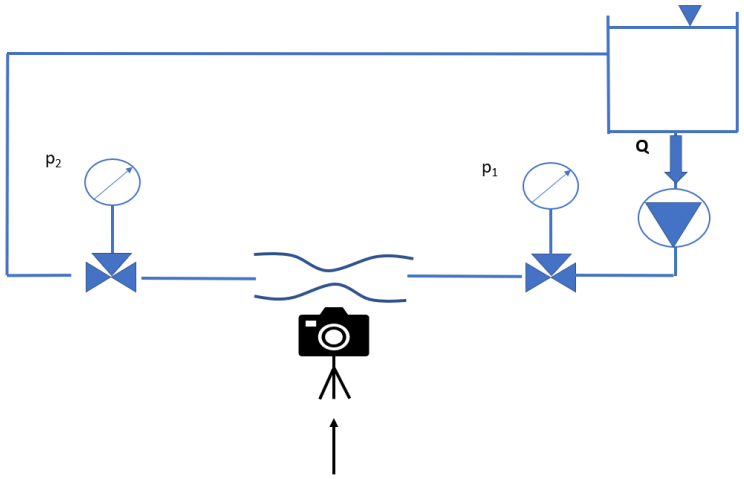

Figure 5.8: Schematic setup for the experiments with the phantom of stenotic vessel.

The Figure 5.9 shows in detail the positioning of the vessel and the other components of the setup. A light was placed under the phantom thus obtaining the appropriate compromise between intensity of light scattered by the particles and reduction of reflections on the vessel walls. In fact, since the phantoms are made up of a curved and complex geometry, reflections have been a significant problem.

Considerable distances in the setup	
Plane-stenosis distance ↑	4 *cm*
Stenosis-camera →	13 *cm*
Plane-free surface distance ↑	15 *cm*
LED-stenosis distance ↑	3 *cm*

Table 5.2: Characteristic distances of the setup.

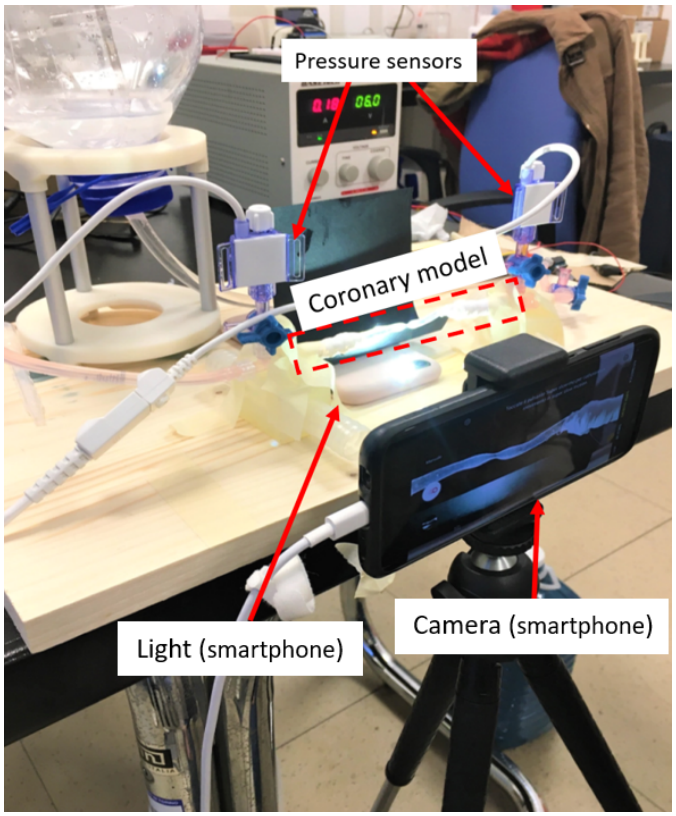

Figure 5.9: Photograph of the experimental setup applied to the stenotic coronary artery model with the various components highlighted.

Getting the right compromise between ideal model lighting and reflection reduction was one of the key points in organizing the setup. The camera was positioned to be orthogonal to the plane on which the vessel lies, this was implemented to improve the quality of the acquisition as explained in section 3.3.2. In Figure 5.10

it is possible to observe the setup created during the recording. In fact, to improve the contrast of the particles and limit the influence of further lights, black sheets have been positioned laterally and behind the vessel.

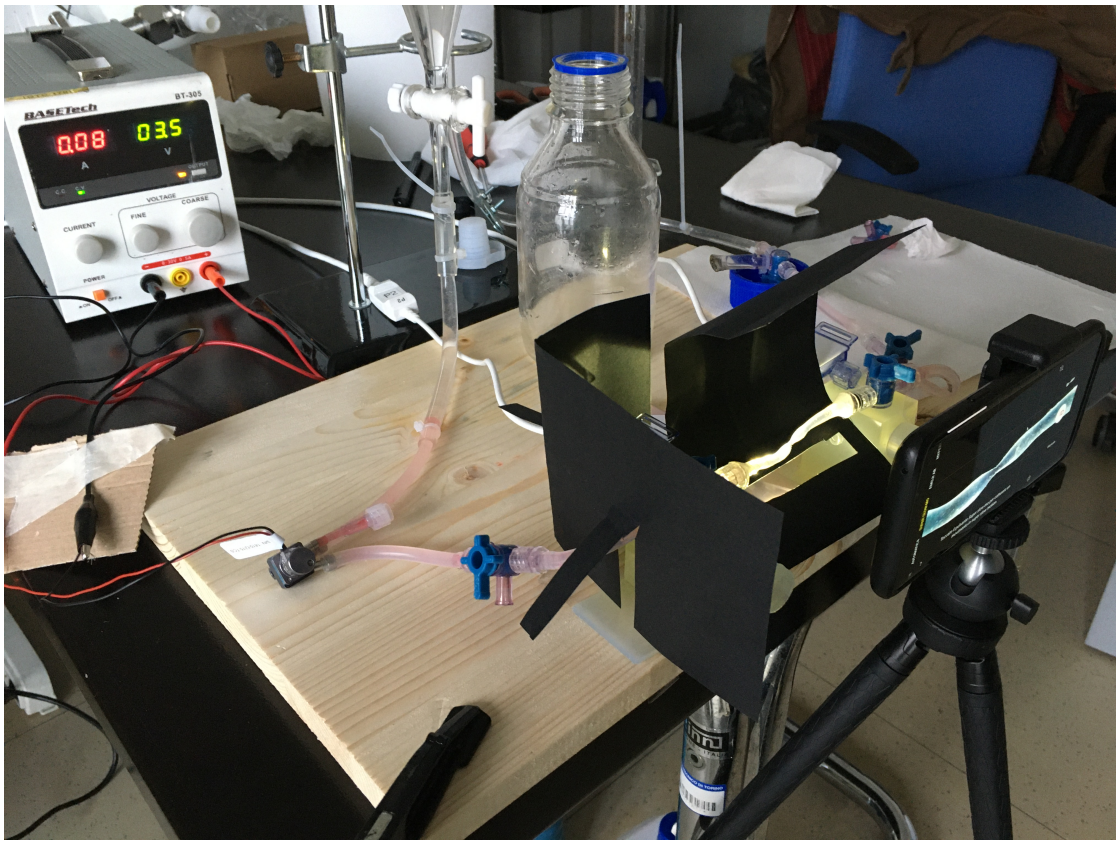

Figure 5.10: Photograph of the experimental setup applied to the stenotic coronary artery phantom.

5.2.1 Characteristic curves of the circuit

The hydraulic characterization of the circuit was carried out with the *graduated cylinder - chronometer method*. Figure 5.11 shows the flow-rate values at varying pressure obtained for both artery models. The characterization was performed with the same setup once for the healthy artery model and once for the pathological one. By varying the pump power in an increasing and then decreasing way, nine tests were carried out for each value. At each test the pressures upstream P_1 and

downstream P_2 of the vessels were measured with the sensors described in 5.1 and subsequently calculated the $\Delta P = P_1 - P_2$. In addition, for each test a determined quantity of fluid was collected inside a graduated cylinder and the time elapsed from the fall of the first drop to reaching the predetermined volume was measured. The values represented were chosen in order to investigate the entire range of flow-rates present inside the LCX. In fact, the flow-rates of 20, 40, 60 and 80 ml/min have been chosen. The first value is obtained in the case of the systolic phase in resting conditions, the second and third are the values in which the average flow rates in the cardiac cycle within the LCX are contained. The last value is obtained during the diastolic phase in conditions of physical activity.

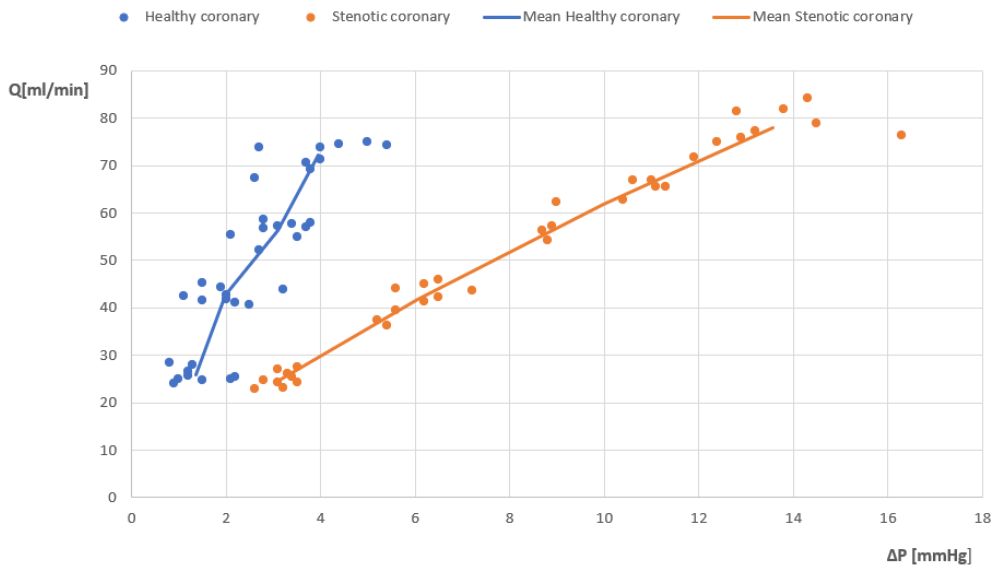

Figure 5.11: Variation of the circuit flow rate Q as the ΔP varies for the healthy artery model and for the stenotic artery model.

5.2.2 Particles

The particles chosen and used in this setup are spherical particles with a diameter of 100 μm in polyamide. In particular, they are produced by LaVision Inc [69]. These particles were chosen for their ability to scatter light, for their density (ρ_p=1100 kg/m^3) similar to that of the working fluid and for their stability in contact with

numerous solutions. The choice of this particle size made it possible to obtain a sufficient intensity of the scattered light despite the light sources used are not those typical of PIV. In fact, in the case of the PIV, lasers are used that have considerably higher powers than those of the light sources described in the Chapter 3. The density comparable to that of the fluid is important to obtain an excellent approximation of the motion of the fluid itself as described in 3.3.2.
The amount of particles inserted inside the working fluid was commensurate with trial and error in order to obtain a fair compromise between quantity of particles and ideal scattering. The particles were mixed with the fluid in such a way as to have a homogeneous distribution within the fluid itself. If the quantity of particles had been too excessive, high values of noise would have been obtained, on the contrary a too negligible quantity would not have allowed to obtain the right visibility. The Figure 5.12 shows the package containing the particles that are shown on the right of the image.

Figure 5.12: Particles used during the experimental tests d = 100 μm, ρ_p =1100 kg/m^3 [69].

For some additional information on the chemical and physical properties of the

particles described, it is recommended to take note of the Table 5.3.

Physical and chemical properties	
Form	Powder
Odour	Odourless
Colour	Varying colours
Melting point	>80 °C
Flammability	Non-flammable
Density	1.1-1.2 g/mL
Water solubility	Insoluble
Decomposition temperature	>300 °C
Ignition temperature	>350 °C

Table 5.3: Physical and chemical properties [69].

5.2.3 Acquisitions

In order to implement a setup with the same structure as a traditional PIV one (described in Section 3.5), the camera was placed orthogonally to the plane in which the analyzed portion of the vessel lies, while the light source was positioned below of the artery model as explained in the previous sections.
Before each acquisition, flow-rate values similar to the physiological values that occur in human coronary arteries were set by regulating the pump voltage. The flow-rate with which the acquisitions were made are respectively 20, 40, 60, 80 ml/min, obtained together with the respective pressure values from the characteristic curve of the circuit described in Section 5.2.1. For each range, 30 videos were recorded with a duration of 0.2 s each and a time interval (Δt) between one frame and the next of 1.04 ms. Subsequently, the extraction of frames and the pre-processing of the images were carried out, which was described in Section 4.2. Furthermore, to avoid introducing motion artifacts during the acquisitions, a voice control mode was used to activate the camera at each video shot.

Camera and Light source

The camera of the Samsung Galaxy S9+ mobile phone was used to record the videos, all the features of the device can be found in [70]. The camera used has a resolution of 12 megapixels and allows to record videos with a frame rate of 960 Hz in HD through the Super slow motion mode. It has been chosen to use the maximum frame rate that can be selected in the camera in order to reduce the displacements of the particles between one frame and the next since both algorithms used to determine the fields of motion have performances that deteriorate as the displacements increase, as reported in Chapter 4. As described in Section 3.5.2 since it was possible to use large particles (100 μm diameter) as tracer it was possible to replace the pulsed light laser typical of PIV setups with a continuous white light. The True Tone LED Flash of the Iphone 8 Plus was used as light source, for the characteristics of the phone see [71].

Chapter 6

Results for Artery in microgravity experiments

This short Chapter shows the initial results obtained in this work with the implementation of the AIM setup described in Section 5.1. It was then briefly discussed how wavefront tracing could be used in the experiments related to the AIM project. Finally, the main reasons that led to the implementation of the new measurement setup with the use of a discrete tracer are reported.

6.1 AIM feasibility experiment

The first experiments conducted in this thesis were performed with the AIM setup, in order to be able to visualize the motion of the fluid in the models inserted in the cube (Section 1.2). As described in Section 5.1 the images were acquired by placing the camera over the phantoms in order to obtain the best focus for both artery models. The frames extracted from the video acquisitions were subsequently pre-processed by applying a black mask to exclude the background from the OF analysis, as it is shown in Figure 6.1.

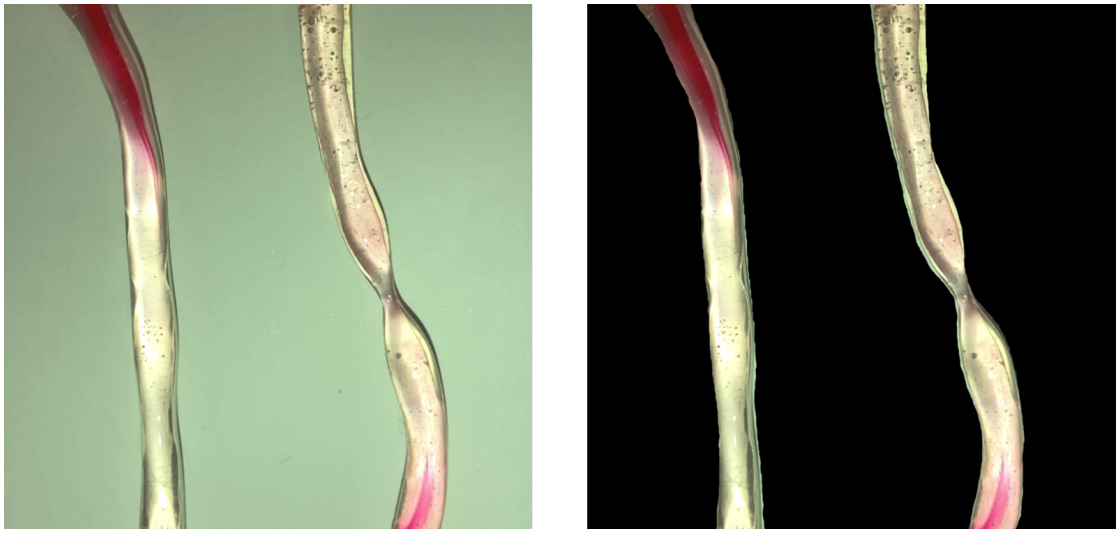

Figure 6.1: One frame acquired with AIM setup. On the left 1 frame. On the right 1 pre-processed frame.

Since the AIM setup was designed for the use with a continuous tracer, the analyzes were carried out using the OF algorithm. In fact, it allows to calculate the velocity field of a fluid inseminated with both continuous and particle tracers, as explained in Chapter 3. Due to the fast diffusion of the dye inside the fluid, it was not possible to obtain 2D velocity fields that faithfully represented the displacement of the fluid between successive frames. The spread of the tracer create the visualization of a continuous medium and does not allow the OF to correctly detect the displacement of the pixels between the frames.
In order to trace the displacement of the fluid in the models it is therefore decided to apply the algorithm to frames representing the wavefront of the tracer, before the complete diffusion in the fluid took place. The results obtained from the analysis of the tracer front are shown in Figures 6.2 and 6.3.
By observing the results it can be seen that by means of the OF it is possible to obtain a tracing of the wave front between various successive frames. From Figure 6.3 it can be seen how in some regions of the motion field the velocity vectors do not correctly follow the direction of the principal motion. Furthermore, very high displacements are obtained between the frames, which can lead to errors on the computation of velocity values (see Section 9).

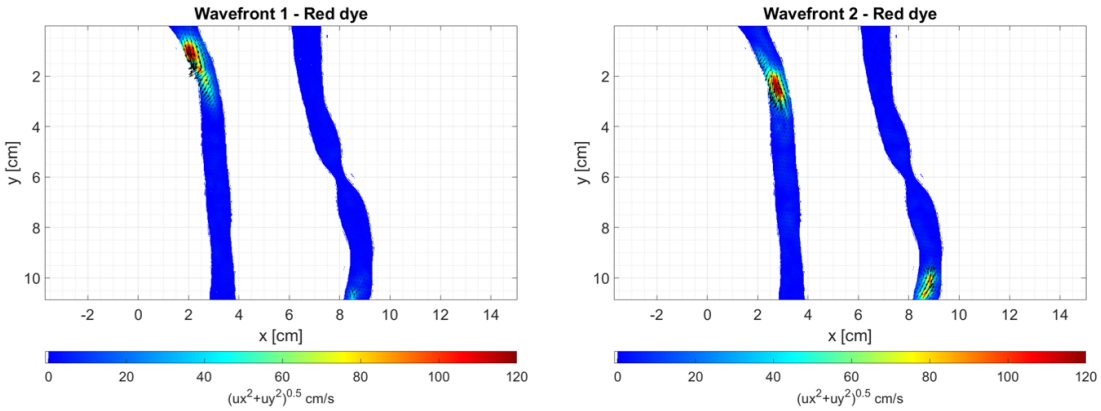

Figure 6.2: Velocity fields of Wavefront of successive frames.

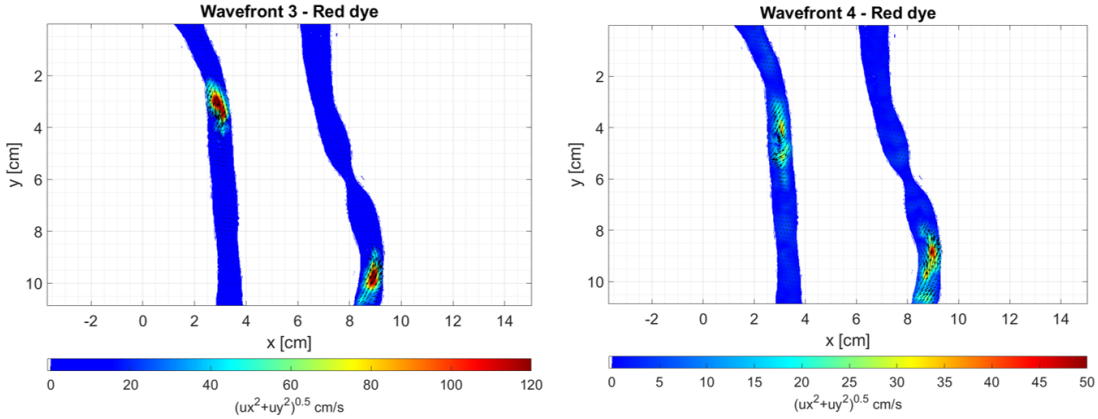

Figure 6.3: Velocity fields of Wavefront of successive frames.

The tracking of the wavefront instant by instant inside the phantoms can be used in experiments in microgravity conditions. As a first information, this method allows to detect whether or not there is movement of the fluid during the experiments in space described in Chapter 1. It is also possible to obtain the characteristic velocity of the fluid and characterize the experiment by calculating the Reynolds number. Thus, by defining the motion regime it will be possible to characterize the other experiments that will be conducted for the AIM project (such as the

measurement of the pH of the fluid) described in Section 1.1.1.
However the display of the wavefront velocity gives limited information on the displacement of the fluid and allows the experiment to be carried out for only a short time, before the tracer diffuses into the fluid. In order to trace the fluid displacement more faithfully and to carry out experiments to visualize fluid dynamic patterns that are generated within the model of healthy and stenotic coronary, the information provided by the analysis of the wavefront was found to be insufficient. For these reasons it was decided to switch to the use of a particle tracer, as described in Chapter 5. The results obtained by using particles as a tracer will be reported in the following Chapter.

Chapter 7

Experimental results

The following Chapter represents the core of this thesis. The experimental results deriving from the implementation of the setup with the use of tracer particles are presented. The various experiments carried out with the relative flow-rates, characteristic velocities and Reynolds numbers are presented. The instantaneous motion fields obtained from the application of both algorithms to two successive frames are then reported. An analysis of the average velocity fields was then carried out, with considerations on the effect of the mean on the results. In the description of the velocity fields, the results obtained by both algorithms are compared. In the final sections some quantities calculated starting from the 2D average velocity fields are shown, in order to understand if the method presented in this thesis allows to visualize and study the fluid dynamic patterns that are established in a pathological artery.

7.1 Experimental approach

Following the characterization of the circuit in Section 5.2.1, different working flow-rates were chosen, respectively 20 ml/min (case A), 40 ml/min (case B), 60 ml/min (case C), 80 ml/min (case D). These values were chosen in accordance with [9] and following what explained in Section 2.3.1 in order to obtain physiological flow-rates during the cardiac cycle for the coronary LCX. Some of the results

obtained with the different flow-rates will be reported and discussed below. The quantities obtained from the experiments will be analyzed from a physical point of view, in order to understand whether fluid dynamic patterns are present in the motion fields that can lead to the formation of cardiovascular pathologies (i.e. atherosclerosis, see Chapter 2).
A comparison will also be presented between the results obtained with the OF algorithm and the same results obtained with PIV. In particular, the ability of both techniques to detect the motion of particles in the pipe will be discussed and the spatial resolutions of both algorithms will also be compared.
Considering the mean diameter of coronary artery models equal to 3 mm, it is possible to calculate the average velocity using the principle of conservation of the mass inside a pipe given by the following relationship:

$$Q = Av = k \tag{7.1}$$

where Q represents the flow rate of the pipe, A the area of the pipe section and v the velocity inside it.
Using the formula (7.1), the average velocity values within the healthy coronary phantom were calculated for the various flow-rate cases, as observed in the Table 7.1. For the values reported in the third column of the table, the average internal diameter of the pipe (3 mm) was used. Considering the density and viscosity of the working fluid, reported in Section 5.1.1, using the formula (2.2) the theoretical Reynolds number in the pipe was calculated.

$\boldsymbol{Case}$	$\boldsymbol{Q[ml/min]}$	$\boldsymbol{V_m[cm/s]}$	$\boldsymbol{Re_m}$
A	20	4.72	61.34
B	40	9.43	122.55
C	60	14.15	183.89
D	80	18.86	245.10

Table 7.1: Theoretical speed values and Reynolds numbers as the flow-rate values vary for the healthy coronary model. V_m is the mean theoretical velocity in the pipe, Re_m is the Reynolds number in the pipe.

As regards the stenotic artery model, the objective was to use the same flow-rate values as those imposed in the healthy case. However, during the experiments it was not possible to maintain constant flow-rates due to setup errors discussed in Section 9.1.1 and for this reason the flow-rate values for the stenotic model are different from those imposed in the healthy phantom.
Table 7.2 shows the flow-rate values for the stenotic model calculated starting from the experimental velocities for the various cases (A, B, C, D). The mean velocities and Reynolds numbers outside the stenosis were calculated using the same pipe diameter and fluid density and viscosity used for the healthy case. To calculate the mean velocity value and Reynolds number in the stenosis, an average restriction diameter of 1 mm was considered.
Considering what has been explained in Section 2.2, taking into consideration the Reynolds numbers reported in Tables 7.1 and 7.2 it can be stated that from a theoretical point of view the experiments were carried out under conditions of laminar motion.

$\boldsymbol{Case}$	$\boldsymbol{Q[ml/min]}$	$\boldsymbol{V_m[cm/s]}$	$\boldsymbol{Re_m}$	$\boldsymbol{V_s[cm/s]}$	$\boldsymbol{Re_s}$
A	12	2.82	36.65	25.46	110.29
B	15	3.53	45.87	31.83	137.88
C	25	5.89	76.55	53.05	229.81
D	35	8.25	107.21	74.27	321.73

Table 7.2: Theoretical speed values and Reynolds numbers as the flow-rate values vary for the stenotic coronary model. V_m is the theoretical velocity outside the stenosis, V_s is the theoretical velocity in the stenosis, Re_m is the Reynolds number outside the stenosis, Re_s is the number of Reynolds in the stenosis.

7.2 Instantaneous velocity fields

All the instantaneous velocity fields, for all the flow-rate shown above, were obtained by analyzing two successive frames extracted from the related video. Instantaneous velocity fields can be useful for visualizing particular conditions along a cycle. In this case, for the constancy of the work cycle, they were used to have a first estimate of the quality of the results and served as a basis for implementing subsequent improvements.

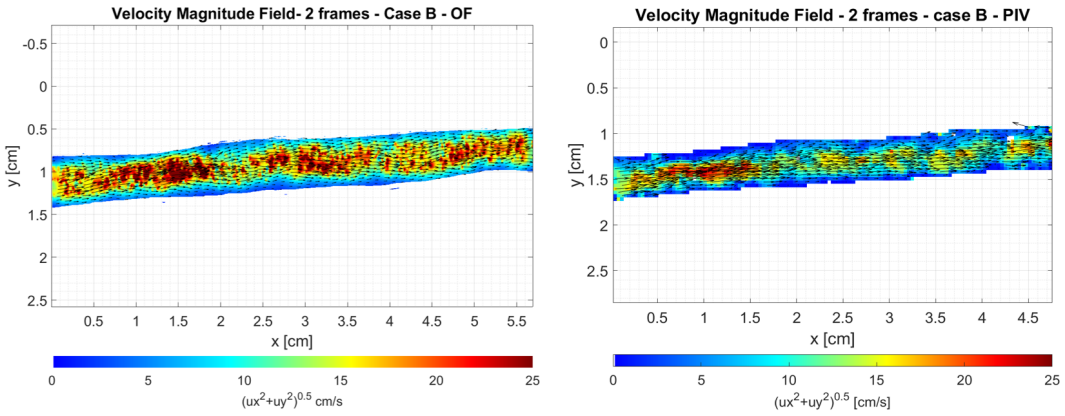

Figure 7.1: Instantaneous velocity field of healthy coronary artery. Case B. First image: OF. Second image: PIV.

From the preliminary results obtained for the healthy coronary artery it is possible to observe a velocity trend that does not correctly approximate the theory of the motion of a fluid in a cylindrical pipe under conditions of laminar motion [67]. However, both algorithms, especially in cases with low flow-rates (Figure 7.1), are able to detect higher speeds in the center of the pipe and lower speeds approaching the wall. Observing the figures of the results in the stenotic model (Figures 7.3 and 7.4) it can be seen that both algorithms return a velocity trend that has maximum values in the restriction zone, in accordance with the conservation mass law (equation (7.1)). Considering the highest flow-rate value (Case D), downstream of the stenosis, the separation between a low velocity region in the upper area of the vessel and a high velocity jet in the underlying area can be observed.

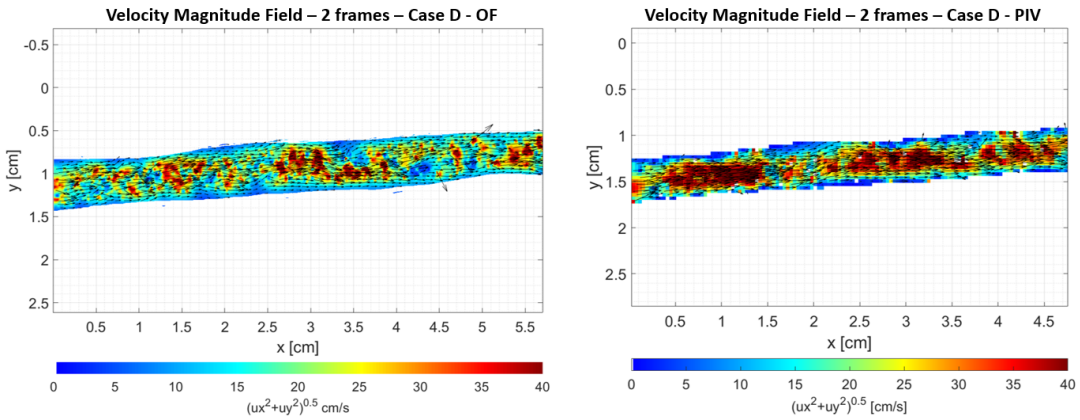

Figure 7.2: Instantaneous velocity field of healthy coronary artery. Case D. First image: OF. Second image: PIV.

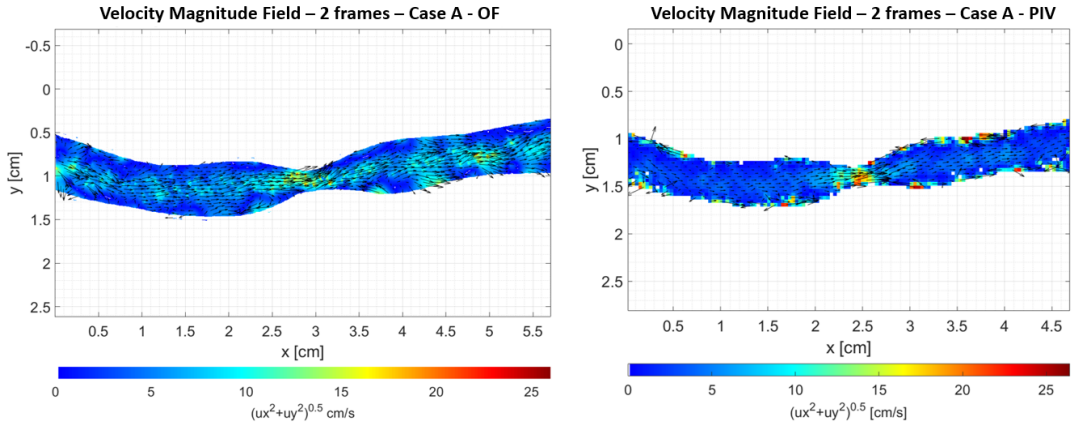

Figure 7.3: Instantaneous velocity field of stenotic coronary artery. Case A. First image: OF. Second image: PIV.

As for the velocity values, in the case of the healthy artery, the average of the velocities calculated by the algorithms is in agreement with the theoretical data shown in Table 7.1. By analyzing the results of the stenotic model, on the other hand, both algorithms underestimate the speed in the restriction zone with respect to the theoretical values.

From a qualitative point of view, as for the instantaneous velocity fields, the results obtained are significantly affected by noise. In particular, as can be seen in Figure

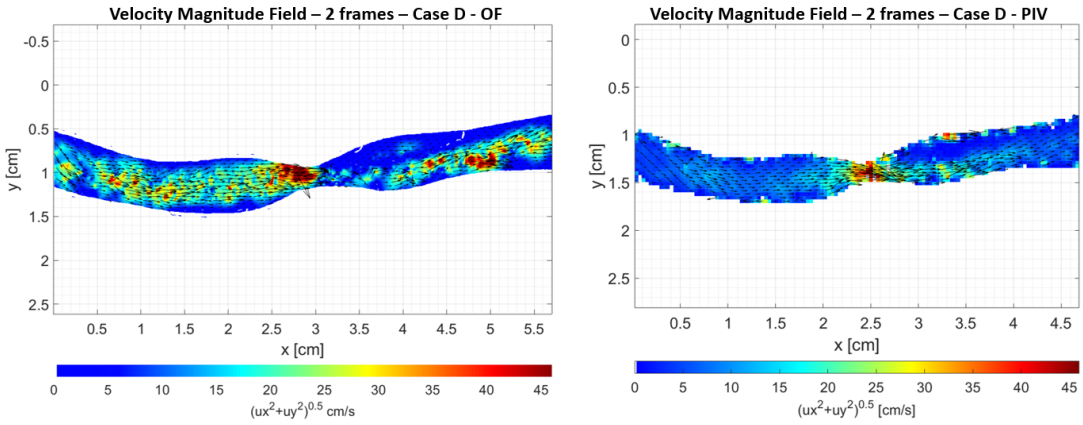

Figure 7.4: Instantaneous velocity field of stenotic coronary artery. Case D. First image: OF. Second image: PIV.

7.5, the presence of a trend of the velocity vectors that does not follow the principal motion of the fluid is shown. In order to attenuate the velocity components that cause noise in the results and to highlight certain fluid dynamic patterns of interest, some algebraic operations were performed such as averaging discussed in the next Section (7.3).

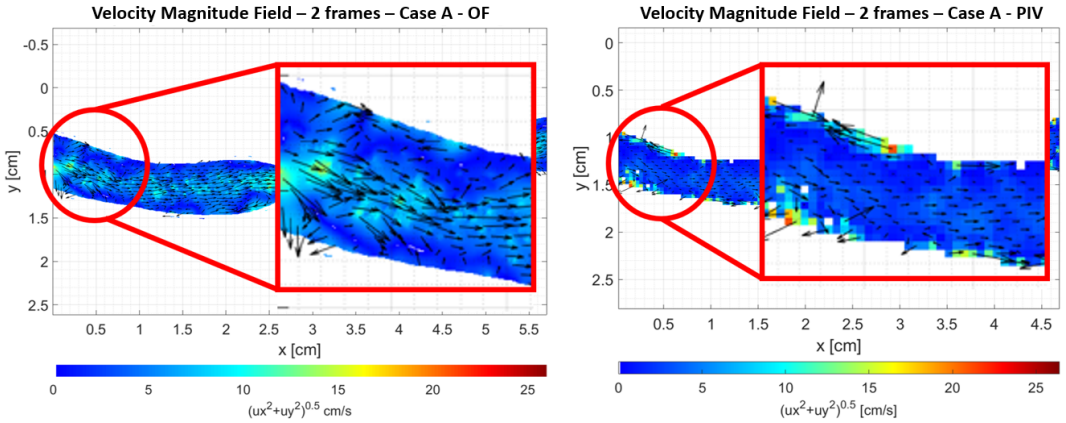

Figure 7.5: Zoom of velocity field in two areas where the presence of noisy vectors is detected. First image PIV. Second image OF.

7.3 Average of the velocity fields

As in the previous case, the average of the velocity fields were also analyzed for each flow-rate value. In particular, as shown in Section 7.3.2, averages were carried out on several motion fields and the variation of the result was evaluated as the number of averaged fields (n) varied. As will be explained later, it was decided to take as a reference the average over 280 velocity fields to obtain a fair compromise between the signal-to-noise ratio and the computational costs of the algorithms. The elapsed time between two frames remained constant and only the number of velocity fields used to calculate the average was varied.
As shown in [72], averaging the velocity fields allows to improve the SNR and to obtain velocity fields with fewer spurious vectors. The calculation of the average over a large number of fields is widely used in the case of PIV, but as shown in this paragraph it has allowed to obtain less noise-afflicted results also in the case of OF.

7.3.1 Description of results

The following Section shows some results obtained for both algorithms, after having averaged over 280 velocity fields. Observing the reported results, it is possible to notice how the presence of outliers decreases as the number of average frames increases. As described in [73], the average on the velocity fields allows to improve the results, in particular, in the situation in which there is a low density of particles in the fluid. By carrying out the average, it is possible to increase the number of particles that are on average present within the analyzed spot, in the case of the PIV this is equal to the interrogation window. On the contrary, excessive averaging can cause an over-presence of particles inside the spot.
Considering the Figure 7.6 and 7.7 which show a direct comparison between the motion field obtained between 2 frames and that obtained by averaging, it is possible to see a notable improvement in the quality of results. In this case, in the healthy artery a velocity distribution is obtained with a much more gradual variation between the extremities and the center of the vessel, compared to the instantaneous velocity field. This trend more closely reflects the velocity trend

that should be expected from the fluid under these conditions, as explained in the previous section.

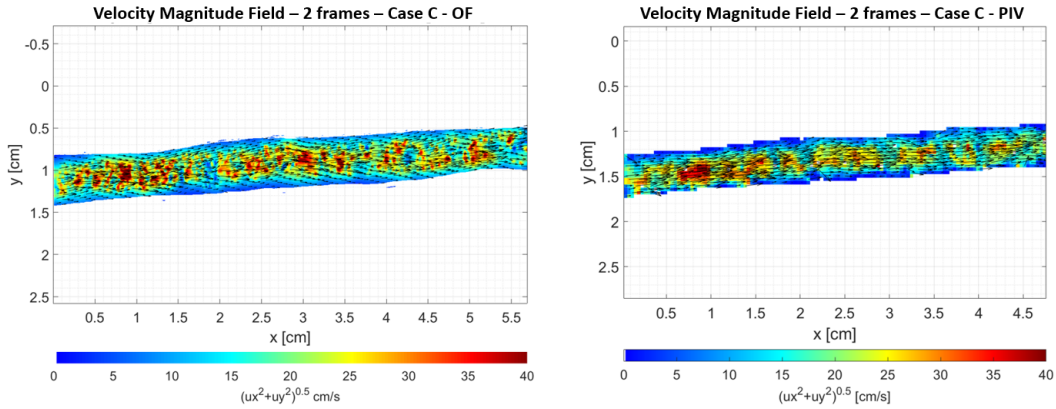

Figure 7.6: Instantaneous velocity field of healthy coronary artery. Case C. First image: OF. Second image: PIV.

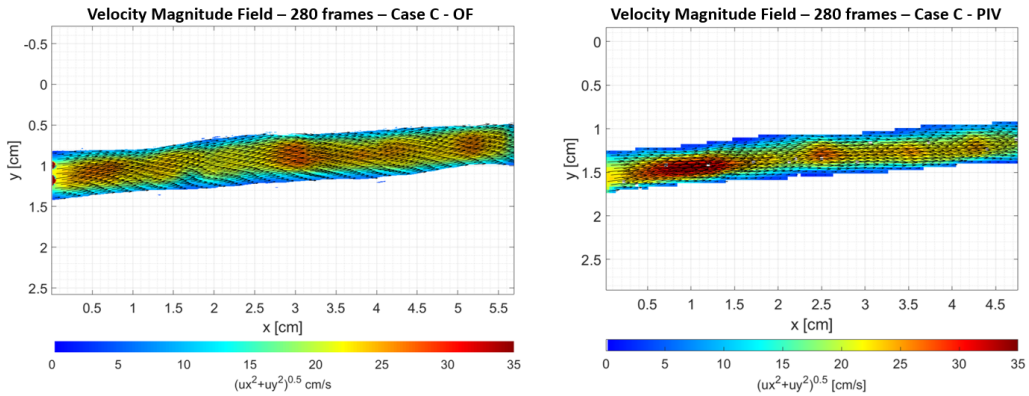

Figure 7.7: Average of the velocity field of healthy coronary artery between 280 frames. Case C. First image: OF. Second image: PIV.

As regards the quantitative data, apart from sudden accelerations of the fluid in some areas, due to variations in diameter and the irregular geometry of the vessel, the values obtained in Figure 7.7 are approximately in agreement with the theoretical data calculated in the Table 7.1.

Figure 7.8 and 7.9 show the results relating to the mean over 280 velocity fields in the stenotic artery for two different flow-rates. A notable improvement can

be observed in the trend of the velocity vectors, which follow the main direction of motion more accurately than the instantaneous velocity fields. The maximum speed values are well highlighted in the region of the restriction in agreement with (7.1). Outside the stenosis, the velocity values follow the theoretical trends both for the Case A (Figure 7.8) and for the Case D (Figure 7.9).

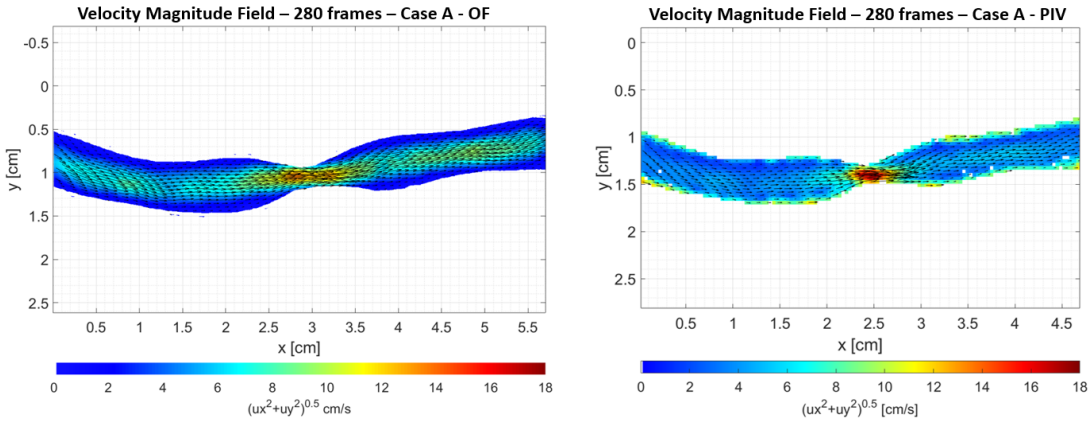

Figure 7.8: Average of the velocity field of stenotic coronary artery between 280 frames. Case A. First image: OF. Second image PIV.

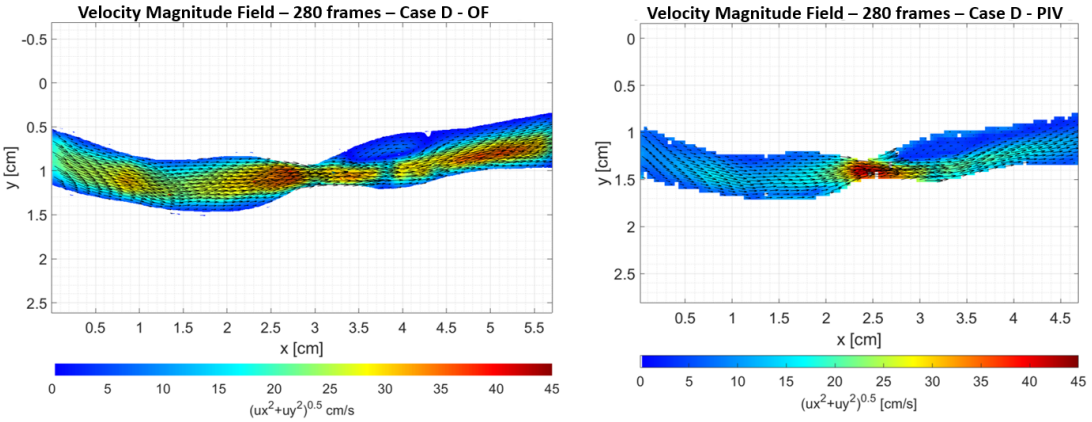

Figure 7.9: Average of the velocity field of stenotic coronary artery between 280 frames. Case D. First image: OF. Second image PIV.

As regards the velocities calculated by both algorithms in the presence of the abrupt shrinkage, they differ from the theoretical calculations, as will be discussed

later in Chapter 9.
Related to what is expressed in Section 2.5.1, it is important to study the fluid dynamic structures that are generated inside an artery in order to be able to predict and understand the causes that lead to the development and progression of atherosclerotic pathologies. Analyzing the results of the experiments conducted in vitro, it can be seen how, following the averaging operations on multiple fields of motion, it is possible to obtain a good visualization of the fluid dynamic patterns that are generated downstream of the stenosis.
In Figure 7.9 it is possible to observe, in the area immediately downstream of the restriction, the separation of the flow with the formation of a low speed recirculating area in the upper region of the vessel and a high speed jet in the underlying region. By comparing the Case A and D, the formation of a recirculating zone with greater extension and visibility is obtained in the case with a greater flow-rate, as will be shown in the following sections. Moreover it is possible to make a qualitative comparison between the velocity field related to case D and the results present in the literature shown in Section 2.5.1. It can be noted the separation of the jet downstream of the stenosis with the formation of a low speed recirculating zone both for case D, for the experimental and numerical results reported in the literature (Figure 2.9.

7.3.2 Consideration on the average

In order to numerically verify the effect of the mean of the motion fields as n increases, a $3x3$ windows for OF and a point for PIV, were randomly chosen in the domain. For the PIV images, a point was selected in the restriction area and in the recirculating zone downstream of the stenisis. For the OF image 3x3 windows were chosen at the same points choosen for PIV as shown in Figure 7.10. Subsequently, the value assumed by the average was observed as the number of motion fields used for the average increased. In particular, for the PIV results, the variation of the speed in the selected points was observed, while for the OF the variation of the velocity obtained as the average of the values present in the $3x3$ window was observed. In Figures 7.12, 7.11 the blue curves represents the trend of the average

as n increases. In particular, the value of n was increased in steps of 10 in order to investigate the mean values between 10 and 560 motion fields. In the graphs, the point highlighted in red represents the average value for 280 fields, while the dashed line represents the speed value in the points considered averaged over 560 fields.

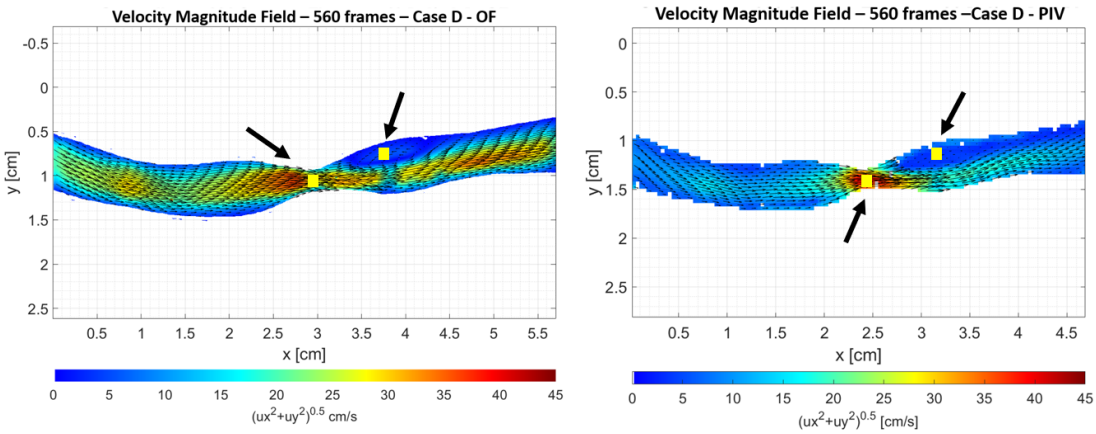

Figure 7.10: Points chosen to evaluate the effect of averaging the velocity fields on increasing the number of averaged frames. In the image on the left the two points chosen for the results of the OF, one in the stenosis region and one downstream. In the image on the right the two points chosen for the results of PIV, one in the stenosis region and one downstream.

On the basis of the results shown in Figures 7.12 and 7.11, it was decided to use the average over 280 motion fields for the calculation of all the results that are shown in this thesis. In all the graphs this value turns out to be the adequate compromise between a correct approximation to the mean over several motion fields and the computational costs necessary to process the data.

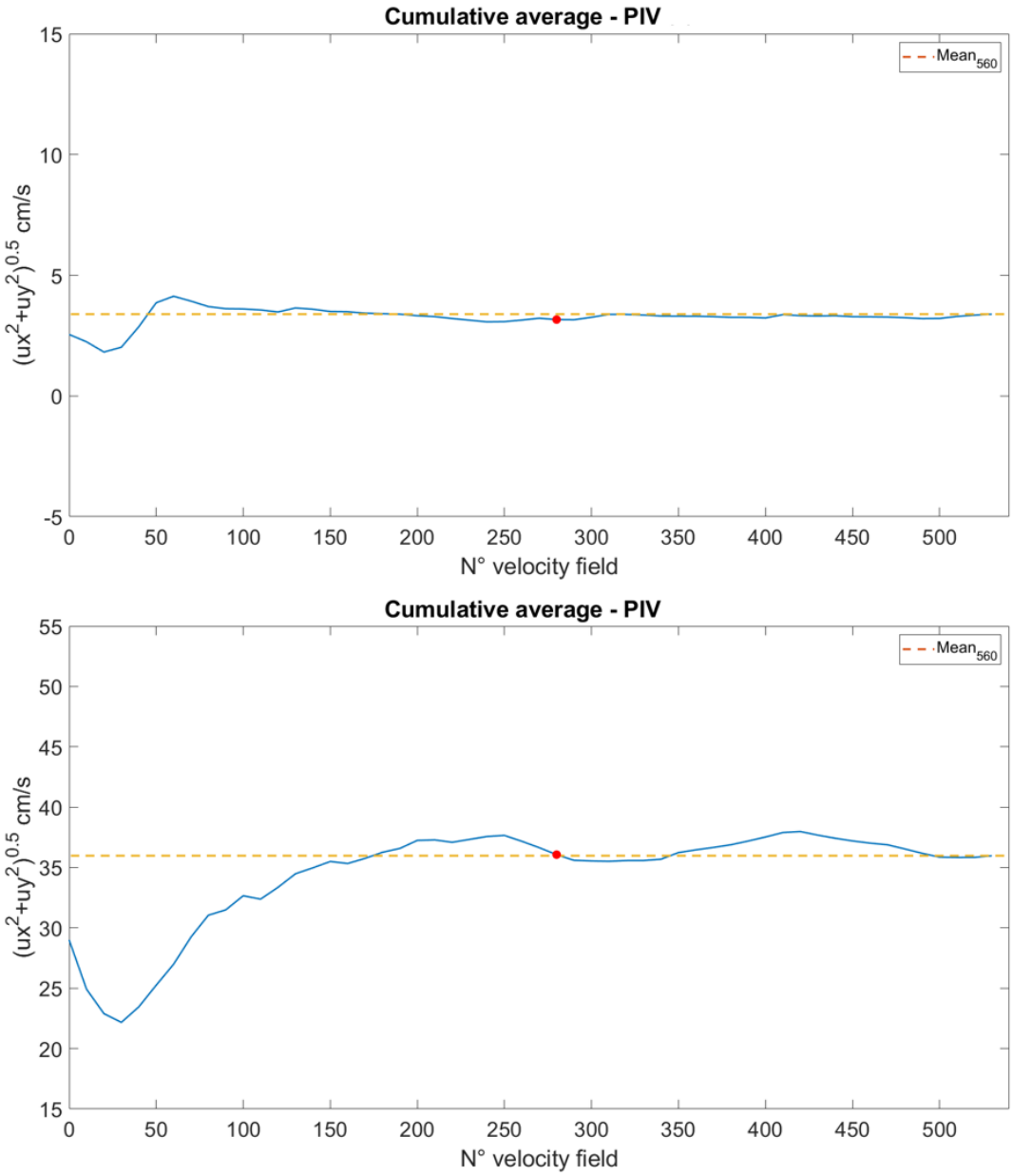

Figure 7.11: Effect of the average (PIV): Top image = trend of the speed values, in a point chosen in the recirculating zone, as the number of fields used to carry out the average increases. Bottom image = trend of the speed values, at a point chosen in the restriction, as the number of fields used to make the average increases.

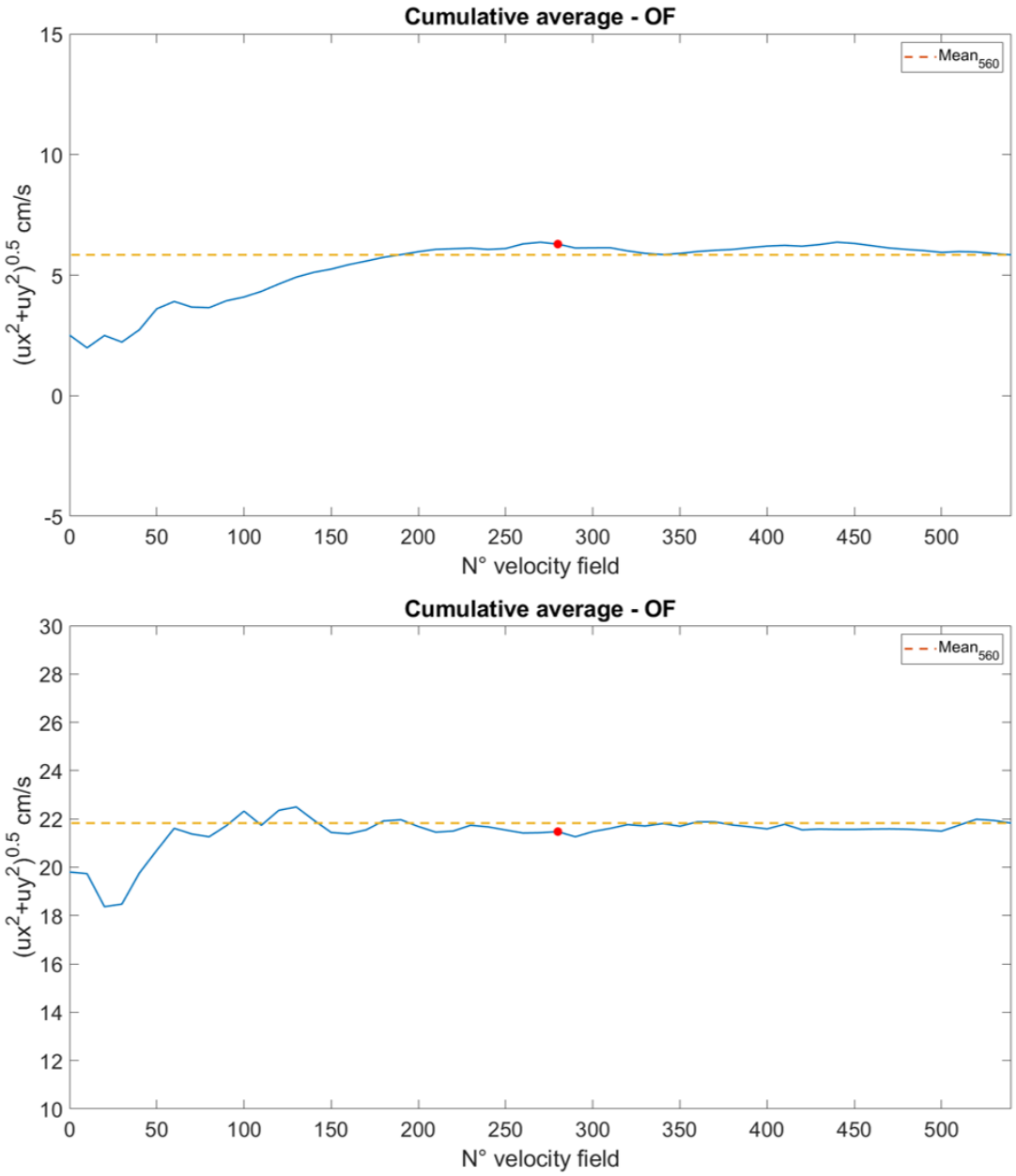

Figure 7.12: Effect of the average on OF: Top image = trend of the speed values, in a 3x3 window chosen in the recirculating zone, as the number of fields used to carry out the average increases. Bottom image = trend of the speed values, in a 3x3 window chosen in the restriction, as the number of fields used to make the average increases.

7.3.3 Comparison of methods

As regards the instantaneous velocity fields, by observing Figure 7.1, it can be seen how the OF algorithm provides a motion field with a non-physical trend, in fact the transition between the low wall speed and the speed in the center of the vessel is too abrupt. PIV instead, shows a more gradual speed variation between the wall and the central axis of the vessel which is quite in agreement with the theory of the motion of a fluid in a cylindrical pipe.
Considering the stenotic model it is possible to observe how the OF algorithm allows to obtain a greater spatial resolution (1 velocity vector per pixel) than PIV. On the other hand, the lower spatial resolution that occurs with the PIV causes a worse visualization of the velocity field. As can be seen in Figures 7.3 and 7.4, the analyzes with the PIV algorithm show areas in the motion field (single white pixels in the images) in which no velocity values are present. This is due to the lack of a sufficient number of particles in some areas of the vessel. Furthermore, in the results of PIV concerning the stenotic model, speed peaks are observed near the vessel wall due to variations in brightness at the edges, as will be further explored in the section 9. Observing the results related to the average of velocity fields for both techniques, it can be seen that as n increases the pattern of the velocity vectors inside the vessels assumes a more regular trend. Indeed, no abrupt changes in direction are observed between two adjacent vectors as described in 7.2. From the Figure (7.7) it can be seen that the general trend of the velocity in the field of motion is comparable for both algorithms. However, PIV, by averaging on more fields of motion, allows to further reduce the presence of outliers compared to OF. In fact, in the field of motion shown in Figure 7.7 in the case of the OF outliers were detected with velocities approximately 3 times the maximum velocity value in the colormap.
From the results of the model with stenosis it is possible to note how the greater spatial resolution of the OF allows a better visualization of the fluid dynamic patterns of interest, such as the recirculating zone and the separation of the jet. In Figure 7.8 high velocity values at the wall detected by PIVlab are observable. These errors are mainly due to reflections present on the wall that have not been

sufficiently attenuated by the pre-processing of the images.
From an initial analysis of the results relating to the instantaneous and average fields, it can be deduced that the PIV technique allows to obtain velocity values that are more in agreement with the theoretical values and is less subject to the presence of outliers in the motion field. The OF instead, despite showing the presence of outliers, by applying the solution equations to the single pixel allows to obtain a better visualization of the fluid dynamic patterns of interest. It is necessary to remember that the computational costs associated with the OF are far higher than those of the PIV, as will be discussed in section 10.1. Other results calculated from the average velocity fields will be shown below and for sake of brevity the results obtained with only one of the two techniques will be shown.

7.3.4 Streamlines

The following paragraph shows the streamlines superimposed on the colorimetric map of the velocities for all cases related to the stenotic artery (Figures 7.14 and 7.15) and two cases related to the healthy artery (Figure 7.13).

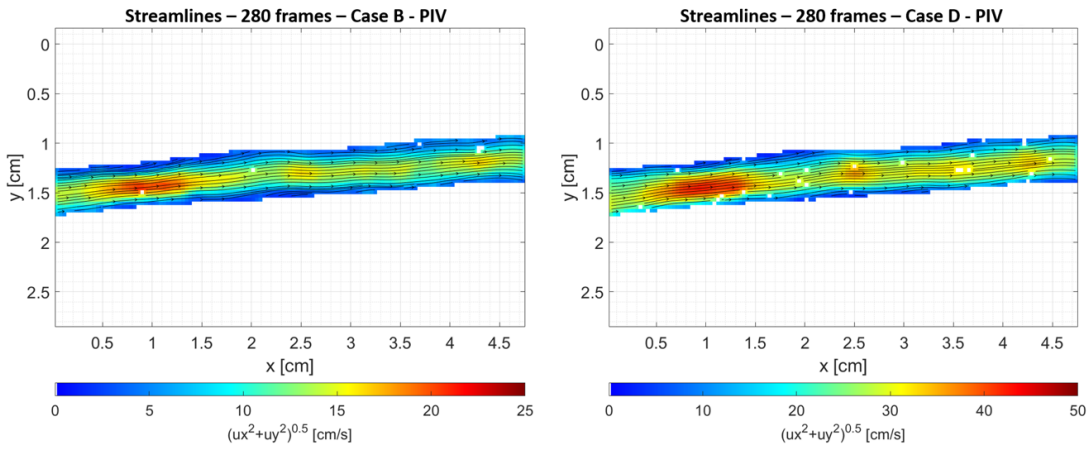

Figure 7.13: Streamlines relative to average velocity field in healthy coronary artery. Image on the left: Case B. Image on the right: Case D. PIV results.

Specifically, streamlines are lines that are at each point tangent to the local velocity vector [74]. The concept of streamline given the definition is obviously an

Eulerian concept, since they are calculated starting from the spatial distribution of velocities. Streamlines provide information on the direction in which the fluid element is traveling at each point in time. Following the definition just stated, different streamlines at the same instant in a flow cannot intersect, since fluid elements cannot have two different speeds at the same point [67]. From Figure 7.13 the streamlines allow to highlight the condition of laminar motion (see Section 2.2). This condition is in accordance with what is reported in Section 7.1 since in the range of flow-rates for which the experiments were carried out the state of motion is always laminar.

As regards the stenotic artery model, it can be noted that for cases A and B shown in Figure 7.14 there is no visible recirculating zone downstream of the stenosis with the inversion of the fluid motion. Only at higher flow-rates, starting from case C (flow-rate 25 ml/min) and also for case D (flow-rate 35 ml/min), a clear separation of the jet downstream of the stenosis can be observed with the formation of a low speed recirculating area, in the upper region of the vessel, and stagnation point. From the experimental results it was possible to calculate the extension of the recirculating zone in terms of length and area. Furthermore, considering the velocity vectors with negative sign in the motion fields, it was possible to calculate the percentage of retrograde flow. In particular, it was calculated how many velocity vectors reverse the direction of motion in the 2D velocity maps.

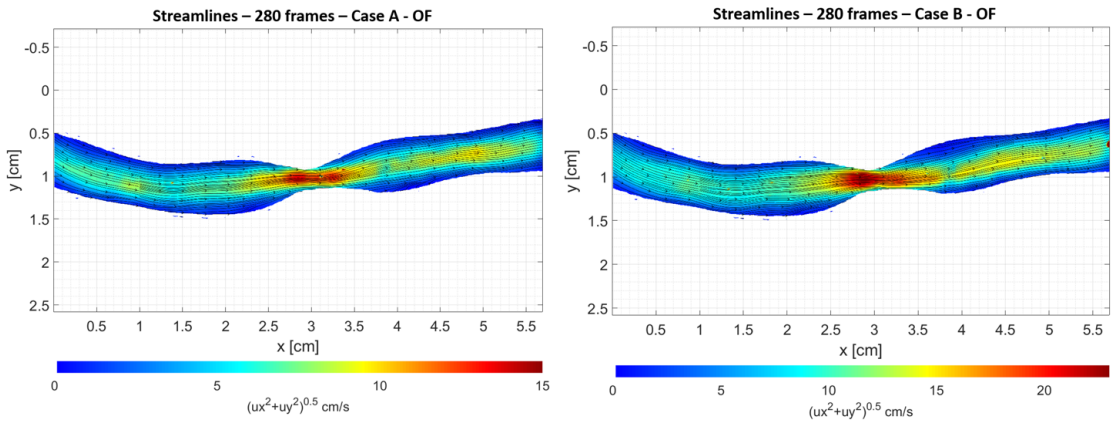

Figure 7.14: Streamlines relative to average velocity field in stenotic coronary artery. Image on the left: Case A. Image on the right: Case B. OF results.

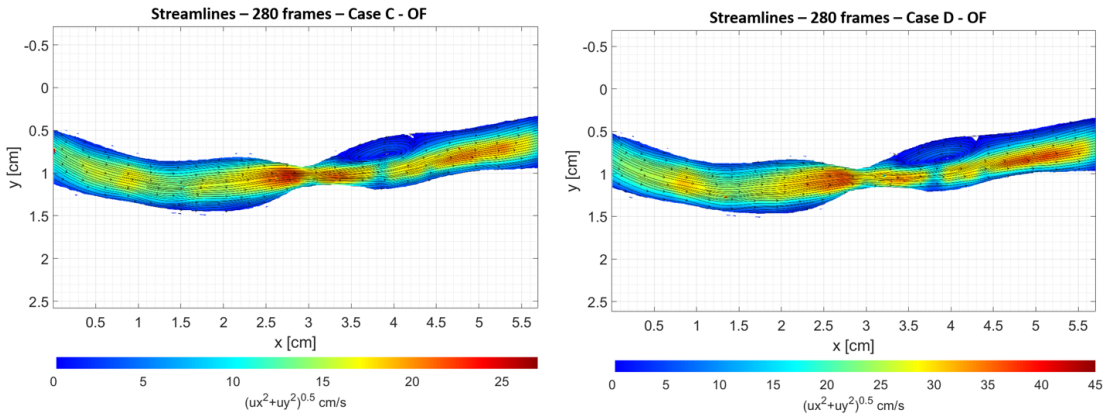

Figure 7.15: Streamlines relative to average velocity field in stenotic coronary artery. Image on the left: Case C. Image on the right: Case D. OF results.

The data reported in Tables 7.3 and 7.4 show the results obtained for OF and PIV respectively. From a physiological point of view, as explained above, it is important to study the characteristics of the low-speed recirculating zones that can form downstream of a stenosis because they are closely linked to biological pathways that lead to atherosclerosis and thrombosis [22]. From the data shown in the Tables 7.3 and 7.4 it can be seen that as the flow-rate increases, the three calculated quantities increase. The estimates calculated with the PIV showed values of length and area of the recirculating zone lower than the estimates of the OF. It should be remembered that these calculations are directly influenced by the spatial resolution of the methods used. The OF having a resolution of 1 velocity vector per pixel allows to have a more accurate estimate of the calculated quantities. In the next Chapter a comparison between these quantities and the same ones obtained from numerical simulations will be shown.

Cases	***Length*[*mm*]**	***Area*[mm^2]**	***Rf*%**
Case C	4.91	14.39	4.78
Case D	6.01	18.22	5.99

Table 7.3: Values of length, area of recirculating zone and % of retrograde flow (Rf) for OF results. Cases C and D.

$Q[ml/min]$	$Length[mm]$	$Area[mm^2]$	$Rf\%$
Case C	3.25	8.46	4.01
Case D	4.17	12.64	5.95

Table 7.4: Values of length, area of recirculating zone and % of retrograde flow (Rf) for PIV results. Cases C and D.

7.4 Velocity profiles

In the following paragraph the various velocity profiles of U component (alog x axis) extracted from the average velocity fields are shown. The data were extracted from the PIV analyzes and some sections of interest were chosen in the pipe. Figure 7.16 shows the arbitrary section chosen for the healthy vessel and the three sections chosen for the stenotic one. In particular, it was decided to display the trend of the velocity profiles normalized for the maximum velocity value as the flow-rates vary. For the stenotic case, in addition to the pre-stenosis section, it was decided to visualize the velocity profile also in the stenosis and downstream of the stenosis, where the flow separation can be observed. From Figure 7.17 it is noticed how the trend of the velocity for the healthy vessel and before the stenosis assumes a parabolic profile, with the maximum peak near the central axis of the vessel. This trend reflects an approximation of the Poiseuille motion for a fluid moving in a cylindrical pipe [6].

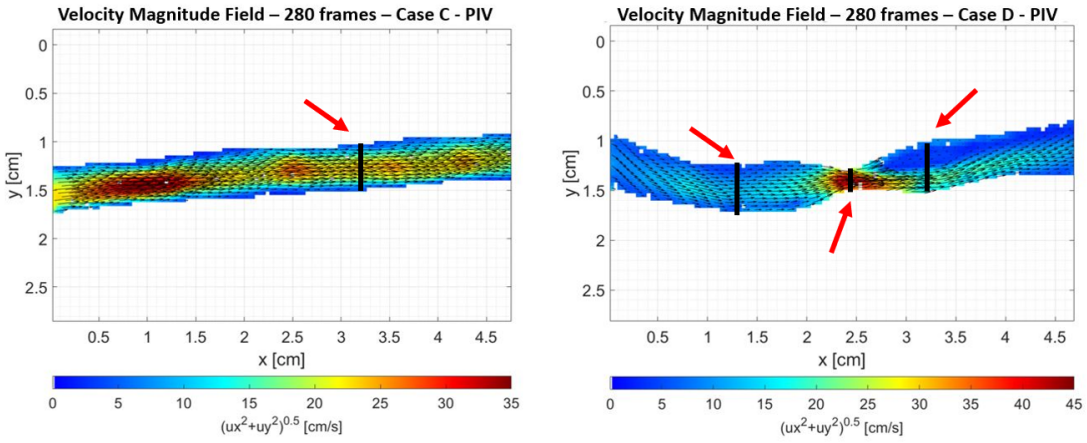

Figure 7.16: Sections chosen to extract velocity profiles. Left image: arbitrary section chosen for the healthy vessel. Right image: sections chosen for the stenotic vessel, respectively pre-stenosis, in stenosis and post stenosis.

Furthermore, it can be noted that the velocity profile in the pre-stenosis case assumes a more irregular parabolic shape than in the healthy case and this may be due to the irregularities of the geometry of the pathological vessel. Always considering the pre-stenosis profiles for Case A, an increase in velocity is observed near the lower wall of the vessel, due to light reflection phenomena at the edges.
For both graphs presented in Figure 7.17 it can be noted the increase in the peaks of the parabolas as the flow-rate increases and this is in agreement with the equation (7.1).
Figure 7.18 shows the velocity profiles for the section in the stenosis and for the section downstream of the stenosis. For the first graph, an approximately parabolic trend is observed with the speed increasing as the flow-rate increases, as seen in the previous cases. It can be observed that at the walls, in correspondence with the stenosis, zero velocity is not obtained in the experimental case, unlike what will be seen in the numerical results, described in the next Chapter. The high velocity values near the wall are due to the low spatial resolution of the velocity field and also to reflection phenomena near the edges.
As for the graph representing the profiles extracted from the downstream section of the stenosis, the trends are in line with what is described by the mean velocity

fields and streamlines discussed in the previous paragraphs.

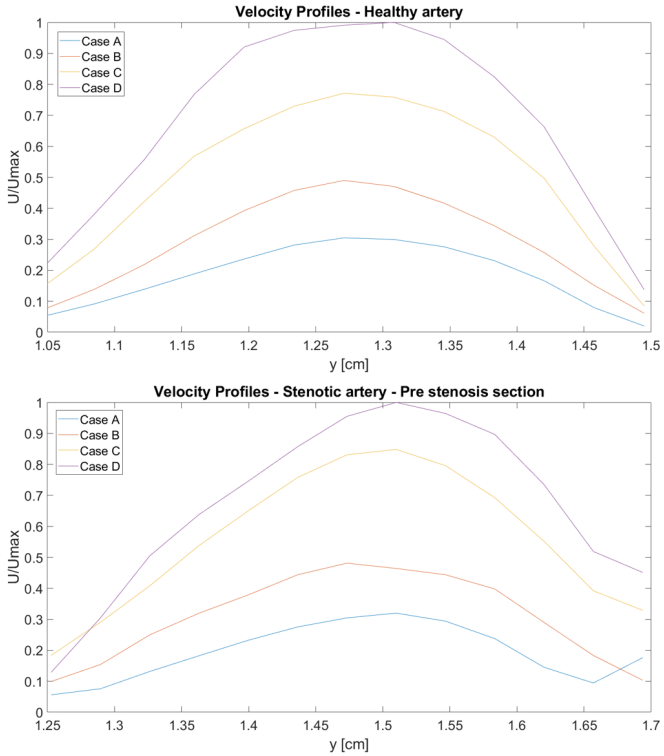

Figure 7.17: U component (x axis) velocity profiles normalized for the maximum value for all cases. Top image: U component velocity profile for the healthy coronary model. Bottom image: U component velocity profile for the stenotic coronary model in pre-stenosis section.

In the left part of the graph it is possible to see a reduction in the speed values due to the formation of the recirculating zone. It can be observed that the inversion of the motion occurs only for the highest values of flow-rates (cases C and D), while for the other cases there are no negative values of the U component of the speed. These considerations confirm the fact that the method proposed in this work allows to visualize the recirculating zone only starting from the flow-rate value and Reynolds numbers corresponding to case C. The right part of the graph (moving towards the positive y) shows the region inferior of the vessel in which the lateralized jet is present. In this case the maximum peaks, in addition to growing, are increasingly lateralized as the flow-rate increases.

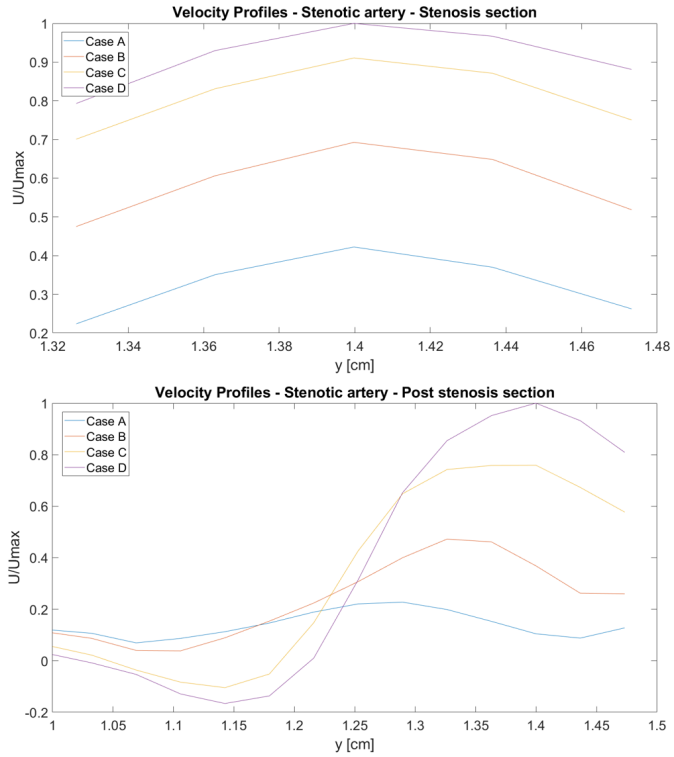

Figure 7.18: U component (x axis) velocity profiles normalized for the maximum value for all cases. Top image: U component velocity profile for the stenotic coronary model in the stenosis section. Bottom image: U component velocity profile for the stenotic coronary model in post-stenosis section.

It can be concluded that the extracted velocity profiles are in line with what occurs in the motion fields and allow a better visualization of the velocity trend, especially in the recirculating area and in the flow separation region.

7.5 Shear rate

Starting from the average velocity fields obtained experimentally with OF technique, it is calculated the shear rate, this is the gradient of the velocity component along the x axis (U) with respect to a variation along the vessel diameter coordinate (y axis in the graphs). The shear rate gives information on the velocity transmitted by the fluid threads as the y coordinate varies.
Figure 7.19 shows the shear rate colormap calculated for the lowest flow-rate values

(cases A and B) where in the velocity field the inversion of the motion downstream of the stenosis does not occur.

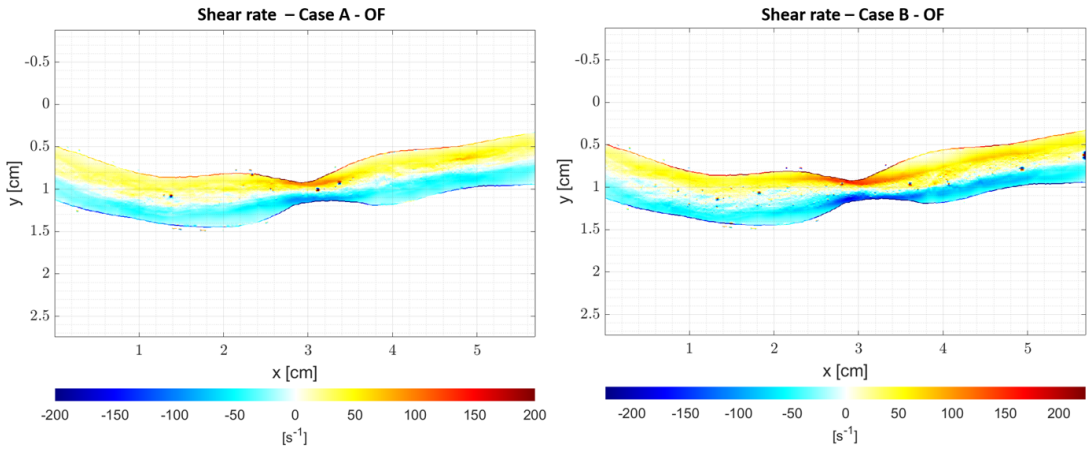

Figure 7.19: Shear rate colormap of stenotic coronary artery. Image on the left: Case A. Image on the right: Case B.

On the other hand, it can be observed that in cases C and D (Figure 7.20) the low speed recirculating region obtained in the average velocity fields is associated with low shear rate values near the wall. Observing the results shown in Figure 7.20 only from a qualitative point of view, it is possible to note that the highest shear rate values are obtained in the jet separation zone, downstream of the stenosis.

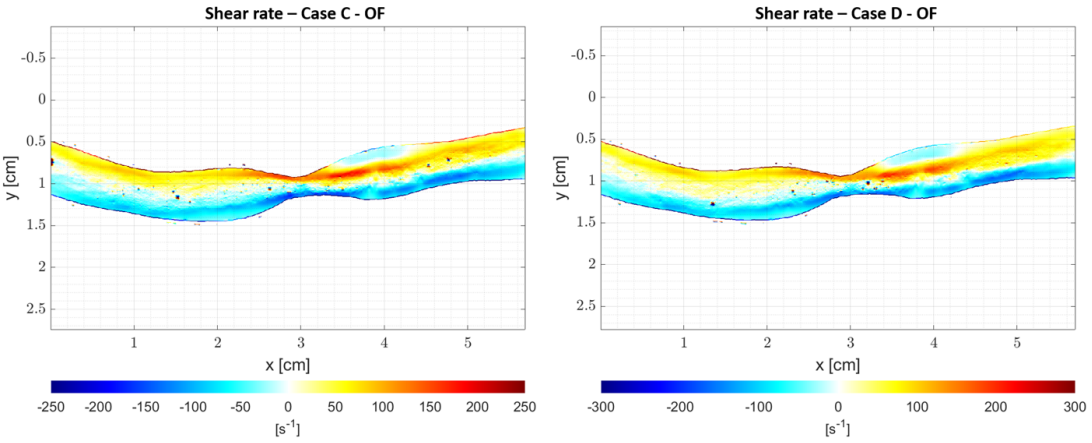

Figure 7.20: Shear rate colormap of stenotic coronary artery. Image on the left: Case C. Image on the right: Case D.

Even in the results shown in Figure 2.11 described in Section 2.5.1 high shear rate values are detected between the recirculating zone and the main jet, despite the geometry of the vessel and stenosis used is different from that used in this thesis. The method presented in this work therefore allow to visualize the shear rate trend in the area of interest (downstream of the narrowing) in order to study the influence of the variation of this quantity with the progression and development of pathologies in coronary arteries.

7.6 U and V fluctuations

In order to try to investigate the possible establishment of turbulent regimes downstream of the restriction zone, the ratio between the velocity of the single motion fields and the time average over 280 velocity fields respectively for the velocity component projected along the x axis (u) and for that along the y one (v) are shown in Figure 7.21.

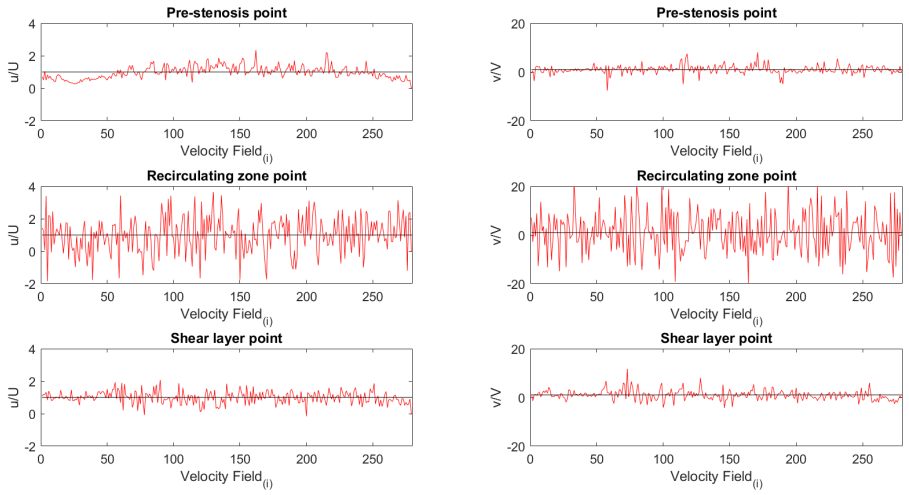

Figure 7.21: Ratio between the velocity along the x (u) axis and along the y (v) axis, normalized for the average over 280 velocity fields (U, V). On the left u/U of a pre-stenosis, recirculating zone and shear layer point. On the right v/V of a pre-stenosis, recirculating zone and shear layer point. Case D.

Even if the Reynolds numbers related to the experiments carried out in this thesis are relatively low, as explained in Section 2.3, due to the presence of abrupt curvatures of the vessel or rapid variations in diameter, turbulent regimes can also arise for Re smaller than the critical values.
In particular, it was decided to try to investigate the fluctuations of velocity along the x (u component) axis and along the y (v component) axis. Recalling that to model turbulent phenomena the velocity can be expressed with the following formula [6]:

$$u = U + u'; \tag{7.2}$$

where U represents the average of the velocity values in a given time interval, while u' is the fluctuation term around the average value. The u/U and v/V ratio shown in the graphs in Figure 7.21 give information on the entity of the velocity fluctuations with respect to the average calculated over 280 frames. To compare the trend of the velocity values in the areas of interest, a point in the region before the stenosis, a point in the recirculating area and a point in the region where the flow is separated (shear layer) were selected. By directly comparing the velocity trends

for the pre-stenosis case and in the recirculating area, it can be stated that in the second case significantly higher oscillation amplitudes are obtained. In particular, the oscillations of the v component reach values up to 20 times the average value. The increase in fluctuations for the v component in the recirculating zone are due to the inversion of the direction of motion of the velocity components and to the presence of displacements along the y direction greater than in the pre-stenosis case in which there are low displacements in the direction perpendicular to that of the principal motion. As regards the fluctuations calculated in the shear layer, values comparable to the pre-stenosis case were obtained.
Because of the low Reynolds numbers of the case in question, due to the presence of noise components in the velocity fields and the uncertainties on the quantitative data (section 9), it is not possible to make any assumptions about the possible establishment of a turbulent regime in a restricted area downstream of the stenosis. However, observing the results obtained, it is possible to state the presence of a greater variability of the velocity components in the recirculating area compared to the rest of the velocity field.

7.7 Considerations

Taking into consideration the results shown above, it is possible to state that both the algorithms used allow to carry out a qualitative analysis of the fluid dynamic patterns that are established in a model of healthy artery and in one of stenotic artery. Quantitative data are affected by uncertainty, especially in the case of large displacements, as discussed in Chapter 4 and 9, which mainly occur in the stenosis area. Contrary, in the healthy case, the results are more congruent to the theoretical values obtained from the law of conservation of mass (7.1). However, by applying the average over multiple fields of motion, as shown in Section 7.3, significant improvements are obtained in terms of visualization of the fluid dynamic patterns of interest. In order to validate the experimental results obtained, in the next chapter comparisons will be shown with the numerical simulations performed on the CAD model from which the phantoms used for the experimental studies were obtained.

Chapter 8

Fluid dynamic simulations

The following Chapter describes the CFD simulations used to compare and validate experimental results both qualitatively and quantitatively. The first part of the Chapter concerns the description of the geometry and the operations that were performed on it before carrying out the simulations. All the settings inserted in the solver are then summarized and presented to obtain a correct representation and description of the velocity fields obtained by the experimental studies. All the results obtained experimentally were also reproduced with CFD simulations in order to compare them and highlight any differences and similarities.

8.1 Domain definition

To obtain models that would allow to faithfully reproduce the geometry of the phantoms, images obtained with angiography on a real patient were used. The reconstruction of the models starting from medical images, such as in this case angiographic images, is carried out with special software that allow to reconstruct the geometry starting from data in DICOM format. This format is one of the main used in the medical field for managing patient data. Within these software it is possible to identify the layers concerning the various anatomical structures present within the image and differentiate them from each other. This subdivision allows to reconstruct the geometry of interest ignoring the other anatomical structures

present within the image. In the specific case used in this Chapter, this allowed to obtain the geometry of the stenotic phantom and the healthy one. Their geometry are complementary to that of the patient from whom the angiographic images were extracted. In this way, it is possible to carry out a study that turns out to be specific for that particular patient and so patient specific.

8.1.1 Geometry generation

The first step that was carried out following the import of the model concerns the reconstruction of the geometry in such a way as to optimize the subsequent discretization. The model was imported in ".stl" format and was modified using the Rhinoceros software [75] and this allow to pass from a point cloud to a polysurface. To derive the polysurface from the model in ".stl" format, the *contour* command of Rhinoceros was first used, which allowed to create curves that surround the model. To use it in the subsequent fluid dynamic simulations it was necessary to extend the model by extending the length of the input and output traits. In fact in the fluid dynamics simulations the solver, following the conditions set at the input, needs to develop the motion in such a way that the velocity conditions at the wall are zero. As can be seen in the Figure 8.1 the vessel represented in green turns out to be longer than the vessel represented in red, precisely because it has been stretched to its ends. Subsequently, with the *surface-loft* command, the lateral surface was reconstructed starting from the curves generated in the previous step. Finally, with the *edge-planar curves* command have been created the upper and lower surfaces of the model that will be used to give the boundary conditions during the simulation. Before exporting the model in ".igs" format, the three surfaces created were joined into a single polysurface using the *join* command. In Figure 8.2 is present the vessel just imported in red and the final result reconstructed in green. The figure shows the different geometric structures that make up the two elements, where the red one is made up of a mesh while the green one is a closed surface.

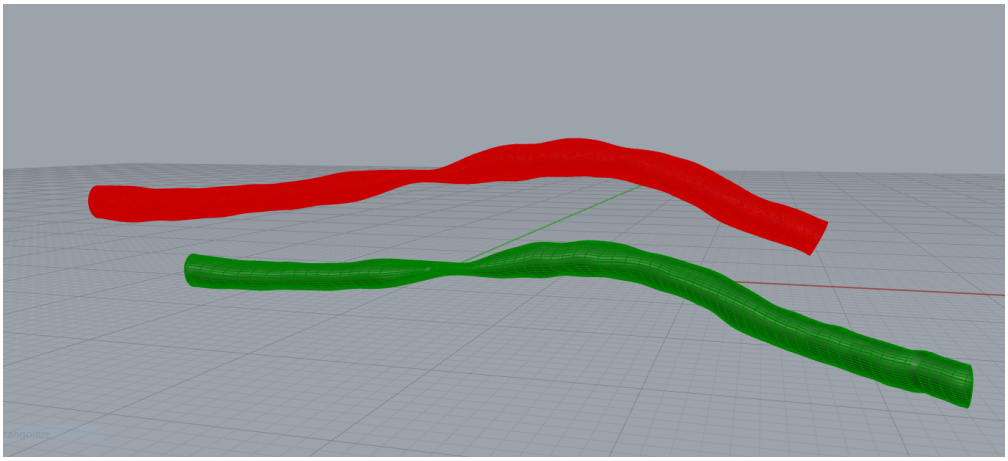

Figure 8.1: Red model represents the newly imported vessel in ".stl" format while the green model represents the final geometry before export.

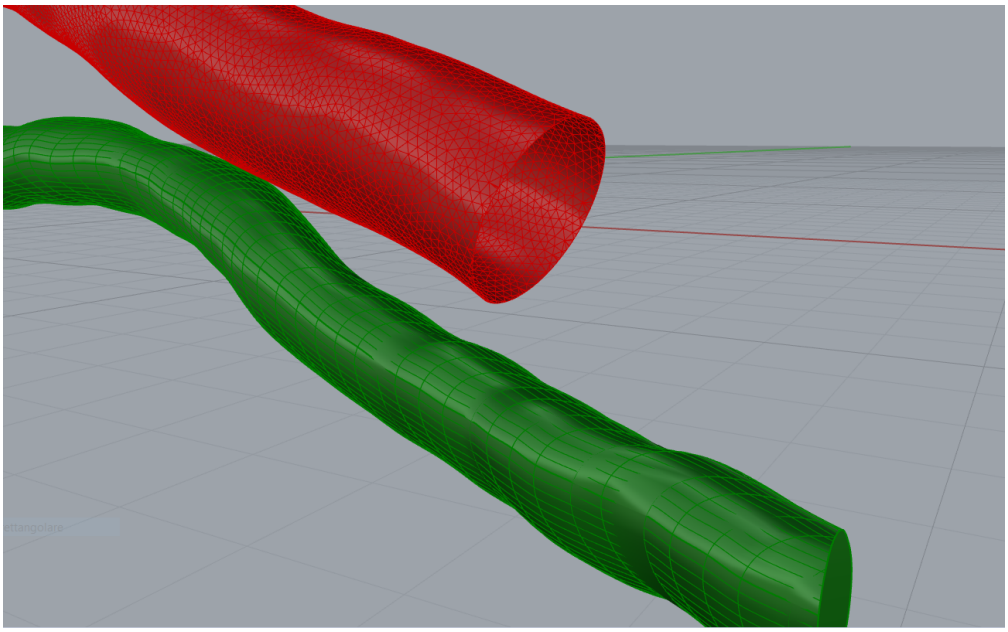

Figure 8.2: Detail of the two geometries, red model consisting of a mesh, green model consisting of a closed surface or polysurface.

8.1.2 Domain discretization

Once the geometry was prepared it was imported in ".igs" format into ANSYS Fluent software [76]. Within the ANSYS Workbench it is possible, in addition to modifying

the geometry, to perform the mesh before analyzing the results. Numerical analysis using the finite volume method, as well as all the other techniques that make use of discrete equations, require a discretization of the domain. This method involves solving the equations in discrete locations on a mesh geometry [77]. The term mesh or grid, identifies the set of nodes, faces and vertices with which the computation domain is divided. The subdivision of the computation volume into infinitesimal volumes implies having a discrete representation of the problem in a finite number of nodes or elements [77]. The determination of a correct calculation grid is fundamental for a correct simulation of the real phenomenon since the greater the number of cells, the more it is possible to have infinitesimals volumes and a practically continuous description, in order to have the most accurate solution possible. On the other hand, a large number of cells implies a considerable increase in the computational cost, in fact the calculation time expands [78].
To obtain a fair compromise between optimal mesh and computational costs, some parameters have been evaluated within the environment dedicated to meshing in ANSYS.
The tetrahedral elements were selected by changing their size and setting it to 0.2 mm that is approximately 20% of the stenosis diameter. To evaluate the quality of the elements, the skewness was displayed and a mesh with greater detail was applied to the edges of the vessel. The details of the mesh are summarized in the Table 8.1. The Figures 8.3 and 8.4 show the final result following the mesh. From the detail on the outlet section of Figure 8.4 it is possible to observe how the mesh has been thickened on the wall due to its importance in the description of the flow.

Variable name	**Healthy vessel**	**Stenotic vessel**
Element size	$0.2mm$	$0.2mm$
Type of element	$Tetrahedral$	$Tetrahedral$
Inflation	$5 - layers$	$5 - layers$
Number of nodes	114875	113094
Number of elements	351001	309817

Table 8.1: Principal parameters of mesh for healthy and stenotic models.

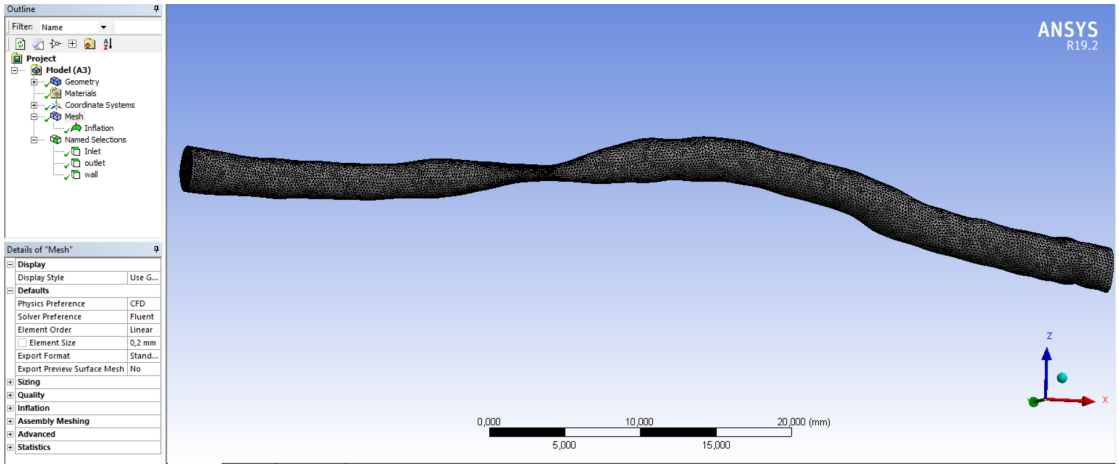

Figure 8.3: Mesh of the entire stenotic vessel.

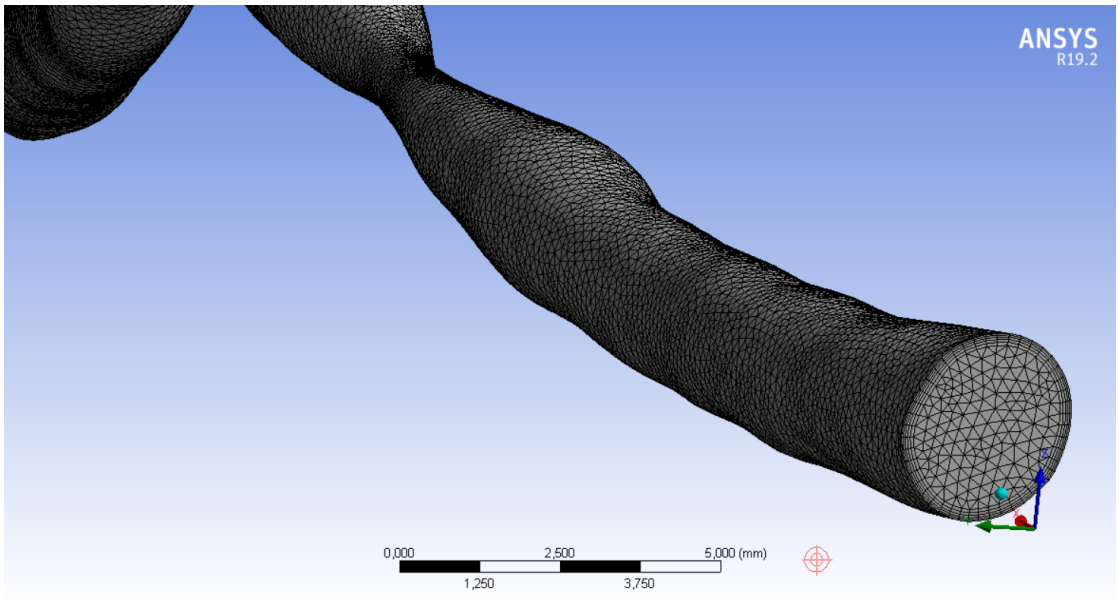

Figure 8.4: Detail of the mesh of the outlet of the stenotic vessel.

8.2 Solving

After the steps explained in the previous sections, the import of the model with mesh into Fluent was carried out. The calculation or Solving phase can be summarized as the set of all the settings to be inserted within the Fluent software, in order

to obtain the success of the numerical simulation. The incompressible fluid was defined and the simulations were carried out in steady state. From the calculation of the Reynolds numbers that are established inside the vessels, the conditions appear to be of the laminar type.
The solving step allows to solve the Navier-Stokes equations, whose analytical solution is limited to simple geometries and simple motion cases. In fact, by discretizing the volume of fluid it is possible to generate a calculation grid within which it is possible to solve the equations.

8.2.1 Laminar model

As previously mentioned, the model used for the simulation was the laminar one. This model was chosen since the Reynolds numbers calculated inside the vessels are low. In the literature there are several studies that involve use of a laminar model to assimilate the motion inside the coronary arteries as described for example in [79]. Although the geometry of the coronaries is very irregular, the flow-rates and velocities inside them do not cause high Reynolds numbers. The laminar model, therefore, turns out to be a good approximation of the description of the motion inside them.
First of all, the viscosity and density characteristics of the fluid described in Section 5.1.1 were set and they were imposed in the internal domain of the model. The no slip condition was imposed on the walls and they were assumed to be rigid. This could introduce an error in the simulations since the blood vessel walls are not rigid but have muscle layers within them [13]. This simplification introduces an error which, in the case of coronaries, does not introduce an excessive departure from reality. In fact, as described in [24], the coronaries, among the arteries present in the circulatory system, are those with less elasticity. Furthermore, during the diastolic phase in which there is the greatest flow-rate inside them, their elasticity is reduced by heart movements.

8.2.2 Boundary conditions

The boundary conditions allow to uniquely determine the solution of the adopted system. They describe the flow variables and were applied to the surfaces of the fluid domain. In this case the setting of the boundary conditions are the inlet velocity and the pressure in the outlet surface. The first was calculated starting from one of the flow-rate investigated and shown in Table 7.1 and Table 7.2. The second was obtained from the sensors connected to the circuit during the tests.

8.2.3 Solution method and convergence

The definition of convergence is to be identified in the verification of some conditions in order to observe that the iterative calculation performed converges to the real solution. That is, the result of the iterations is sufficient to describe the real phenomenon.
Generally the convergence condition is controlled through residual monitoring. They represent for each imposed equation, the difference between two successive iterations. When these settle on values that are constant in the time, the solution can be said to be convergent.
Figure 8.5 shows the trend of the residuals, as it is possible to observe as the number of iterations increases their value decreases. This shows how the simulation is converging towards a solution.

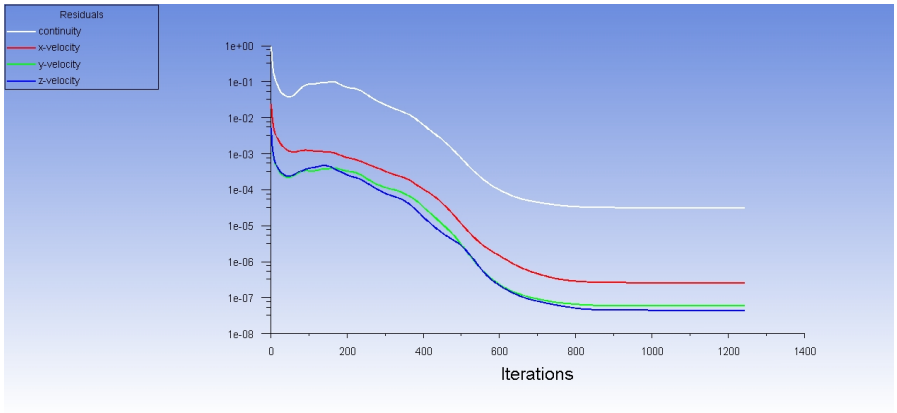

Figure 8.5: Trend of residuals during simulation.

For the simulations carried out, the SIMPLE method was used in which the algorithm solves the equations sequentially using the relationship between velocity and pressure to impose the conservation of the masses and obtain the pressure field within the geometry [78].

8.3 Analysis of results

The following paragraph exposes and describes the results obtained by imposing the same conditions that were recorded during the experimental acquisitions. This allows to highlight the important fluid dynamics parameters in the cardiovascular field and to have a term of comparison with the experimental results. In particular, all the results obtained from experimental data are compared to verify the differences in view of future improvements.
The reasons for the differences found between the experimental results and those of the simulations will not be described in this section. They will be deepened and investigated in Chapter 9.

8.3.1 Velocity fields

The result shown in Figure 8.7 is comparable with the mean of the velocity range discussed in Chapter 7 for the same cases. In order to better compare the results, in the case of the simulations the vessel was cut with a plane. This made it possible to obtain a representation similar to the two-dimensional one obtained from the experimental results.
Observing Figures 8.6, 8.7 and 8.8 it is possible to notice how the velocity scales have a greater range than the cases presented in the experimental results. According to the equation (7.1) the maximum velocity value is found inside the stenosis. Among the cases shown, there are no particular differences as the flow-rates and therefore the input velocities increase. A slight difference is observed in the width of the jet that forms downstream of the stenosis.
As described in paragraph 2.3.1 the effects of the restriction are more visible as the flow-rates increases. It is possible to better appreciate the differences that occur

between the various cases by observing the length of the recirculating zone, which will be discussed later in this Chapter.

Observing the results of the simulations it is possible to note that, while the velocity in the pre-stenotic zone is comparable to that of the experimental results both in qualitative and quantitative terms, the velocity inside the stenosis is comparable only in qualitative way. In fact, inside the stenosis, the velocity values shown in the simulation results turns out to be greater than that observed in the experimental results. From a first observation, the qualitative trend of the velocities seems to be comparable with those presented in the experimental results despite the fact that the recirculating area in the latter is less large. However, the qualitative description, with the presence of the lateralized jet downstream of the stenosis, appears to be comparable in all cases for both experimental and numerical results.

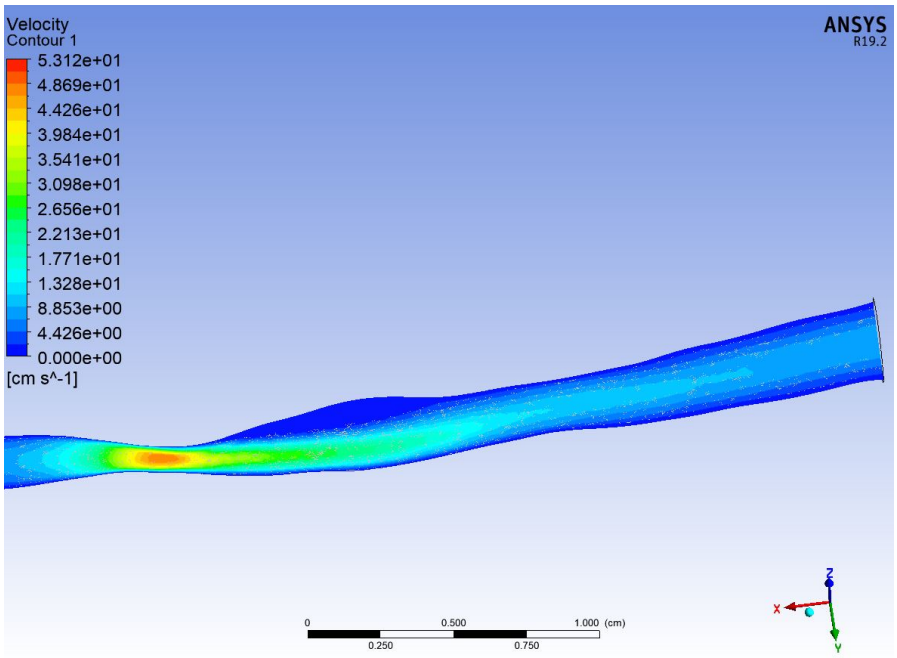

Figure 8.6: Contour of the velocity on 50 levels, on a plane that cuts the stenotic vessel from the pre-stenotic area to the outlet area. Case B.

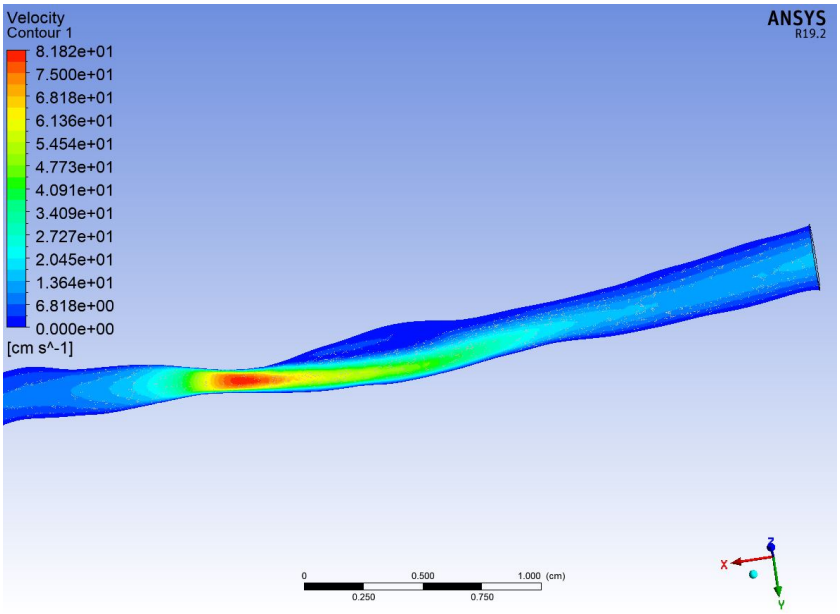

Figure 8.7: Contour of the velocity on 50 levels, on a plane that cuts the stenotic vessel from the pre-stenotic area to the outlet area. Case C.

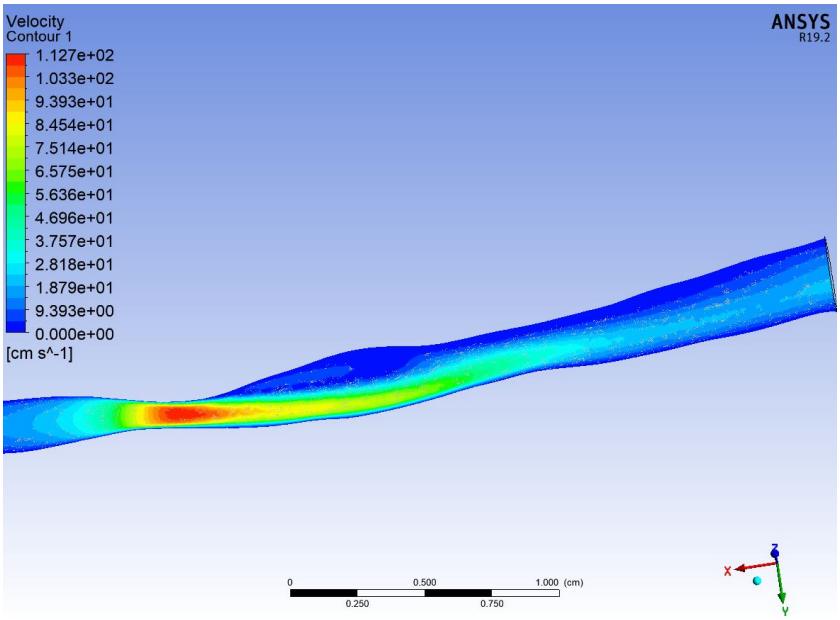

Figure 8.8: Contour of the velocity on 50 levels, on a plane that cuts the stenotic vessel from the pre-stenotic area to the outlet area. Case D.

In Figure 8.9, eleven planes have been selected, they are placed at approximately the same distance from each other and perpendicular to the main axis of the coronary model. This representation allows to observe how the fluid inside the vessel acquires a three-dimensional motion following the restriction.
In the area of the recirculating bubble, it is observed that the lowest velocity values are confined to the upper part of the vessel, while the formation of the jet is observed in the lower part.
By observing the last section it is possible to notice how the velocities with higher intensity are located on the right side of the section, while in the previous sections the regions with higher velocities were confined to the jet zone. This allows to appreciate the three-dimensional structure of the motion inside the vessel.
The analysis of three-dimensional structures is of interest from the point of view of cardiovascular flows as described in [80]. Some hemodynamic indices based on the calculation of helical indicators can give information on the formation of atherosclerotic plaque.

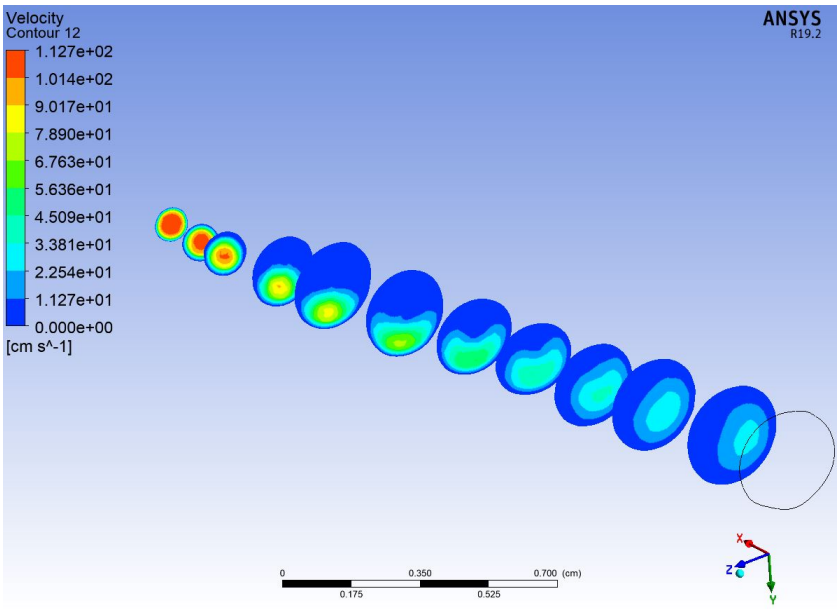

Figure 8.9: Contour of velocity on eleven planes perpendicular to the main axis of the vessel. Case D.

8.3.2 Streamlines

The streamlines were also plotted for the results relating to the simulations. In fact, these allow to highlight the formation of any secondary and or disturbed flows which, as explained in the paragraph 2.5.1, are relevant to the development of the atherosclerotic pathology. Differently from the experimental results, in this case the streamlines were plotted both on a plane that cuts the vessel along its main direction and on the three-dimensional representation.
Figures 8.10, 8.11 and 8.12 allows to highlight in a very precise way the formation of the recirculating zone. For all three cases represented in the figures it is possible to observe the recirculating area highlighted by the streamlines.

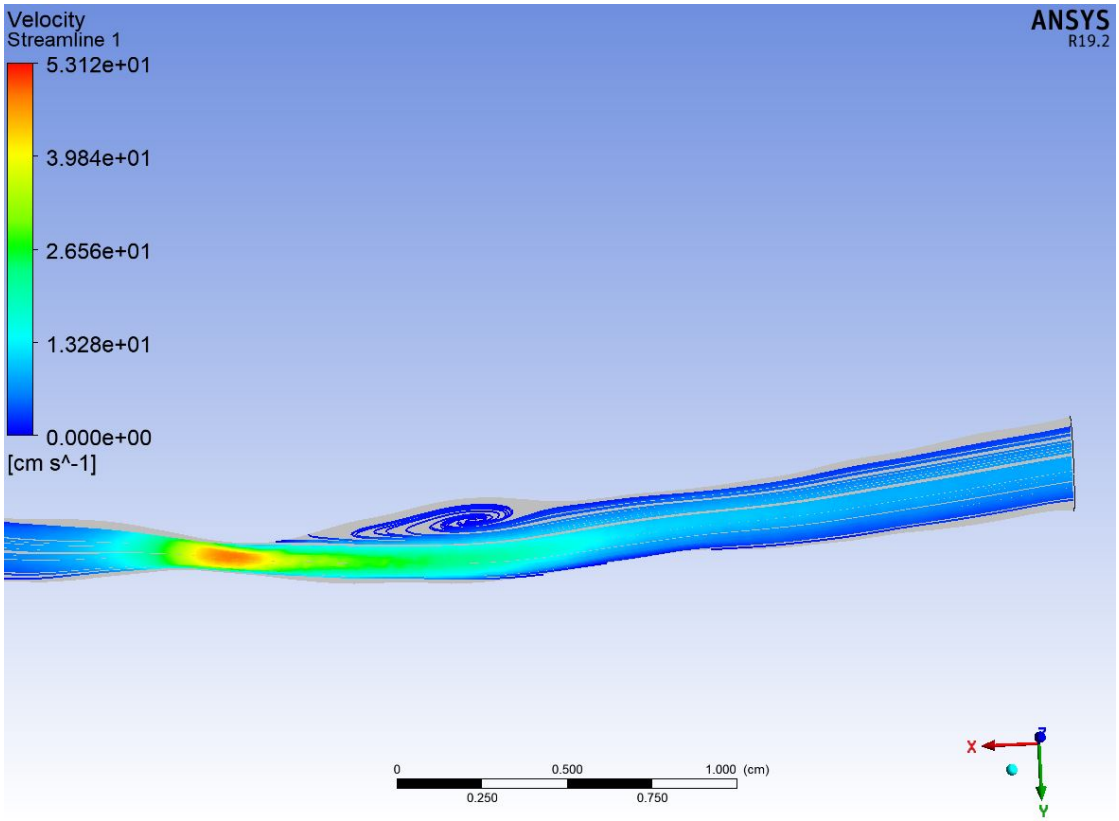

Figure 8.10: Velocity streamlines on a plane that cuts the stenotic vessel. Case B.

Contrary to the experimental results, the results of the simulations allow to observe the presence of the recirculating zone also for Case B (Figure 8.10). In the reported Figures a flow separation region is clearly visible, in which there is the possibility of forming a stagnation point. The latter is not visible in the results of the OF nor in those of PIV for the low flow-rates, related to cases A and B. Its identification can be important since as described in [81] and [24] the formation of a stagnation point can cause the formation of thrombus with eventual release of the same into the bloodstream. The presence of abrupt geometry variation causes a deviation from the regular flow geometry as is also highlighted in the results reported in [22].

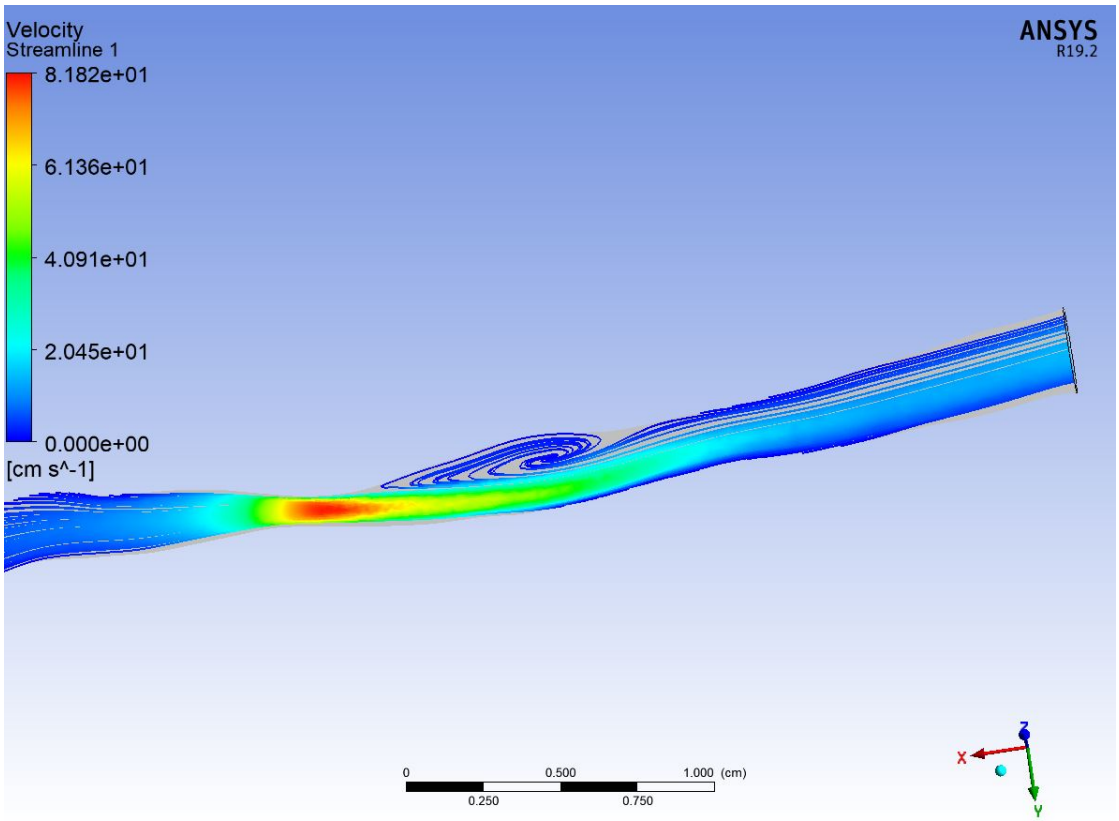

Figure 8.11: 3D representation of the velocity streamlines in the stenotic vessel. Case C.

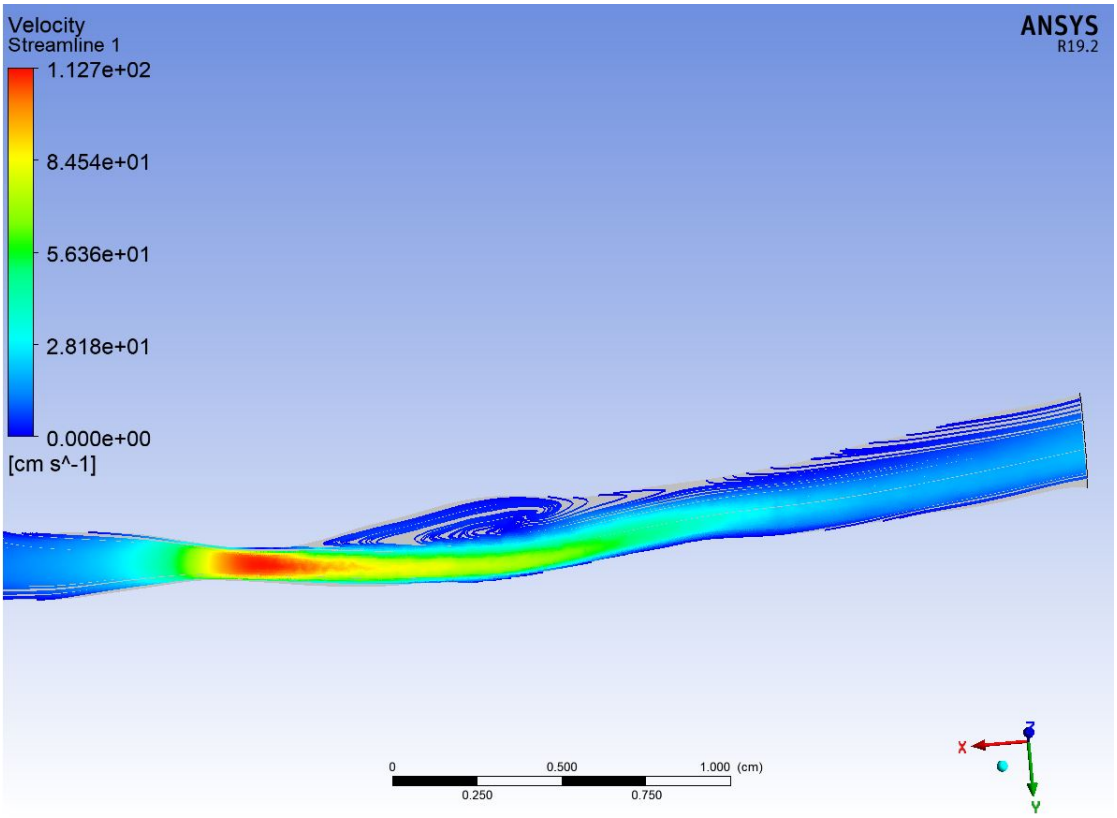

Figure 8.12: 3D representation of the velocity streamlines in the stenotic vessel. Case D.

Figure 8.13 shows the same result of Figure 8.12 but in a three-dimensional representation. This allows to highlight the formation of a lateralized jet with the recirculating area placed in the opposite direction and confined to a single portion of the vessel.

The figure relating to the three-dimensional streamlines allows to observe how, following the recirculating area, the laminar flow is re-established. With the image of the three-dimensional streamlines, Figure 8.13, it is possible to accurately observe the characteristics of the motion in the area behind the recirculating zone. In fact, unlike the experimental results, in this case it is possible to observe how the flow does not immediately return to the laminar motion. From a single observation of the experimental results it would seem that the motion has returned to laminar after the recirculating zone.

However, the flow extensions that were created before carrying out the simulations proved to be sufficient since the flow in the exit surface can be considered laminar.

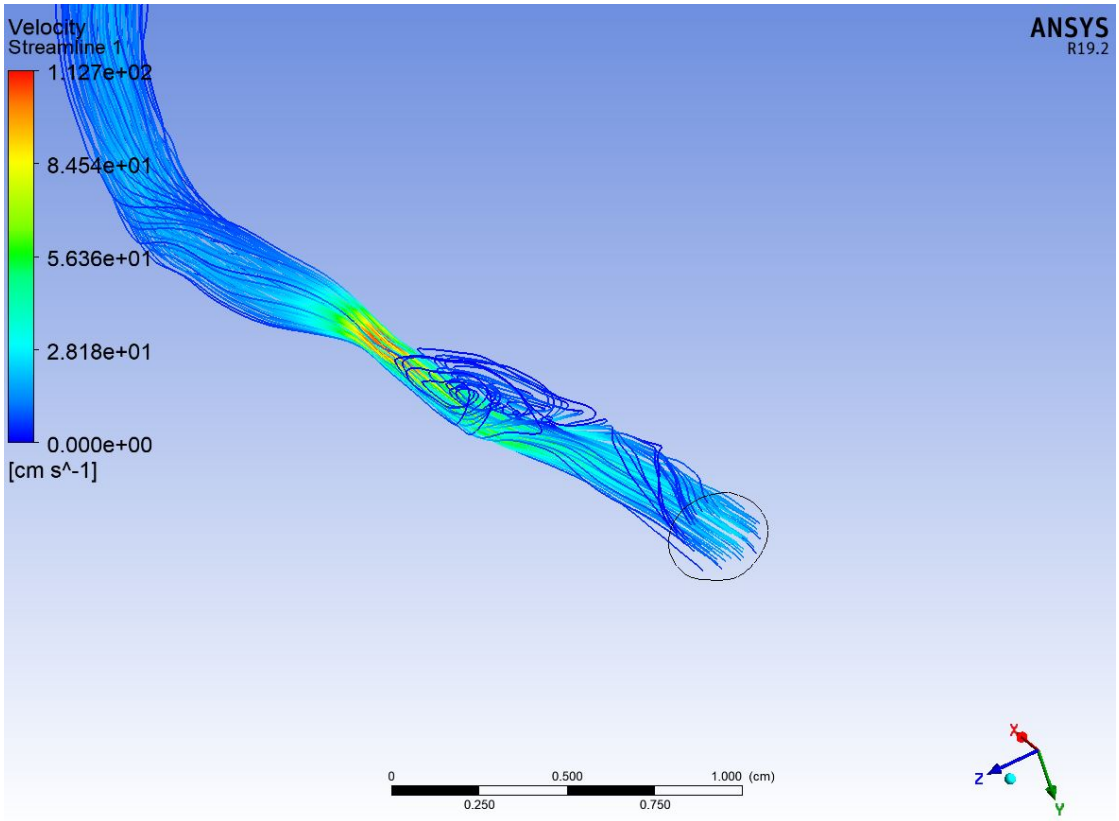

Figure 8.13: 3D streamlines of the stenotic vessel. Case D.

8.4 Velocity profiles

Figures 8.15 and 8.16 show the velocity profiles relating to case C and case D of the stenotic coronary artery. Figure 8.14 highlights the sections in which the velocity profiles have been extracted. In particular, it was decided to observe the velocity profiles in the area of the restriction and downstream of the latter.
The first section has been selected within the stenosis in which the motion of the fluid undergoes an acceleration due to the restriction. The second section relates to the post-stenotic area in which the recirculating zone with the inversion of motion is observed.

Comparing this results with that of the experimental results shown in Chapter 7, it is observed that a higher speed is obtained from the simulations which also have a zero wall velocity. This last condition occurs since the zero wall velocity has been set as a boundary condition, obviously this does not occur in the experimental results.

The images on the left in Figures 8.15 and 8.16 shows the velocity profile present inside the stenosis. As expected, the velocity takes on a much higher value and this values are quite similar with those reported in Table 7.2. Also in this case the velocity differs greatly from the value assumed by the experimental results. As will be explained in 9 as the speed increases the difference between the two techniques increases.

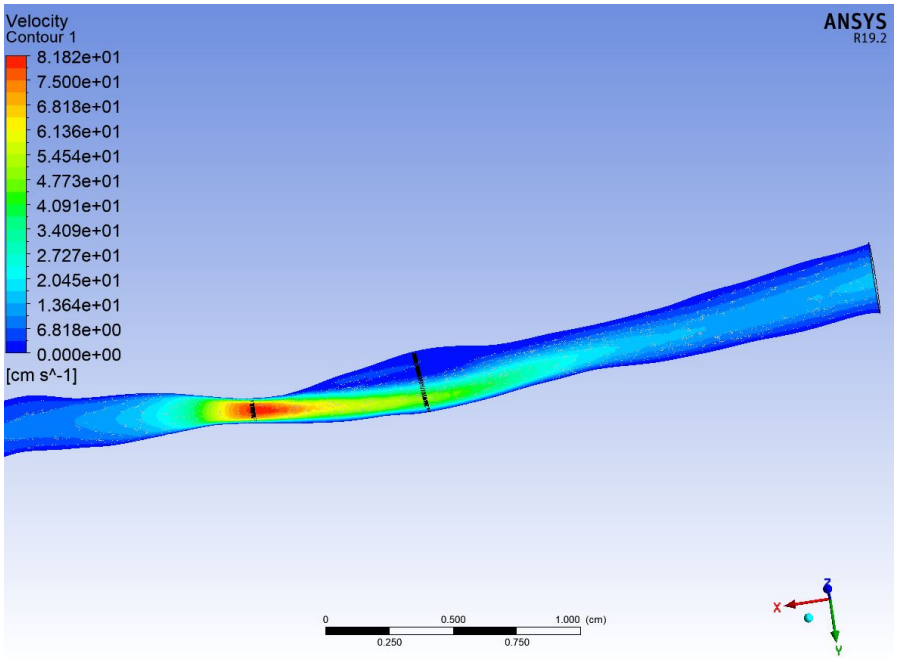

Figure 8.14: Representation of the vessel with the areas in which the velocity profiles have been extrapolated highlighted in black.

Finally, the images on the right in Figures 8.15 and 8.16 shows the velocity profile relating to the post-stenotic zone. In particular, in this image it is clearly visible the inversion of the motion that occurs due to the shrinkage of the vessel. This condition is of interest to highlight the areas that can stimulate the development

of atherosclerotic pathology. Furthermore, observing the scale it is possible to note that in the case with higher flow-rate (case D) also the velocity in the recirculating zone increases becoming more negative than in case C.

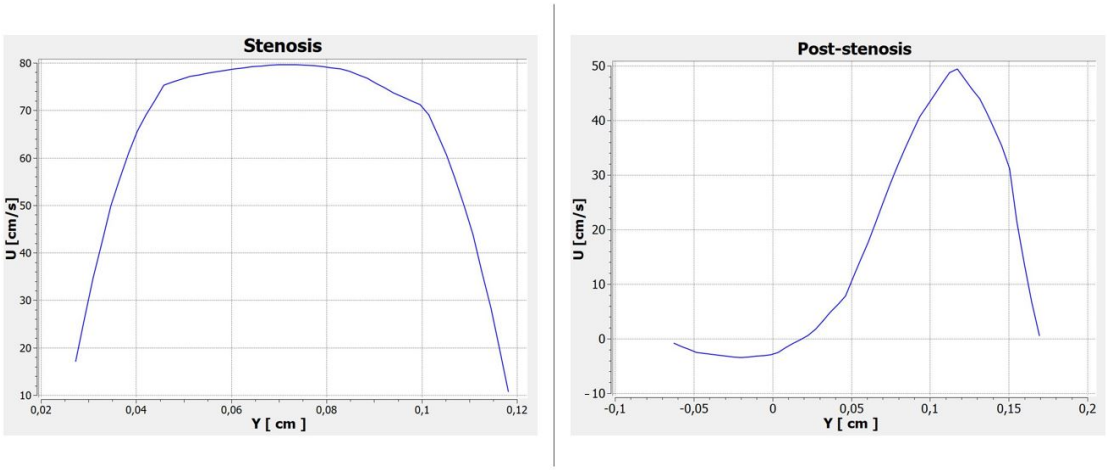

Figure 8.15: Velocity profile of a section in the stenotic and post-stenotic zone, U component of velocity. Case C.

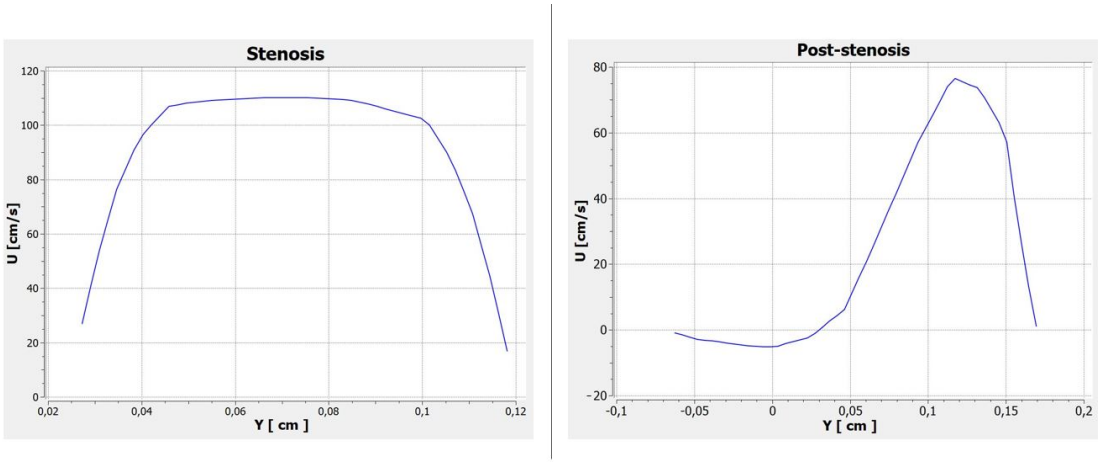

Figure 8.16: Velocity profile of a section in the stenotic and post-stenotic zone, U component of velocity. Case D.

The main difference with the experimental results is due to the wall velocity. In the results of the simulations the latter reaches values close to zero while in the case of the experimental results the assumed values remain high even on the wall.

This is due to numerous factors but mainly to the presence of reflections due to the geometry of the vessels which cause the detection of movement also on the wall as explained in 9.

8.5 Shear rate

The Figure 8.17 show the shear rate that is the variation of the velocity along the main axis of the vessel (x), with respect to the y coordinate in the Case D. Only these case has been reported and described as those relating to lower flow rates have a similar trend. By observing the figure, it can be seen that the greatest values occur in the restricted area where the variation between the speed at the wall and the velocity inside the model is greater. Furthermore, high values are also reported in the shear layer area, that is the separation region that is created downstream of the stenosis between the low speed of the recirculating area and the high speed inside the jet. This result allows to validate the experimental results from a qualitative point of view.

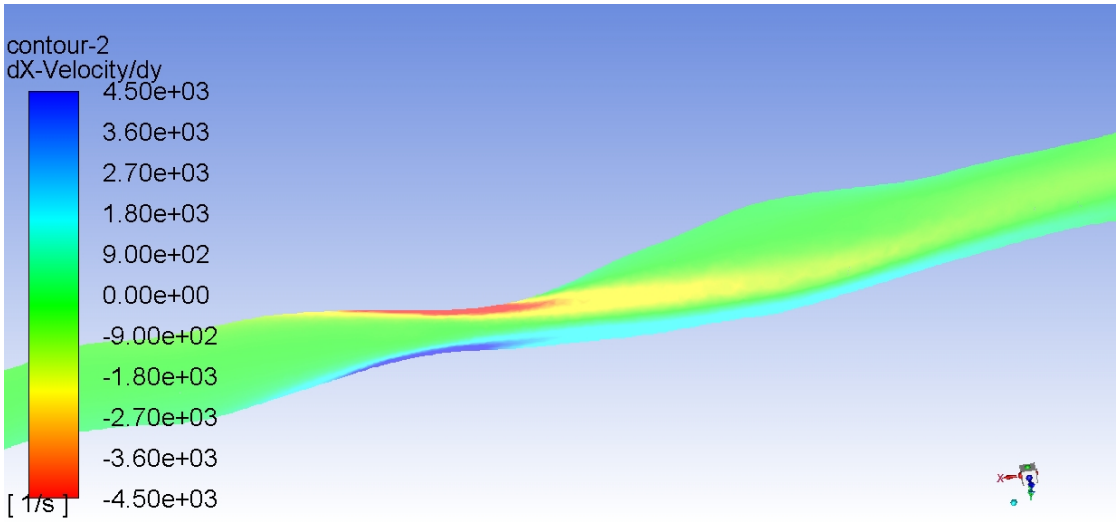

Figure 8.17: Shear rate. Case D.

While as regards the values assumed by the shear rate they differ considerably from those observed in the experimental results of PIV and OF. Although the

geometry representation is different, a trend and values of the same order of magnitude are also represented in [23].
As described in Section 2.5.1 the shear rate is interesting to evaluate since, as described in [26], its value affects the motion of red blood cells and the interactions that occur between them. For examples, in areas with high shear rate values, red blood cells tend to aggregate less easily and their rotation is facilitated, thus decreasing the viscosity of the blood [26].

Chapter 9

Discussion on the errors of the experimental method

In this Chapter there is first a comparison between the results of all the methodologies used with the description and explanation of the differences found. Particular attention was paid to the reasons that led to the differences between OF, PIV, simulations and analytical results. In the second part there is a detailed analysis of the sources of errors that have been detected. In particular, the errors were divided according to the source that generated them.

9.1 Comparison with analytical and numerical data

Figures 9.1, 9.2 show the trends of the maximum velocity values as the flow-rate increases in the healthy and stenotic vessels. The four curves represent the values calculated analytically, with OF, PIV and with CFD simulations. For the calculation of the analytical values, Tables 7.1 and 7.2 reported in chapter 7 was taken as a reference.
Considering a cylindrical geometry inside the vessels and assuming a Poiseuille

type of motion, the maximum speed was obtained through the relation [6]:

$$V_{avg} = \frac{1}{2} V_{max} \tag{9.1}$$

where V_{avg} is the velocity value calculated from the table using the mass conservation equation (7.1), while V_{max} is the maximum value reached within the velocity profile that is assumed as parabolic. By inverting the relationship it was possible to obtain the theoretical maximum value and calculate it analytically.

An arbitrary region of the motion field for the healthy artery and the region of restriction for the diseased artery were chosen to obtain the maximum velocities for PIV and OF. At the regions considered, the section for which the maximum speed value was calculated was taken together with 4 adjacent sections. Subsequently, the mean and standard deviation of the 5 maximum values within the considered sections were calculated.

For the selection of the maximum velocity value related to the simulations, the vessels were first cut with a longitudinal plane, then the velocity profiles were extracted in order to take the maximum point of the profile.

By observing the figure relating to the healthy coronary artery (Figure 9.1) it is possible to note that the similarity between the results of the various methodologies is greater than in the case of stenotic coronary artery (Figure 9.2).

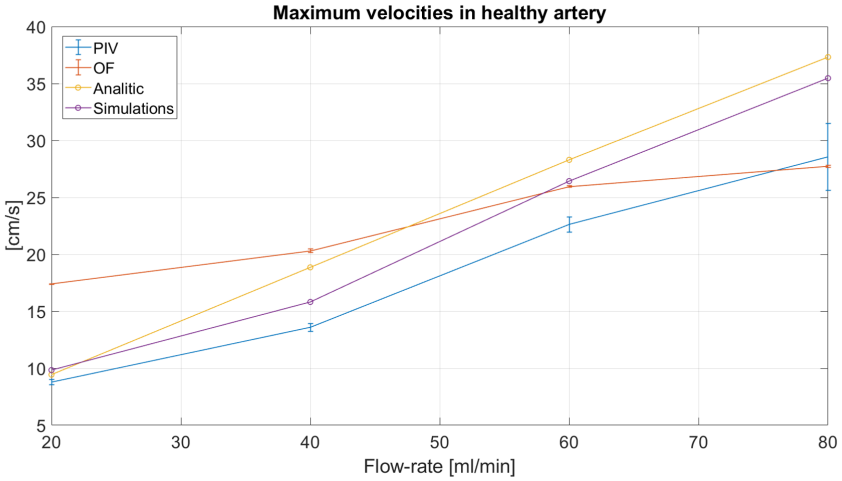

Figure 9.1: Comparison of the maximum velocity values assumed as the flow-rate increases in the healthy vessel.

In particular, the trends of the curves relating to the simulations and results of PIV closely approximate the results obtained analytically. On the other hand, while the distance between the curve relative to the simulation and that of the analytical results remains almost constant, the distance between the PIV results and the analytical one increases as the flow-rate increases. Furthermore, from the graph it can be observed that as the flow-rate increases there is a considerable increase in the standard deviation compared to the average value for PIV.
For the OF, an increasing trend is observed, but which is not in line with the trend of the other curves. In fact, the increase in velocity for the first values and for the last one is considerably different from those assumed. From Figure 9.2 is possible to observe a different trends compared to the previous case. In fact the maximum velocity inside the stenosis obtained through OF and PIV do not follow the trend of the other two curves. Furthermore, the difference between the curves becomes increasingly greater as the flow-rate value increases. Also for the values of the simulations, for the higher flow-rates there is a deviation from the analytically calculated value. Although they have an increasing trend, the maximum speed values measured with PIV and OF turn out to be an excessive underestimation that does not make them usable for quantitative calculations.

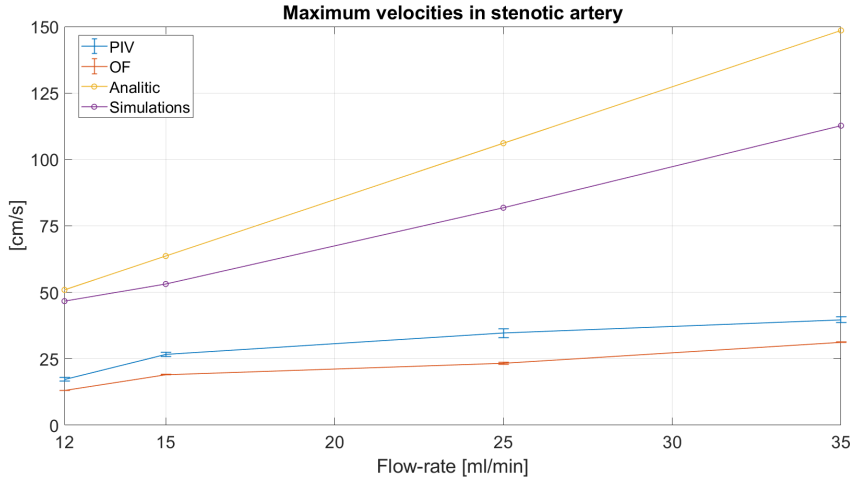

Figure 9.2: Comparison of the maximum velocity values assumed as the flow-rate increases in the stenotic vessel.

9.1.1 Sources of errors

Following the results shown, comparisons between theory, simulations and analytical results, it is possible to analyze and investigate some of the causes of errors that contributed to the differences between the various techniques investigated. Some sources of error present in the results are found both for OF and for PIV and therefore are configured as systematic errors of the experimental setup. Others, on the other hand, are typically of the technique used.

Errors caused by geometry

In particular, with regard to the errors common to both techniques, the geometry of the models has a significant effect. In fact, although the reproduction of the patient's anatomy is very good, the geometry does not allow its precise measurement of its characteristic dimensions. The diameter of the model inside the vessel does not have a perfectly defined geometry. In fact, the thickness of the vessels is also taken into account when measuring with the caliper. Subsequently, the thickness of the vessels is subtracted from the result obtained on the basis of the data provided by the model manufacturer for the calculation of the analytical data. Obviously the result obtained will not fully conform to reality. This introduces a systematic error which affects all results. Furthermore, its determination, for a possible elimination or attenuation, is not easy to implement in all the geometry. This allows to partially explain the difference in results between CFD simulations and analytical results. In fact, the latter was obtained starting from geometric considerations made on the basis of geometry measurements. The CAD model used to reconstruct the geometry, on the other hand, had some differences that were taken into account for example in the inlet section. Observing the measurements of the model carried out experimentally and those of the CAD model in some points, a diameter error of 10% was observed. Another error deriving from geometry is that on analytical calculations. In fact, to perform them and to calculate the maximum speed, a Poiseuille motion was assumed inside the pipe. Among the conditions of validity of the Poiseuille motion is that of being in a cylindrical pipe, which is not valid in the models used for the experiments reported [6]. This approximation introduces

errors and overestimates especially in the area of the stenosis in which a sudden variation of the geometry is observed. Furthermore, the curvature of the vessel does not allow to identify the edges in two-dimensional images.
A clear example of the differences introduced by calibration and geometry errors is shown in Figure 9.3. This image shows the lengths of the recirculating area for all cases in stenotic coronary model. It is possible to observe how for CFD measurements the data are considerably greater than those of PIV and OF. Although an increase in the length of the recirculating zone is observed in the results of PIV and OF for the cases C and D, the irregular geometry and the errors introduced by it respectively cause a lack of detection for the lower flow-rates (cases A and B) and an underestimation for higher flow-rates (cases C and D). Furthermore, the lack of detection of the recirculation zone in the experimental results for cases A and B is also influenced by the limited spatial resolution linked to the number of particles in the fluid domain, as will be explained in the following sections.

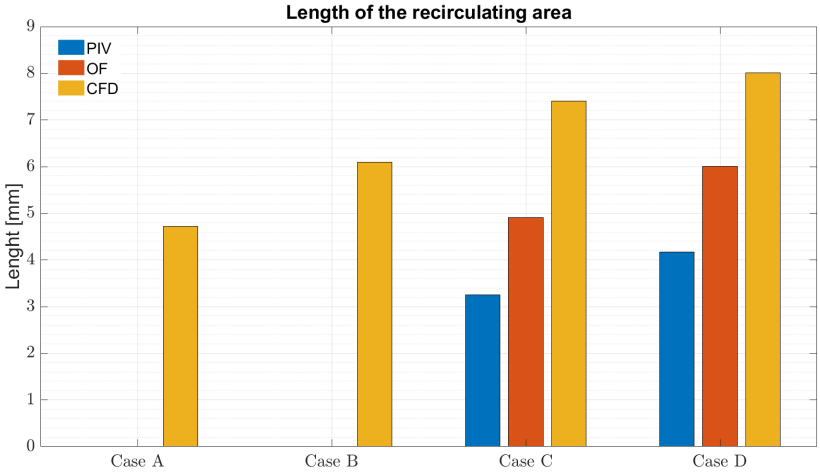

Figure 9.3: Bardiagram representing the lengths of the recirculating zone as the flow rate varies, for PIV, OF and CFD simulations.

Errors due to image particles

Although the particles have allowed to significantly improve the quality of the results obtained, some sources of error due to their visualization are still present.

Figure 9.4 shows one of the major problems due to image particles. In fact, in the area of the stenosis for higher flow-rates it is noted how the particles are elongated and not point-like. This phenomenon occurs since within the restriction the particles undergo an acceleration which is too high compared to the exposure time of the camera. This causes the detection of a "strike" that represent the motion of the particle during the exposure time.

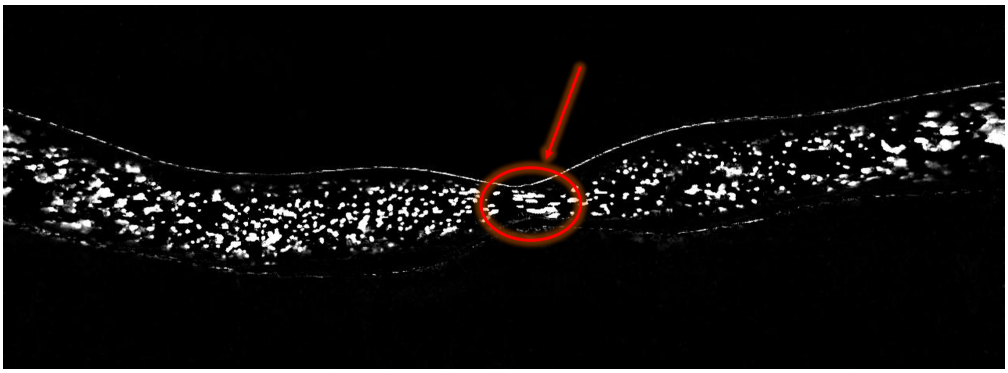

Figure 9.4: Particular on the particles. Effect of high velocities within the stenosis causing the detection of streaks. Case D.

In Figure 9.5, however, it is evident that this phenomenon is largely reduced for lower flow-rates. This is due to the lower acceleration of the particles within the restriction zone.

Another observation that can be made by observing the two figures concerns the distribution of the particles within the model. In fact, it is possible to observe the presence of some areas in which the density of particles present is very low compared to other areas in which the particles are more concentrated. These two factors contribute to the detection of slower velocity values than in reality. In fact, as regards PIV, the presence of empty areas inside the interrogation window causes a lowering of the speed value inside the window itself. Recalling what explained in Section 3.6.5 about the error deriving from the use of images with particles in the OF, it is possible to notice that a low density of the particles contribute to the increase of the error. Furthermore large displacements affect the error by increasing it, since they are directly proportional.

As regards the PIV, the resolution is too low and in the stenosis this causes a

incorrect resolution of the motion. Since the particles move very fast within the restriction, these velocity values are only detected in a part of the interrogation windows. By averaging with the remaining values within the window, the high speed value is attenuated.

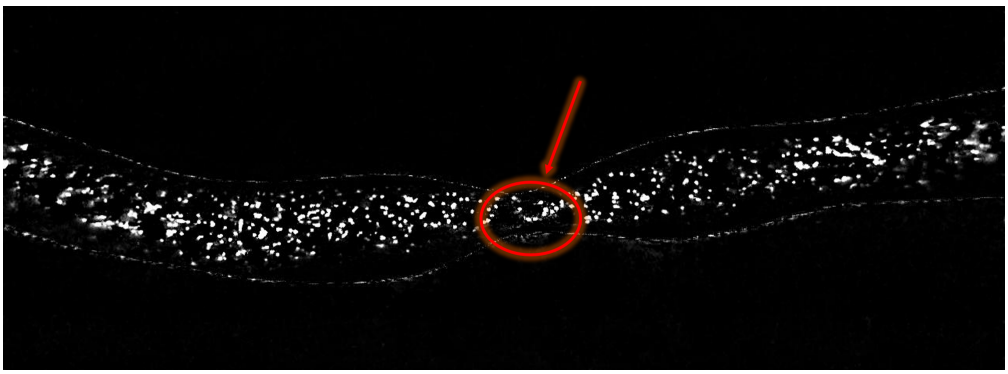

Figure 9.5: Particular on the particles. Effect of velocities within the stenosis, the particles are represented as dots. Case A.

Errors due to setup

Part of the errors also come from the setup measurements. Although they were repeated a sufficient number of times, the tests carried out with the *graduated cylinder-chronometer* technique led to the introduction of uncertainty. In fact, both the synchronization between the start of the chronometer and the fall of the first drop of fluid inside the cylinder and the stop of the chronometer following the achievement of the predetermined volume of fluid led to errors in the tests. These errors are reflected in the real-flow rate value which could assume a variation from the one measured and used for the calculations. As briefly mentioned in paragraph 7.1 this type of error has a great influence on the flow rates imposed for the experiments with coronary stenotic. In fact, since the acquisitions were made after those of the healthy coronary artery and therefore the circuit had been in operation for a long time, this contributed to the accumulation of particles. Accumulation was greater in areas where restrictions or valves were present and contributed to less flow control. The imposed flow rate values were those of the circuit characterization described in Section 5.11, but this error led to a detection

of lower flow-rates as shown in Table 7.2. The use of a flow-meter that allows to measure the flow-rate of a fluid and therefore to automate the process could have a positive effect on this type of error.
Another source of error due to setup is that relating to light sources. In fact, although the lighting conditions on the vase were controlled using LED light described in 5.2.3, the influence of the external lighting conditions is present in the shots. This contributed to the detection of reflections whose effect is amplified by the curved geometry of the models.
Finally, the observations, comparisons and considerations on the results and on the sources of error reported in this chapter are an excellent starting point for the reflections and conclusions that will be addressed in the next one.

Chapter 10

Conclusions

10.1 Considerations on OF and PIV

From the direct comparison of the performances of both technique examined in this thesis it can be inferred that the OF allows to carry out experiments both with continuous and particle tracers, while this is not possible with PIV. Furthermore, the OF was found to be more sensitive to the conditions of the input images (for example rapid variations in brightness between two frames) which causes the presence of some outliers in the velocity fields. The PIV allows to adjust the size of the interrogation windows based on the size of the hypothesized displacement between the frames in order to improve the accuracy of the results. As for the spatial resolution, while in the PIV application it is determined by the dimensions of the interrogation windows, the OF has a resolution of one vector for each pixel. As described in chapters 3 and 4, both algorithms produce errors in the estimation of velocity if the displacements between two frames are too high, as has been observed by the analyzes applied to the stenotic model. Another aspect to take into consideration concerns the computational costs associated with both methods which can influence the goodness of the same. Regarding this aspect, a significant difference was found between the two techniques. This difference was highlighted during the analyzes carried out on an increasing number of frames to obtain the averaged motion fields. The timing has expanded as the number of frames analyzed

increases. For example, for a 280-frame time-resolved analysis, the OF takes about 1,5 hours while PIVlab takes about 10 minutes. To further evaluate the growth trend of computational costs as the number of frames varies, time-resolved analyzes with 4000 frames were carried out, which led to times of the order of 24 hours for the OF and 2 hours for PIVlab.
In conclusion, it can be stated that both algorithms have both positive and negative aspects. The choice of the algorithm is linked to the type of study to be conducted. In particular, to have a better visualization of the fluid dynamic patterns it is advisable to choose OF because it allows to maintain a high spatial resolution. This can be observed in the results relating to the visualization of the recirculating zone and separation region of the jet downstream of the restriction. However, in order to have a more reliable quantitative analysis, it is recommend the use of the PIV, which has allowed to obtain numerical results more in line with analytical calculations and CFD simulations.

10.2 General conclusions

Following the experiments described and the results shown in the previous Chapters, it can be stated that the use of a particle tracer rather than a continuous one allows to more accurately approximate the motion of the fluid inside the coronary phantoms. From a qualitiative point of view it is evident that the fluid dynamic patterns deriving from the experimental analysis with particles are congruent both with the data reported in the literature and with the numerical simulations performed.
The realization of the set-up described in Chapter 5, reproducing the fluid dynamic conditions inside the coronary arteries, allows to carry out experimental studies on the motion fields inside them. Starting from the physiological values of flow-rates in the coronary arteries, relatively low velocities are obtained, such that it was possible to carry out the PIV technique using the built-in setup, which is much cheaper than the setups most used in literature, which have prices starting at 100,000$ [82].
As regards the quantitative data, the method is subject to errors found especially in

the case of the stenotic artery. In fact, in the model narrowing area, the proposed techniques tend to underestimate the velocity values with respect to the theoretical and simulation results, as described in Chapter 9. The velocity fields obtained allow to have a good qualitative visualization of the flows that are established inside the vessels and which are at the basis of numerous theories on the development and progression of atherosclerotic plaques (Section 2.5.1). Starting from these quantities it was possible to calculate further ones of specific interest in the cardiovascular biomechanics field. However, at the moment only the qualitative aspect of these quantities can be taken into consideration since, as previously described, the errors present in the quantitative results of the motion fields propagate on the latter. It would be interesting to obtain improvements or at least try to reduce the sources of error, for example by modifying the setup, as will be discussed in the next section, to obtain more robust quantitative values in such a way as to be able to make a direct comparison with the data reported in the literature.

10.3 Setup improvements

In order to improve the quality of the results obtained, both from the point of view of the visualization of the velocity fields and above all in the calculation of quantitative data, some improvements could be implemented in the setup designed for this thesis, always maintaining a relatively low cost compared to traditional PIV systems.

The first improvement could be made in the choice of the camera. In this regard, ultra high speed cameras are available on the market that allow to increase the frame rate while maintaining a low cost. Here is an example of a camera that could be used, for more information refer the reader to [83]. By increasing the frame rate it would be possible to obtain lower particle displacements between two frames and therefore considerably attenuate the uncertainties discussed in 9.1.1.

Lighting control could also be improved. Implementing a system that allows to reduce the influence of external light sources, illuminating the models only with the main light source.

In order to reduce the errors introduced by the *cylinder-chronometer* method

for flow-rate measurements, it would be ideal to use a flow-meter. In fact, this instrument allows a much more accurate calculation in flow rate measurements. With the contribution of even just some of these improvements to the measurement setup, much better results could be obtained.

10.4 Future developments

The first development of the setup proposed in this work is certainly the use of a flow-meter to have greater control over the imposed flow-rates. In particular, the experiments could be repeated for the stenotic coronary model by setting the same flow-rate values used for the healthy artery model. In this way it would be possible to more faithfully reproduce the flow conditions in the coronary arteries also in the pathological model and study the alterations of the hemodynamics produced by the restriction in a more realistic way.
The greater accuracy of the results introduced by the improvements that could be made to the setup would allow for velocity values to be more in agreement with the analytical and simulation ones. In this way it would be possible to calculate hemodynamic indices that provide quantitative information on the development and progression of the atherosclerotic pathology.
Furthermore, different geometries of the coronary vessels could be realized. This with the aim of representing different severity of the stenosis and eccentricity of the lesion in order to conduct in vitro studies on their influence in the development of the pathology. Moreover, with more accurate results, it would be possible to calculate descriptive quantities of turbulent motion with the aim of investigating the possible establishment of turbulent motions inside the coronaries despite the low Reynolds numbers (see Chapter 2).
The possible use of a greater number of cameras would allow to implement a 3D PIV in such a way as to reconstruct the velocity component outside the measurement plane. In this way, a more accurate visualization of the motion fields would be obtained, which would also lead to improvements in the quantities calculated from them. Furthermore, it would be possible in this way to calculate hemodynamic indices that allow to describe the presence of three-dimensional structures. The

latter, such as helicity, have found interest from a cardiovascular point of view due to their atheroprotective characteristics [80].
A further future application could be the study of the variation in coronary hemodynamics following the application of a stent within the models. This could be useful for determining any changes in flow that can cause accumulation of red blood cells, and other molecules, on the surface of the device that can lead to thrombus formation [84].
Finally, by introducing the particle tracer in the AIM setup, it will be possible to carry out studies on the effects of microgravity conditions on coronary artery flows. In this way it will be possible to assess whether astronauts are more exposed to the onset of cardiovascular diseases than people on Earth.

Bibliography

[1] Elena Torta. *Artery in Microgravity (AIM) Project*. Politecnico di Torino, 2018-2019. Chap. 5 (cit. on pp. 2, 71–73, 77).

[2] Jens Waschke Friedrich Paulsen. «Sobotta Atlas of Anatomy Volume». In: (2017) (cit. on pp. 4, 6, 8).

[3] «Circulation». In: (). URL: https://www.pinterest.it/pin/790381803330987868/ (cit. on p. 5).

[4] John E Hall and Michael E Hall. *Guyton and Hall textbook of medical physiology e-Book*. Elsevier Health Sciences, 2020 (cit. on pp. 5, 6, 10–14).

[5] Umberto Morbiducci. *Lessons in Fluid Mechanics*. Politecnico di Torino, 2019, pp. 13–20 (cit. on pp. 7, 8).

[6] Diego Gallo. *Biomeccanica dei Fluidi Parte II Bilanci di strato e nei continui Biomeccanica dei fluidi Parte II*. 2019 (cit. on pp. 8, 15, 107, 113, 135, 137).

[7] Richard Drake, A. Wayne Vogl, and Adam W. M. Mitchell. *Gray's Anatomy for Students E-Book*. eng. Apr. 2009. URL: https://www.123library.org/ebook/isbn/9781437720556/ (cit. on p. 9).

[8] University of Minnesota. *Human cardiac anatomy*. URL: http://www.vhlab.umn.edu/atlas/physiology-tutorial/coronary-circulation.shtml (cit. on p. 10).

[9] Tamilselvi Ramanathan and Henry Skinner. «Coronary blood flow». In: *Continuing Education in Anaesthesia Critical Care Pain* 5.2 (Apr. 2005), pp. 61–64. ISSN: 1743-1816. DOI: 10.1093/bjaceaccp/mki012. eprint: https:

//academic.oup.com/bjaed/article-pdf/5/2/61/1167967/mki012.pdf. URL: https://doi.org/10.1093/bjaceaccp/mki012 (cit. on pp. 10, 90).

[10] Elizabeth O Ofili, Arthur J Labovitz, and Morton J Kern. «Coronary flow velocity dynamics in normal and diseased arteries». In: *The American journal of cardiology* 71.14 (1993), pp. D3–D9 (cit. on pp. 11, 15).

[11] Charalambos Vlachopoulos, Michael O'Rourke, and Wilmer W Nichols. *McDonald's blood flow in arteries: theoretical, experimental and clinical principles*. CRC press, 2011 (cit. on p. 11).

[12] Novalia Sidik, Andrew Morrow, and Colin Berry. *Human Microcirculation in Ischemic Heart Disease*. Jan. 2020. DOI: 10.1161/ATVBAHA.119.313579 (cit. on p. 12).

[13] Umberto Morbiducci. *Lessons in biomechanics of the cardiovascular system*. Politecnico di Torino, 2019, pp. 13–20 (cit. on pp. 12, 14, 15, 17, 19, 120).

[14] Georg Wick and Cecilia Grundtman. *Inflammation and atherosclerosis*. Springer-Verlag Wien, Apr. 2012, pp. 1–631. ISBN: 9783709103388. DOI: 10.1007/978-3-7091-0338-8 (cit. on p. 13).

[15] Medicina Online. *Atherosclerosis*. URL: https://medicinaonline.co/2017/01/23/differenza-tra-aterosclerosi-e-arteriosclerosi/ (cit. on p. 13).

[16] HA Kirişli et al. «Standardized evaluation framework for evaluating coronary artery stenosis detection, stenosis quantification and lumen segmentation algorithms in computed tomography angiography». In: *Medical image analysis* 17.8 (2013), pp. 859–876 (cit. on p. 15).

[17] Carlos Moreno and Kiran Bhaganagar. «Modeling of stenotic coronary artery and implications of plaque morphology on blood flow». In: *Modelling and Simulation in Engineering* 2013 (2013). ISSN: 16875591. DOI: 10.1155/2013/390213 (cit. on p. 15).

[18] George A. Stouffer MD, J. Larry Klein MD, and David P. McLaughlin MD. *Cardiovascular hemodynamics for the clinician*. Ed. by Whiley Blackwill. second edition. 2017 (cit. on p. 15).

[19] K Lance Gould and Kirk Lipscomb. *Effects of Coronary Stenoses on Coronary Flow Reserve and Resistance*. 1974 (cit. on p. 16).

[20] K Lance Gould, Richard L Kirkeeide, and Martin Buchi. «Coronary flow reserve as a physiologic measure of stenosis severity». In: *Journal of the American College of Cardiology* 15.2 (1990), pp. 459–474 (cit. on p. 16).

[21] Donald F Young and Frank Y Tsai. «Flow characteristics in models of arterial stenoses—I. Steady flow». In: *Journal of biomechanics* 6.4 (1973), pp. 395–410 (cit. on p. 16).

[22] Ashkan Javadzadegan, Andy S C Yong, Michael Chang, Austin C C Ng, John Yiannikas, Martin K C Ng, Masud Behnia, and Leonard Kritharides. «First published December 15». In: *Am J Physiol Heart Circ Physiol* 304 (2013), pp. 559–566. DOI: 10.1152/ajpheart.00428.2012.-Flow. URL: http://www.ajpheart.org (cit. on pp. 17, 20, 106, 127).

[23] Sagi Raz, Shmuel Einav, Yared Alemu, and Danny Bluestein. «DPIV prediction of flow induced platelet activation-comparison to numerical predictions». In: *Annals of Biomedical Engineering* 35 (4 Apr. 2007), pp. 493–504. ISSN: 00906964. DOI: 10.1007/s10439-007-9257-2 (cit. on pp. 17, 18, 20, 133).

[24] Toshihisa Asakura and Takeshi Karino. *Flow patterns and spatial distribution of atherosclerotic lesions in human coronary arteries.* 1990. URL: http://ahajournals.org (cit. on pp. 18, 19, 120, 127).

[25] A.M. Malek and S. Izumo. «Mechanism of endothelial cell shape change and cytoskeletal remodeling in response to fluid shear stress». In: *Journal of Cell Science* 109.4 (1996), pp. 713–726. ISSN: 0021-9533. eprint: https://jcs.biologists.org/content/109/4/713.full.pdf. URL: https://jcs.biologists.org/content/109/4/713 (cit. on p. 19).

[26] Yaling Liu and Wing Kam Liu. «Rheology of red blood cell aggregation by computer simulation». In: *Journal of Computational Physics* 220.1 (2006), pp. 139–154 (cit. on pp. 19, 133).

[27] Alberto Pozo Álvarez. *SPRINGER BRIEFS IN APPLIED SCIENCES AND TECHNOLOGY COMPUTATIONAL MECHANICS Fluid Mechanics Applied to Medicine Cardiac Flow Visualization Techniques*. 2021. URL: http://www.springer.com/series/8886 (cit. on pp. 21–23).

[28] Nicholas DeMarchi and Christopher White. «Echo particle image velocimetry.» In: *Journal of visualized experiments : JoVE* (70 2012). ISSN: 1940087X. DOI: 10.3791/4265 (cit. on p. 22).

[29] Keiichi Itatani et al. «New imaging tools in cardiovascular medicine: computational fluid dynamics and 4D flow MRI». In: *General thoracic and cardiovascular surgery* 65.11 (2017), pp. 611–621 (cit. on p. 23).

[30] Osborne Reynolds. *An Experimental Investigation of the Circumstances Which Determine Whether the Motion of Water Shall Be Direct or Sinuous, and of the Law of Resistance in Parallel Channels*. 1883, pp. 935–982 (cit. on pp. 24, 25).

[31] Inge Hinterwaldner. «Parallel lines as tools for making turbulence visible». In: *Representations* 124 (1 Sept. 2013), pp. 1–42. ISSN: 07346018. DOI: 10.1525/rep.2013.124.1.1 (cit. on p. 25).

[32] Markus Raffel, Christian E Willert, Fulvio Scarano, Christian J Kähler, Steven T Wereley, and Jürgen Kompenhans. *Particle Image Velocimetry A Practical Guide Third Edition*. 2018 (cit. on pp. 26, 31–43).

[33] John F. Foss Cameron Tropea Alexander L. Yarin. *Springer Handbook of Experimental Fluid Mechanics*. 2007 (cit. on pp. 27–30).

[34] K. C. Cheng. «A HISTORY OF FLOW VISUALIZATION: CHRONOLOGY». In: *Journal of Flow Visualization and Image Processing* 4.1 (1997), pp. 9–27. ISSN: 1065-3090 (cit. on p. 27).

[35] Peter Freymuth. «Flow visualization in fluid mechanics». In: *Review of scientific instruments* 64.1 (1993), pp. 1–18 (cit. on p. 27).

[36] John Stewart Turner and John Stewart Turner. *Buoyancy effects in fluids*. Cambridge university press, 1979 (cit. on p. 28).

[37] TT Lim. «Dye and smoke visualization». In: *Flow Visualization: Techniques and Examples*. World Scientific, 2000, pp. 43–72 (cit. on p. 29).

[38] Giuseppe Carlo Alp Caridi. «Development and application of helium-filled soap bubbles For large-scale PIV experiments in aerodynamics». In: (2018). DOI: 10.4233/uuid:effc65f6-34df-4eac-8ad9-3fdb22a294dc. URL: https://doi.org/10.4233/uuid:effc65f6-34df-4eac-8ad9-3fdb22a294dc (cit. on pp. 32, 41, 42).

[39] A Melling. *Tracer particles and seeding for particle image velocimetry*. 1997, pp. 1406–1416. URL: http://iopscience.iop.org/0957-0233/8/12/005 (cit. on p. 33).

[40] Cameron Tropea. «Optical particle characterization in flows». In: *Annual Review of Fluid Mechanics* 43 (Jan. 2011), pp. 399–426. ISSN: 00664189. DOI: 10.1146/annurev-fluid-122109-160721 (cit. on pp. 34, 35).

[41] Ronald J Adrian. *PAR TICLE-IMAGING TECHNIQUES FOR EXPERIMENTAL FLUID MECHANICS*. 1991, pp. 261–304. URL: www.annualreviews.org (cit. on pp. 40, 43).

[42] Umberto Morbiducci. *Lessons in Design of prostheses and artificial organs*. Politecnico di Torino, 2019, pp. 57–90 (cit. on pp. 40, 41).

[43] Richard D Keane and Ronald J Adrian. *Theory of cross-correlation analysis of PIV images*. 1992, pp. 191–215 (cit. on p. 42).

[44] J Westerweel. *Fundamentals of digital particle image velocimetry*. 1997, pp. 1379–1392. URL: http://iopscience.iop.org/0957-0233/8/12/002 (cit. on p. 43).

[45] M. Iskander. *TRANSPARENT SOILS WIKI*. URL: https://wp.nyu.edu/ts/image-analysis/ (cit. on p. 43).

[46] Berthold KP Horn and Brian G Schunck. «Determining optical flow». In: *Artificial intelligence* 17.1-3 (1981), pp. 185–203 (cit. on pp. 44, 46, 47).

[47] *A bit of Optical Flow background*. URL: https://themagicalworldofsakie.wordpress.com/2018/07/22/a-bit-of-optical-flow-background/ (cit. on p. 44).

[48] Joel Gibson and Oge Marques. *Optical flow and trajectory estimation methods*. Springer, 2016 (cit. on p. 45).

[49] Marco Paciscopi Alessio Antonielli Giannantonio D'Avico. *Flusso Ottico: Concetti generali e metodi di calcolo* (cit. on p. 46).

[50] Bruce D Lucas, Takeo Kanade, et al. «An iterative image registration technique with an application to stereo vision». In: (1981) (cit. on p. 46).

[51] Dengsheng Zhang and Guojun Lu. «An edge and color oriented optical flow estimation using block matching». In: *WCC 2000-ICSP 2000. 2000 5th International Conference on Signal Processing Proceedings. 16th World Computer Congress 2000*. Vol. 2. IEEE. 2000, pp. 1026–1032 (cit. on p. 46).

[52] Gunnar Farnebäck. «Two-frame motion estimation based on polynomial expansion». In: *Scandinavian conference on Image analysis*. Springer. 2003, pp. 363–370 (cit. on p. 46).

[53] Tianshu Liu and Lixin Shen. «Fluid flow and optical flow». In: *Journal of Fluid Mechanics* 614 (2008), pp. 253–291. ISSN: 00221120. DOI: 10.1017/S0022112008003273 (cit. on pp. 47, 48).

[54] Tianshu Liu. «OpenOpticalFlow: An Open Source Program for Extraction of Velocity Fields from Flow Visualization Images». In: *Journal of Open Research Software* 5 (Oct. 2017). ISSN: 2049-9647. DOI: 10.5334/jors.168 (cit. on pp. 48, 49, 51, 54, 57–62, 64).

[55] Tianshu Liu, Ali Merat, M. H.M. Makhmalbaf, Claudia Fajardo, and Parviz Merati. «Comparison between optical flow and cross-correlation methods for extraction of velocity fields from particle images». In: *Experiments in Fluids* 56 (8 Aug. 2015). ISSN: 07234864. DOI: 10.1007/s00348-015-2036-1 (cit. on pp. 48, 49).

[56] M. Stanislas, K. Okamoto, C. J. Kähler, J. Westerweel, and F. Scarano. «Main results of the third international PIV Challenge». In: *Experiments in Fluids* 45 (1 July 2008), pp. 27–71. ISSN: 07234864. DOI: 10.1007/s00348-008-0462-z (cit. on pp. 62, 63).

[57] M Stanislas, K Okamoto, and C Kähler. *Main results of the First International PIV Challenge*. 2003, pp. 63–89. URL: http://www.pivchallenge.org. (cit. on p. 62).

[58] M. Stanislas, K. Okamoto, C. J. Kähler, and J. Westerweel. «Main results of the Second International PIV Challenge». In: vol. 39. Aug. 2005, pp. 170–191. DOI: 10.1007/s00348-005-0951-2 (cit. on p. 62).

[59] William Thielicke and Eize J. Stamhuis. «PIVlab – Towards User-friendly, Affordable and Accurate Digital Particle Image Velocimetry in MATLAB». In: *Journal of Open Research Software* 2 (Oct. 2014). ISSN: 2049-9647. DOI: 10.5334/jors.bl (cit. on pp. 64, 66).

[60] Stephen M. Pizer, E. Philip Amburn, John D. Austin, Robert Cromartie, Ari Geselowitz, Trey Greer, Bart ter Haar Romeny, John B. Zimmerman, and Karel Zuiderveld. «Adaptive histogram equalization and its variations». In: *Computer Vision, Graphics, and Image Processing* 39.3 (1987), pp. 355–368. ISSN: 0734-189X. DOI: https://doi.org/10.1016/S0734-189X(87)80186-X. URL: https://www.sciencedirect.com/science/article/pii/S0734189X8780186X (cit. on p. 66).

[61] R D Keane and R J Adrian. «Optimization of particle image velocimeters. I. Double pulsed systems». In: *Measurement Science and Technology* 1.11 (Nov. 1990), pp. 1202–1215. DOI: 10.1088/0957-0233/1/11/013. URL: https://doi.org/10.1088/0957-0233/1/11/013 (cit. on p. 67).

[62] Ind Eng, J.B Segur, and Helen E Oberstar. *Thermodynamic Properties of the Lighter Paraffin Hydrocarbons and Nitrogen*. 1951, p. 53. URL: https://pubs.acs.org/sharingguidelines (cit. on p. 72).

[63] Umberto Morbiducci and Diego Gallo. *Fluidi Biologici*. Politecnico di Torino, 2019 (cit. on p. 72).

[64] *TCS Micropumps website*. TCS Micropumps Ltd - Faversham Road, Faversham, Kent. ME13 0SF ENGLAND. URL: https://micropumps.co.uk/index.html (cit. on p. 73).

[65] *Elastrat Sarl*. Avenue de Châtelaine, Genève. URL: https://www.elastrat.com/?id=5 (cit. on pp. 74, 75).

[66] P Gailloud, J R Pray, M Muster, M Piotin, J H D Fasel, and D A Rüfenacht. *An in vitro anatomic model of the human cerebral arteries with saccular arterial aneurysms*. 1997, pp. 119–121 (cit. on p. 74).

[67] Diego Gallo. *Introduzione alle equazioni di bilancio, Bilanci di energia*. Politecnico di Torino, 2019 (cit. on pp. 76, 93, 105).

[68] *BDC Laboratories*. URL: http://www.bdclabs.com/ (cit. on p. 77).

[69] *LaVision Inc.* Minton Place Victoria Road Biceste. URL: https://www.lavision.de/en/ (cit. on pp. 82–84).

[70] *Samsung*. URL: https://www.samsung.com/it/smartphones/galaxy-s9/ (cit. on p. 85).

[71] *Apple*. Cupertino, California, United States. URL: https://www.apple.com/it/ (cit. on p. 85).

[72] Zhenyu Xue, John J Charonko, and Pavlos P Vlachos. «Particle image velocimetry correlation signal-to-noise ratio metrics and measurement uncertainty quantification». In: *Measurement Science and Technology* 25.11 (2014), p. 115301 (cit. on p. 96).

[73] Steve T Wereley and Juan G Santiago. *Carl D. Meinhart A PIV Algorithm for Estimating Time-Averaged Velocity Fields*. 2000. URL: http://asmedigitalcollection.asme.org/fluidsengineering/article-pdf/122/2/285/5646558/285_1.pdf (cit. on p. 96).

[74] Umberto Morbiducci and Diego Gallo. *Biomechanics of fluids*. Politecnico di Torino, 2019-2020 (cit. on p. 104).

[75] Robert McNeel et al. «Rhinoceros 3D, Version 6.0». In: *Robert McNeel & Associates, Seattle, WA* (2010) (cit. on p. 116).

[76] ANSYS. «ANSYS Fluent - CFD Software | ANSYS». In: (2016). URL: http://www.ansys.com/products/fluids/ansys-fluent (cit. on p. 117).

[77] G. Belingardi. *Il metodo degli elementi finiti nella progettazione meccanica*. Collana di progettazione e costruzione delle macchine. Levrotto & Bella, 1998. ISBN: 9788882180898. URL: https://books.google.it/books?id=VE%5C_XPQAACAAJ (cit. on p. 118).

[78] Gianluca Arcaro. «Caratterizzazione Fluidodinamica di dispositivi idraulici cavitanti= Fluid dynamic characterization of cavitating hydraulic devices». PhD thesis. Politecnico di Torino, 2020 (cit. on pp. 118, 122).

[79] Thomas Frauenfelder, Evangelos Boutsianis, Thomas Schertler, Lars Husmann, Sebastian Leschka, Dimos Poulikakos, Borut Marincek, and Hatem Alkadhi. «In-vivo flow simulation in coronary arteries based on computed tomography datasets: Feasibility and initial results». In: *European Radiology* 17 (5 May 2007), pp. 1291–1300. ISSN: 09387994. DOI: 10.1007/s00330-006-0465-1 (cit. on p. 120).

[80] Giuseppe De Nisco, Annette M. Kok, Claudio Chiastra, Diego Gallo, Ayla Hoogendoorn, Francesco Migliavacca, Jolanda J. Wentzel, and Umberto Morbiducci. «The Atheroprotective Nature of Helical Flow in Coronary Arteries». In: *Annals of Biomedical Engineering* 47 (2 Feb. 2019), pp. 425–438. ISSN: 15739686. DOI: 10.1007/s10439-018-02169-x (cit. on pp. 125, 146).

[81] Bradley A. Herbig and Scott L. Diamond. «Thrombi Produced in Stagnation Point Flows Have a Core–Shell Structure». In: *Cellular and Molecular Bioengineering* 10 (6 Dec. 2017), pp. 515–521. ISSN: 18655033. DOI: 10.1007/s12195-017-0503-x (cit. on p. 127).

[82] N J Lawson and J Wu. *Three-dimensional particle image velocimetry: a low-cost 35 mm angular stereoscopic system for liquid ows*. 1999, pp. 1–19 (cit. on p. 143).

[83] *Krontech Web site*. URL: https://www.krontech.ca/store/Chronos-1-4-High-Speed-Camera-p92268927 (cit. on p. 144).

[84] Thomas E. Watts, Arka Chatterjee, and Massoud A. Leesar. «Chapter 15 - Stent Thrombosis: Early, Late, and Very Late». In: *Cardiovascular Thrombus*. Ed. by On Topaz. Academic Press, 2018, pp. 217–224. ISBN: 978-0-12-812615-8.

DOI: https://doi.org/10.1016/B978-0-12-812615-8.00015-6. URL: https://www.sciencedirect.com/science/article/pii/B9780128126158000156 (cit. on p. 146).